Single Crystal Silicon Lorentz Force Actuated Micromirror and MEMS Blazed Grating for Optics and Sensors

by

Meiting Li

A Thesis submitted to the Faculty of Graduate Studies of

University of Manitoba

in partial fulfillment of the requirements for the degree of

MASTER OF SCIENCE

Department of Electrical and Computer Engineering

University of Manitoba

Winnipeg, Manitoba, Canada

© Copyright 2016 by Meiting Li

Abstract

Micromirrors and diffraction gratings were developed for spectroscopy and magnetic field sensor in this thesis. MEMS blazed gratings were successfully fabricated in different grating periodicities to cover a wide infrared wavelength range. Lorentz force actuated micromirrors were investigated, and two types of mirrors were fabricated: rotating and pop-up micromirrors. The deflection angle of the mirrors was controllable by altering the driving current on the mirror. Deflection angle vs. driving current was studied for different mirror types and different spring dimensions.

A Lorentz force based magnetic field sensor is also demonstrated. The sensor employs the rotating micromirror as a resonator. With an AC current flowing around the micromirror, a periodic Lorentz force is generated which drives the resonator. The rotational amplitude of the micromirror is measured with an optical positioning system and external circuits. The highest resolution of the magnetic field sensor is 0.4 nT at 50 mA_{rms}, and 53 mHz filter bandwidth. With appropriate current level, this sensor can measure a wide range of magnetic field, from nT to T.

Contributions

- A reliable process was developed to achieve 2 μm resolution in the lithography and wet etching.
- COMSOL simulation was made that coupled Lorentz force with mechanics study.
- A process to fabricate blazed gratings by anisotropic etching and oxidation sharpening was developed.
- A process to fabricate thin membranes by timed etching instead of using expensive silicon-on-oxide (SOI) wafers was implemented.

Acknowledgements

First, I would like to express my appreciation to my advisor Dr. Cyrus Shafai, for all the guidance and encouragement over the past few years. His knowledge and patience have benefitted me greatly.

I would like to thank our lab engineer Mr. Dwayne Chrusch, and all of my colleagues, Yu Zhou, and Tao Chen, for their training and help. I would also like to thank Elnaz Afsharipour for her help in the optical testing, and thank Byoungyoul Park for his help in magnetic sensor and noise analysis.

A special thanks Dr. David Prystupa and Spectrum Scientific Inc., and NSERC for their support and motivations to this project.

Finally, I also like to thank my friends, my family, and my fiancé Fan Jiang for their support in my life. I could not achieve this without your encouragement.

Table of Content:

Abstract ii
Contributions iii
Acknowledgements iv
Table of Content v
List of Figures viii
List of Tables xii

Chapter 1: Introduction 1
1.1 Motivation 1
1.2 Organization of Thesis 4

Chapter 2: Background - Micromirrors for Sensors and Spectroscopy 5
2.1 Introduction to MEMS micromirrors 5
2.1.1 Electrostatic force actuated micromirrors 5
2.1.2 Lorentz force actuated micromirror 8
2.2 Introduction to micromirrors and gratings in IR spectroscopy 10
2.2.1 MEMS dispersive spectrometer 11
2.2.2 Curved reflective grating for MEMS spectrometer 12

Chapter 3: Grating design and fabrication 14
3.1 Grating design 14
3.1.1 Grating theory 15

3.1.2 Blazed grating 18
3.2 MEMS grating fabrication design 20
3.3 MEMS grating fabrication trials 23
3.3.1 Lithography 23
3.3.2 Oxide Preparation and Silicon Etch 26
3.3.3 Oxidation sharpening 29
3.4 Experimental Testing 31
3.5 Summary 36

Chapter 4: Micromirror design and fabrication 37
4.1 Lorentz force actuated micromirror design 37
4.1.1 Design requirements 38
4.1.2 Rotating micromirror spring design and COMSOL simulation 41
4.1.2.1 Torsion bar 41
4.1.2.2 S-shape torsion spring 45
4.1.3 Pop-up micromirror spring design and COMSOL simulation 49
4.1.3.1 Cantilever 49
4.1.3.2 S-shape spring 53
4.2 MEMS micromirror fabrication design 56
4.3 MEMS micromirror fabrication trials 59
4.3.1 Backside nitride etch 59
4.3.2 Backside silicon etch 60
4.3.3 Nitride etch and Al deposition 62
4.3.4 Lithography and Al etch 63
4.3.5 Micromirror release 64
4.4 Conclusions 65

Chapter 5: Chip Testing of Micromirrors **67**
5.1 Testing environment and circuit setup 67
5.2 Testing of rotating micromirrors 69
5.2.1 Microscope measurement for rotating micromirrors 69
5.2.2 Dynamic motion measurements for rotating micromirrors 75
5.3 Testing of pop-up micromirrors 78
5.3.1 Microscope measurement 78
5.3.2 Limitations of dynamic motion measurement 82
5.4 Summary 84

Chapter 6: Magnetic field sensor **85**
6.1 Introduction to Lorentz force based magnetic field sensors 85
6.1.1 Capacitive sensing of sensor membrane position 87
6.1.2 Piezoresistive sensing of sensor membrane position 88
6.1.3 Optical sensing of sensor membrane position 89
6.2 Working principle 91
6.3 Measurement set-up 95
6.4 Resolution measurement 96
6.5 Q-factor measurement 100
6.6 Conclusion 101

Chapter 7: Conclusions and Future work **103**
7.1 Conclusions 103
7.2 Future work 104

Reference **105**

List of Figures:

Figure 1.1: Top view of Lorentz force actuated rotating micromirror. 2

Figure 1.2: Top view of Lorentz force actuated pop-up micromirrors. 2

Figure 1.3: Schematic of micromirror and Lorentz force coupling. 3

Figure 1.4: Picture of MEMS blazed grating. 3

Figure 2.1: Schematic of digital micromirror device. 7

Figure 2.2: Schematic of comb drive actuated micromirror. 7

Figure 2.3: Schematic view of the 2D micro scanning mirror (MSM). 8

Figure 2.4: Double-sided scanning micromirror array. 9

Figure 2.5: Schematic diagram of two-axis electromagnetically actuated micromirror. 10

Figure 2.6: The electromagnetic spectrum. 10

Figure 2.7: Dispersive spectrometer system set-up. 11

Figure 2.8: Top view of Lorentz force actuated rotating micromirrors. 11

Figure 2.9: Top view of Lorentz force actuated pop-up micromirrors. 12

Figure 2.10: Picture of MEMS blazed grating. 12

Figure 2.11: Schematic diagram of mini-spectrometer. 13

Figure 3.1: Picture of fabricated blazed grating. 14

Figure 3.2: Classic grating and m-order diffraction light path. 15

Figure 3.3: Diffraction pattern as a function of different slit numbers, with a = 1 μm, ... 16
d = 10 μm, wavelength at 0.5 μm.

Figure 3.4: Zero and first order diffraction pattern with (a) 20 slits, and (b) 100 slits 17
a = 2 μm, *d* = 10 μm, wavelength from 5 μm to 6 μm.

Figure 3.5: Cross-section of a commercial blazed grating and Littrow configuration. 18

Figure 3.6: Cross-section of the V-groove grating. 19

Figure 3.7: Cross-section of the sharpened blazed grating. 20
Figure 3.8: MEMS grating fabrication steps. 22
Figure 3.9: Grating mask. 22
Figure 3.10: Mask and patterned resist for grating fabrication. 23
Figure 3.11: Grating sample after KOH etching. 26
Figure 3.12: Sample after Cr etch and BOE. Photoresist was flying around. 28
Figure 3.13: Wafer positions in the oxidation furnace. 30
Figure 3.14: Grating sample after oxidation sharpening. 30
Figure 3.15: Schematic setup of an ellipsometer. 31
Figure 3.16: Measured reflectivity of blazed grating, d = 3.06 μm, at 45°, 46° and 47°. 32
Figure 3.17: Constructive mode wavelength vs. angle, d = 3.06 μm. 32
Figure 3.18: Measured reflectivity of blazed grating, d = 7.35 μm, at 45°, 46° and 47°. 33
Figure 3.19: Constructive mode wavelength vs. angle, d = 7.35 μm. 33
Figure 3.20: Measured reflectivity of blazed grating, d = 9.80 μm, at 45°, 46° and 47°. 34
Figure 3.21: Constructive mode wavelength vs. angle, d = 9.80 μm. 34
Figure 4.1: Schematic of micromirror and Lorentz force coupling. 38
Figure 4.2: Parameters in torsion bar spring, rotating micromirror. 41
Figure 4.3: First Eigen frequency for torsion bar supported rotating micromirror. 43
Figure 4.4: Temperature for torsion bar supported rotating micromirror. 44
Figure 4.5: Deflection angle vs. current for torsion bar supported rotating mirror. 45
Figure 4.6: Parameters in S-shape spring, rotating micromirrors. 46
Figure 4.7: Temperature for S-shape spring supported rotating micromirror. 47
Figure 4.8: Deflection angle vs. current for S-shape spring supported rotating micromirror. 48
Figure 4.9: Parameters of cantilever, pop-up micromirror. 49
Figure 4.10: First Eigen frequency of cantilever supported pop-up micromirror. 51
Figure 4.11: Temperature of cantilever supported pop-up micromirror. 52

Figure 4.12: Deflection angle vs. current for cantilever supported pop-up micromirror. 53
Figure 4.13: Parameters of the S-shape spring, pop-up micromirror. 54
Figure 4.14: Temperature for S-shape spring supported pop-up micromirror. 55
Figure 4.15: Deflection angle vs. current for S-shape spring supported pop-up micromirror. 56
Figure 4.16: MEMS micromirror mask. Mask #1 is the back etch mask. Mask #2 is the wire and mirror reflector mask. Mask #3 is the front etch mask to define the mirror and spring shapes. 57
Figure 4.17: MEMS mirror fabrication steps. 57
Figure 4.18: Sample after first KOH etch. 61
Figure 4.19: Samples with Al deposited on the frontside. 62
Figure 4.20: Released pop-up micromirrors. 64
Figure 5.1: Actuation circuit of micromirror. 68
Figure 5.2: Micromirror mounting. 68
Figure 5.3: Deflection angle measurement for rotating micromirror. 70
Figure 5.4: Deflection angle vs. driving current for mirror #1. 71
Figure 5.5: Deflection angle vs. driving current for mirror #2. 73
Figure 5.6: Curvature measurements for mirror #1 (units are in micrometers). 74
Figure 5.7: Curvature measurements for mirror #2 (units are in micrometers). 74
Figure 5.8: Rotating micromirror measurement before (left) and after (right) actuation. 75
Figure 5.9: Deflection angle vs. frequency for mirror #1. 77
Figure 5.10: Deflection angle vs. driving current (at resonance) for mirror #1. 78
Figure 5.11: Deflection angle for pop-up micromirror. 79
Figure 5.12: (a) Angle of lift vs. driving current for mirror #3 (upper). (b) Angle of lift vs. Lorentz force (lower). 80
Figure 5.13: (a) Angle of lift vs. driving current for mirror #4 (upper). (b) Angle of lift 81

vs. Lorentz force (lower).

Figure 5.14: Curvature measurements for mirror #4 (units in micrometers). 82

Figure 5.15: Pop-up micromirror measurements before (a) and after (b) actuation. 83

Figure 6.1: Lorentz force resonator in a magnetic field. 86

Figure 6.2: Schematic diagram of magnetic field sensor with capacitive sensing. 88

Figure 6.3: Schematic diagram of magnetic field sensor with piezoresistive sensing. 89

Figure 6.4: Resonance based magnetic field sensor with optical measurement. 90

Figure 6.5: Resonance based magnetic field sensor set-up. 91

Figure 6.6: Schematic of micromirror and Lorentz force coupling. 92

Figure 6.7: Deflection angle vs. driving current, mirror #1. 92

Figure 6.8: Block diagram of magnetic field sensor system. 93

Figure 6.9: Angle measurement with the optical positioning system. 93

Figure 6.10: Resonance based magnetic field sensor set-up. 95

Figure 6.11: Measured magnetic field vs. distance from the sensor to magnets. 96

Figure 6.12: Noise spectrum of uop-amp with different driving current. 97

Figure 6.13: Noise signal (rms) at different integration times. 98

Figure 6.14: Measured sensitivities at different driving current, 3 seconds integration time. 99

Figure 6.15: Q-factor of magnetic field sensor. 101

List of Tables

Table 3.1: Wavelengths (nm) of constructive modes, d = 3.06 µm. 35

Table 3.2: Wavelengths (nm) of constructive modes, d = 7.35 µm. 35

Table 3.3: Wavelengths (nm) of constructive modes, d = 9.80 µm. 36

Table 4.1: Relationships between design considerations and parameters. 40

Table 4.2: Parameters of torsion bar supported rotating micromirror. 42

Table 4.3: Parameters of S-shape spring supported rotating micromirror. 46

Table 4.4: Parameters of cantilever supported pop-up micromirror. 50

Table 4.5: Parameters of S-shape spring supported pop-up micromirror. 54

Table 5.1: Summary of micromirrors. 84

Table 6.1: Summary of various resonance magnetic field sensors. 102

Chapter 1: Introduction

1.1 Motivation

In this thesis, micromirror and diffraction grating elements were developed for magnetic field sensor and optical spectroscopy applications. Rotation and pop-up Lorentz force micromirrors were designed and tested. The goal was the development of micromirrors with large deflection angle, resonance frequency in the 100's of Hz, and which required low power consumption (100 mW for each micromirror). Blazed diffraction gratings for infrared (IR) spectroscopy were fabricated on silicon wafers and designed for potential integration onto the micromirrors.

Rotational and pop-up micromirrors:

Two types of micromirrors were fabricated and tested. Three torsional rotating micromirrors are shown in Figure 1.1, and two pop-up mirrors are shown in Figure 1.2. Both rotating and pop-up micromirrors were fabricated on single crystal silicon wafers and measured 3 × 3 mm. Mirrors are seen held up by silicon micro-springs, and the thickness of the spring and mirror elements was ~ 10 μm.

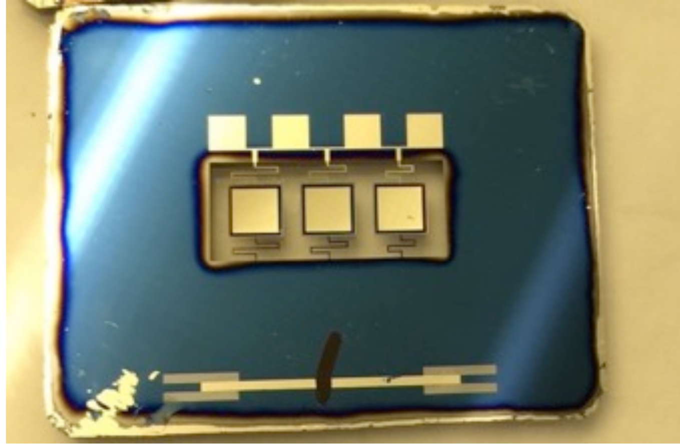

Figure 1.1: Top view of Lorentz force actuated rotating micromirrors.

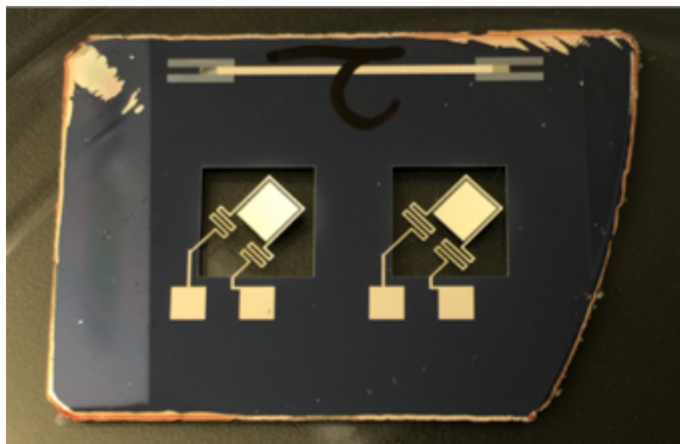

Figure 1.2: Top view of Lorentz force actuated pop-up micromirrors.

The micromirrors are actuated by Lorentz force coupling between an electric current flowing in a wire coil along the outer edge of the mirror, and a nearby permanent magnet (see Figure 1.3). The Lorentz force on the edges of the micromirror gives a rotational torque, which actuates the micromirrors in the desired direction.

Fabricated micromirrors were tested for their mechanical performance. They were also applied as a magnetic field sensor, making use of the Lorentz force rotation as a measure of the intensity of the magnetic field. The resolution of the sensor in this application was found to be 0.4 nT, which is the highest internationally achieved for any MEMS Lorentz force sensor [1].

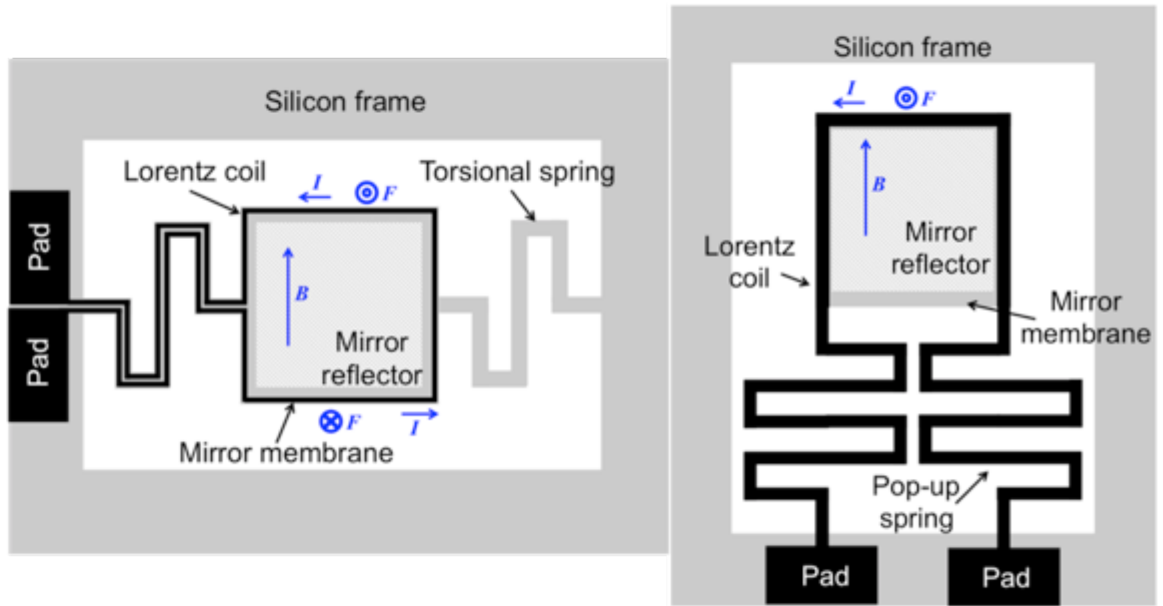

Figure 1.3: Schematic of micromirror and Lorentz force coupling.

Diffraction grating:

Figure 1.4 shows one MEMS blazed grating for infrared (IR) spectroscopy that was fabricated. The blazed gratings ranged from 3.06 μm to 9.8 μm. They were etched on a silicon wafer, and then sharpened for better optical efficiency.

Figure 1.4: Picture of MEMS blazed grating.

1.2 Organization of Thesis

- Chapter 2: MEMS micromirrors for sensors and spectroscopy. It also includes a literature review of MEMS micromirrors for spectroscopy and magnetic field sensors.
- Chapter 3: The diffraction grating developed for the spectrometer. It includes a brief introduction to grating theory, the detailed fabrication process, and the testing of the fabricated blazed gratings.
- Chapter 4: The Lorentz force actuated rotating and pop-up micromirrors. The design requirements, COMSOL simulation, and fabrication process are discussed.
- Chapter 5: The testing methodology and measured results for Lorentz force actuated micromirrors. This chapter also includes the comparison between testing results and COMSOL simulation results.
- Chapter 6: This chapter presents the magnetic field sensor based on the Lorentz force actuated micromirror. The working principle, circuit design, and the testing results are presented.
- Chapter 7: Conclusions and suggestions for future work related to this thesis.

Chapter 2: Background - Micromirrors for Sensors and Spectroscopy

This chapter will present a general introduction to the design and fabrication of rotating MEMS micromirrors and blazed gratings. These structures were developed for a future micro-spectroscopy system. This chapter will include a brief literature review, and discussion of MEMS fabrication and actuation techniques related to these topics.

2.1 Introduction to MEMS micromirrors

A MEMS micromirror consists of a microfabricated platform, supported by flexible springs. In the case of a micromirror, this platform is coated with a reflective coating. Much research has been focused on micromirrors over the past years. For micromirrors with large deflection angle, the most common actuation methods fall into two groups: electrostatic force actuation, and Lorentz force actuation. Thermal actuation has also been used, but to a lesser degree, and so it will not be discussed here.

2.1.1 Electrostatic force actuated micromirrors

For electrostatic force actuators, voltage is applied on parallel plate capacitive electrodes or comb drive capacitors to provide the actuation force. The capacitance for a parallel plate capacitor, if neglecting fringing effects, is given by the following equation:

$$C = \frac{\varepsilon A}{d} \tag{2.1}$$

where A is the overlapping area, d is the distance between two conducting plates, and ε is the dielectric permittivity of the insulator between plates.

The energy stored in the capacitor, when a voltage V is applied, is given by:

$$W = \frac{1}{2}CV^2 = \frac{1}{2}\frac{\varepsilon A V^2}{d} \tag{2.2}$$

The electrostatic force between two charged plates is then found from Equation 2.2. It is proportional to the overlapping area A and the voltage V^2, as shown below:

$$F = \frac{dW}{dz} = -\frac{1}{2}\frac{\varepsilon A V^2}{d^2} \tag{2.3}$$

The digital micromirror device (DMD) produced by Texas Instruments [2] is one of the most commercially successful micromirror devices. The DMD chip consists of an array of 16 µm × 16 µm micromirrors. Each micromirror has two sets of parallel plate electrodes, enabling the micromirror to rotate between +12° and -12°. Figure 2.1 illustrates the schematic of an individual micromirror.

The DMD fabrication starts with the deposition and patterning of a bottom aluminum electrode. An organic sacrificial layer is deposited and patterned for the structure of torsional hinges, and spacing it above the electrodes. After sputtering and patterning the metal hinges, another organic sacrificial layer is spin-coated, and patterned for the mirror, and to space the mirror above the hinges. A layer of aluminum is sputtered and etched into the shape of mirror. Finally, the mirror element is released by removing both sacrificial layers.

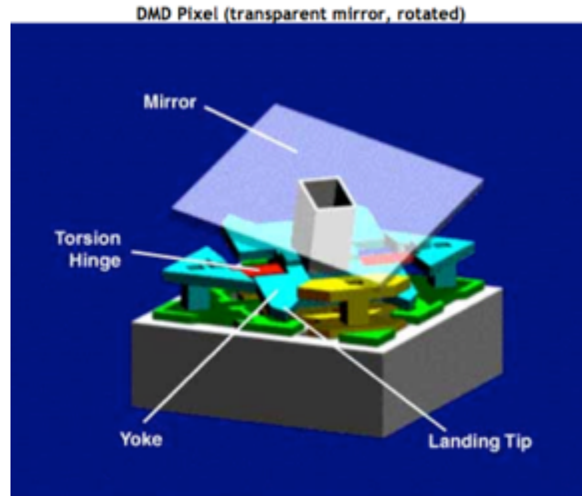

Figure 2.1: Schematic of digital micromirror device [2].

Comb drive actuated micromirrors have been demonstrated by several research groups. The comb drive has the advantage in being a 3D structure (vertical in depth), enabling more force to be applied for a given surface area. In Krishnamoorthy et al. [3], a 300 µm × 100 µm × 40 µm (L×W×H) micromirror and a set of lower comb drive electrodes were built with a deep reactive ion etch (DRIE) technique on silicon-on-insulator (SOI) wafers. The micro-mirror rotated when an AC voltage was applied on the comb drives. The deflection angle was 4° for an applied applied voltage of 75 $V_{\text{peak to peak}}$. This angle would increase to 40° if the applied voltage was at the mechanical resonance of the structure.

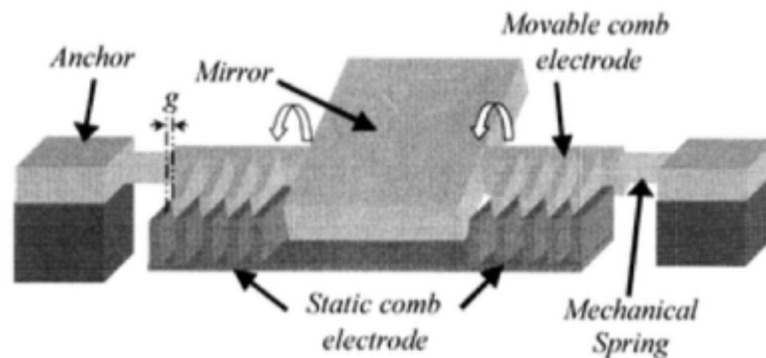

Figure 2.2: Schematic of comb drive actuated micromirror [3].

Schenk et al. [4] demonstrated a 2D comb drive actuated micromirror. The outer plate and the silicon frame employed a set of combdrives, which controls the rotation along the x-axis. The mirror plate, which was suspended inside the outer frame, had another set of comb drives, controlling the rotation angle along the y-axis. This micromirror was also fabricated on SOI wafers. The micromirrors had a thickness of 20 µm to 30 µm, and the size of the micromirror ranged from 0.5 mm × 0.5 mm to 3 mm × 3 mm.

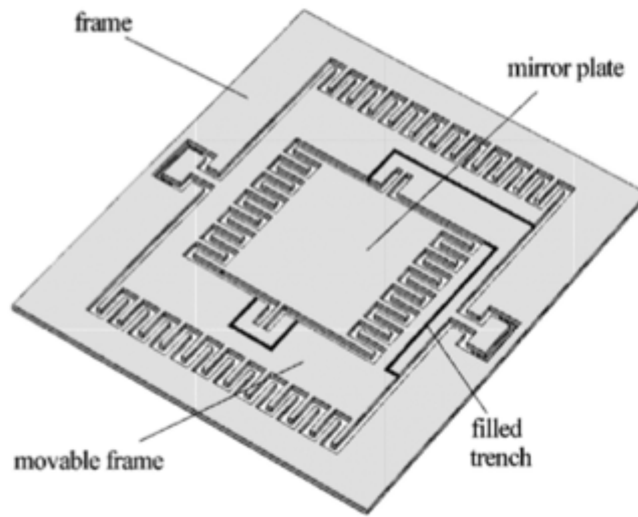

Figure 2.3: Schematic view of the 2D micro scanning mirror (MSM) [4].

2.1.2 Lorentz force actuated micromirror

Lorentz force is generated on moving charged particles in a magnetic field. The Lorentz force on a current carrying wire follows the equation given by:

$$\vec{F} = I\vec{\ell} \times \vec{B} \tag{2.4}$$

where I is the current flowing across the wire, $\vec{\ell}$ is the vector for length of the wire, and $\vec{B}$ is the magnetic flux density vector. We can see that the Lorentz force on the micromirror follows a linear function with the current and magnetic field intensity.

Nakai et al. [5] presented a Lorentz force actuated pop-up micromirror. An array of 520 μm × 450 μm × 20 μm (L×W×H) micromirrors were fabricated from SOI wafers. The fabrication starts by growing 150 nm thermal oxide as insulation layer. Then, a layer of 150 nm thick Ni was deposited by sputtering, and etched to form the shape of mirrors, wires, and hinges. The micromirrors were released by DRIE on both sides. This micromirror array was designed to work on both sides.

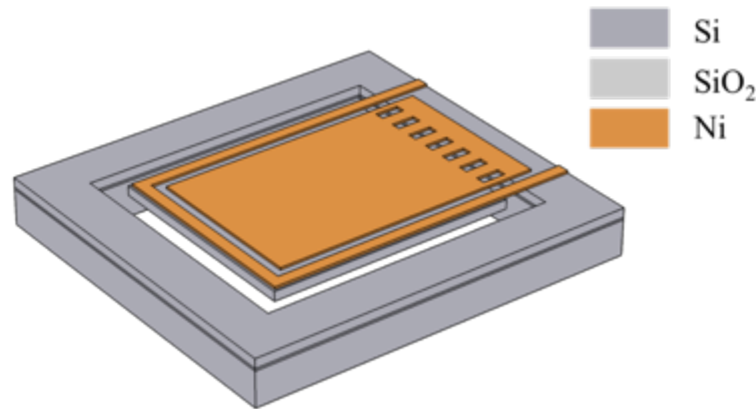

Figure 2.4: Double-sided scanning micromirror array [5].

A two-axis electromagnetically actuated micromirror was proposed and fabricated by Cho et al. [6]. This micromirror had two types of Lorentz force actuators; x-axis actuators outside the mirror plate, and y-axis actuators integrated on the mirror plate. The two-axis micromirrors were fabricated from SOI wafers with a 5 μm top silicon layer. Mirror structures were etched on the top silicon layer with RIE. Then, copper coils were electroplated. A photoresist sacrificial layer was coated to make an air gap under the copper bridge, which was grown by anther electroplating process. The micromirrors were finally released by etching silicon and the buried silicon oxide layer from the backside. The maximum defection angle of the two-axis micromirror was ±15.7° for x-axis actuation, and ±4.35° for y-axis in a 0.16 T magnetic field.

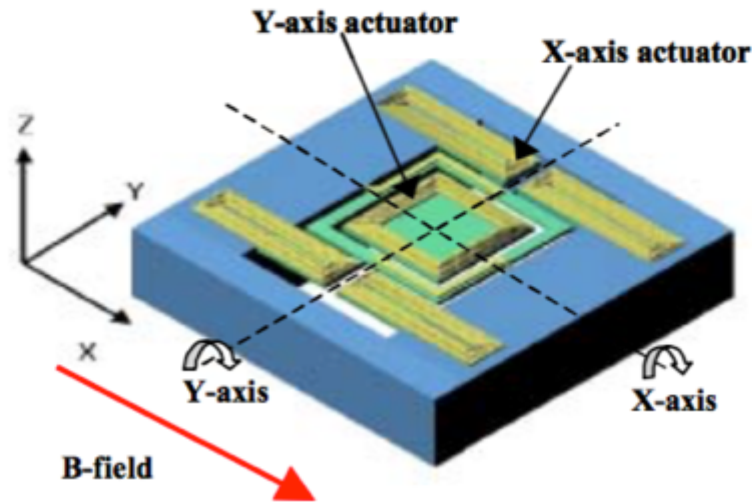

Figure 2.5: Schematic diagram of two-axis electromagnetically actuated micromirror [6].

2.2 Introduction to micromirrors and gratings in spectroscopy

Infrared (IR) spectroscopy is a spectroscopy that analyzes the absorption spectrum between 700 nm and 1 mm in wavelength. It is widely used in identifying and analysis of chemicals.

IR absorption spectrum is related to the rotational and vibrational energy transitions in a molecule [7]. When recognizing chemicals, IR radiation is mostly used in two regions: group frequency region, from 2.5 μm to 7.7 μm, and fingerprint region, from 7.7 μm to 25 μm [8]. In the spectroscopy, the periodicity of the grating depends on the working wavelength range.

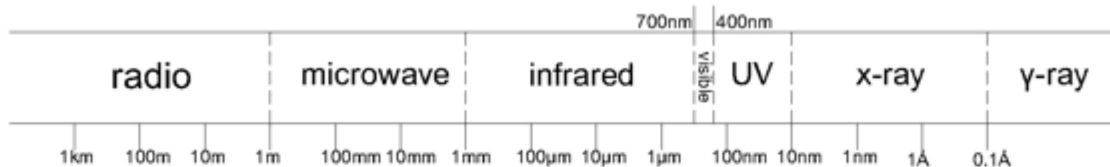

Figure 2.6: The electromagnetic spectrum.

2.2.1 MEMS dispersive spectrometer

In our dispersive spectroscopy (Figure 2.7), the absorption spectrum is measured as a function of wavelength. In this system, a grating is used as a monochromator that bends incident light to an angle as a function of its wavelength. Rotating micromirrors are adopted to guide specific wavelength to the photodetector. Pop-up micromirrors are adopted as optical switch to choose between sample and reference optical path. Note that the grating can be integrated on the surface of the rotating micromirror (as shown in Figure 2.7), or it can be separated from the rotating mirror as well. The fabricated micromirrors and gratings are illustrated in Figure 1.1, 1.2 and 1.4, (reproduced as Figure 2.8 to 2.10 below).

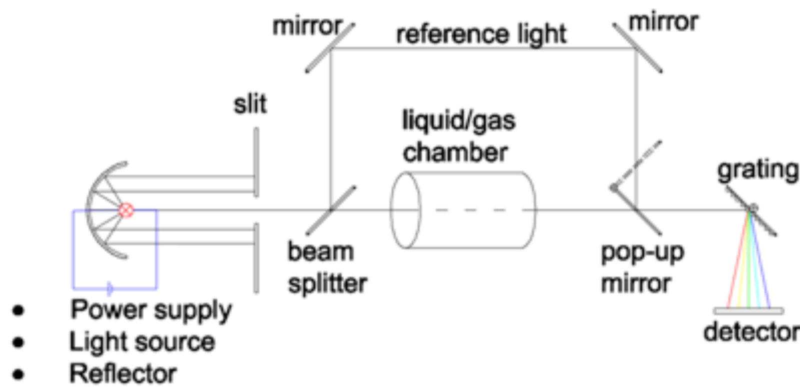

Figure 2.7: Dispersive spectrometer system set-up.

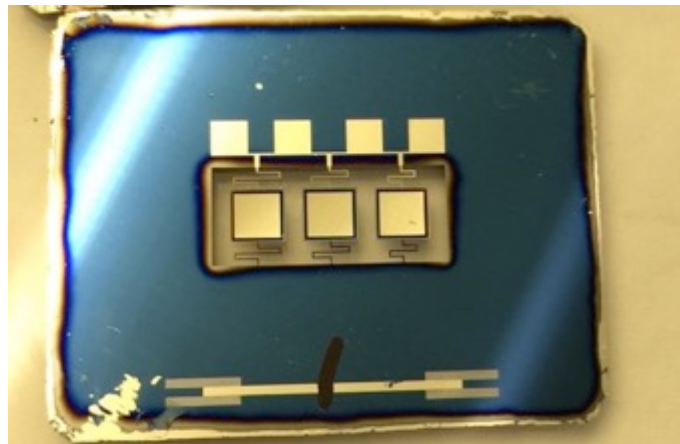

Figure 2.8: Top view of Lorentz force actuated rotating micromirrors.

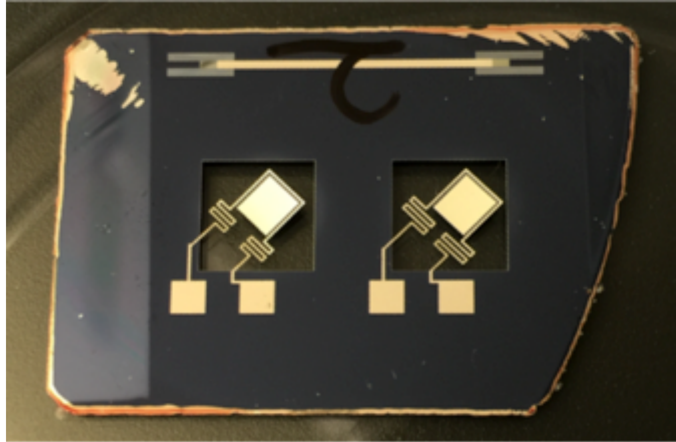

Figure 2.9: Top view of Lorentz force actuated pop-up micromirrors.

Figure 2.10: Picture of MEMS blazed grating.

2.2.2 Curved reflective grating for MEMS spectrometer

An innovative mini-spectrometer has been developed by Hamamatsu Photonics [9]. This spectrometer integrates all the components in a single chip. The top plate contains a CMOS image sensor and an optical slit. A convex lens with gratings on the surface is fabricated by nano-imprinting techniques. The grating works as a monochrometer, and the concave lens focuses the reflected light on image sensor. This design avoids using micromirrors, and thus can be made very compact.

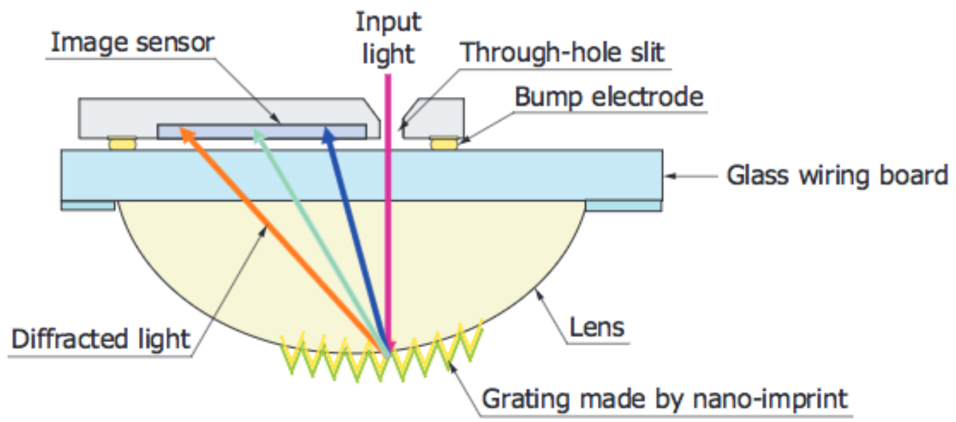

Figure 2.11: Schematic diagram of mini-spectrometer [9].

Chapter 3: Grating design and fabrication

This chapter presents the design of the diffraction gratings developed for this project. Gratings were designed to work in 2 μm to 15 μm for IR spectroscopy. This chapter will first present a brief introduction to grating theory, followed by a detailed description of the developed grating fabrication process and the testing of the gratings.

3.1 Grating design

A diffraction grating is an optical device with periodic grooved structure. In our system, a process to make reflective blazed gratings (Figure 1.4, reproduced as Figure 3.1 below) was developed to achieve a low-loss light path for IR spectroscopy.

Figure 3.1: Picture of fabricated blazed grating.

Compared with classic gratings, a blazed grating can focus light on a non-zero order, and thus achieve a higher optical efficiency. Gratings may be reflective or transmissive. Even in the near-IR and mid-IR range, single crystal silicon has a relatively high transmittance, and is usually considered as "transparent". The transmittance also depends highly on the grade, purity, and thickness of the silicon wafer [10]. This problem can be avoided by depositing a thin layer of metal, and so make a reflective grating.

3.1.1 Grating theory

For a diffraction grating (Figure 3.2) the reflected light photons interfere with each other, generating a diffraction pattern. When the light path difference between two neighbouring light beams is equal to an integer number of wavelengths λ, the light beams will be in-phase, and a higher intensity of light will be observed at that particular angle.

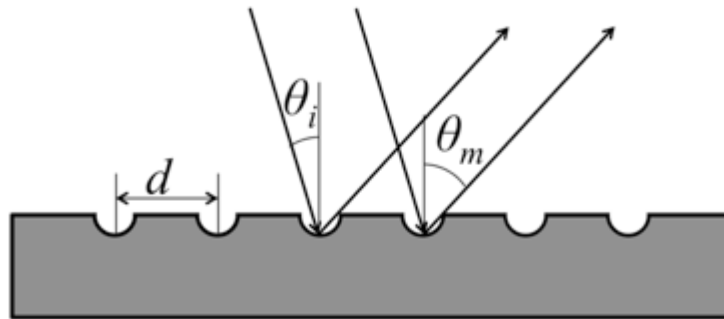

Figure 3.2: Classic grating and m-order diffraction light path.

Equation 3.1 shows the condition for constructive interference, where the light path difference equals an integer number of wavelengths. The angle of m-order diffracted light θ_m is a function of the angle of incident light θ_i, wavelength λ, and slit (or groove) spacing d of the grating. This equation applies to most gratings.

$$d\left(\sin\theta_i + \sin\theta_m\right) = m\lambda \tag{3.1}$$

The single wavelength diffraction pattern consists of a series of peaks with different light intensity. For a classic grating, the multiple slits diffraction intensity pattern can be described as a function of diffraction angle θ, given by:

$$I(\theta) = I_0 \frac{\sin^2(\beta)}{\beta^2} \frac{\sin^2(N\gamma)}{N^2 \sin^2(\gamma)} \tag{3.2}$$

where $\beta = \frac{\pi a}{\lambda}\sin\theta, \gamma = \frac{\pi d}{\lambda}\sin\theta$ (with a the slit width and d is the slit periodicity), and N is the number of grating slits.

Figure 3.3 plots the intensity over diffraction angle, which is calculated from Equation 3.2. Both a single slit pattern and five slit diffraction pattern are plotted in this figure, with the same wavelength and slit width. As shown in the five slit diffraction pattern, a single wavelength light beam is diffracted into a group of beams at different angles, whose envelope follows the single slit diffraction pattern. For a classic grating, most of the energy is focused on the zero order.

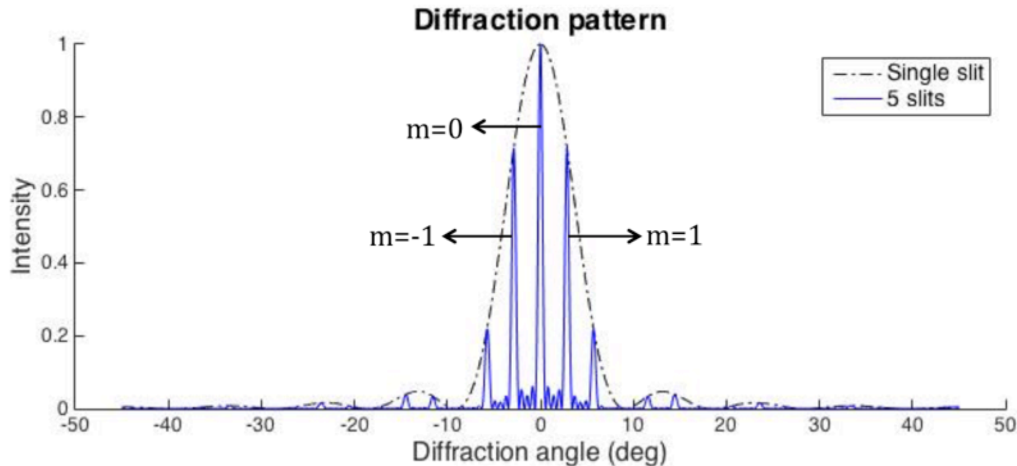

Figure 3.3: Diffraction pattern as a function of different slit numbers, with a = 1 μm, d = 10 μm, wavelength at 0.5 μm.

Figure 3.4 compares the angle of first order diffraction for different wavelength, as solved from Equation 3.2. It also shows the resolution of the diffraction grating with different number of slits. At first order diffraction, different wavelengths are separated at different angles, which provide the possibility of using a grating as a monochromator. As the number of slits increases, the width of each peak will decrease. According to the Nyquist law, the resolution of a signal is limited to the line width of each peak in the signal. Thus, a higher resolution can be achieved with a higher number of slits in the grating. It can also be concluded from Figure 3.4 that, the spectrometer can work at a larger range of wavelengths, when it is capable of sweeping across larger deflection angles.

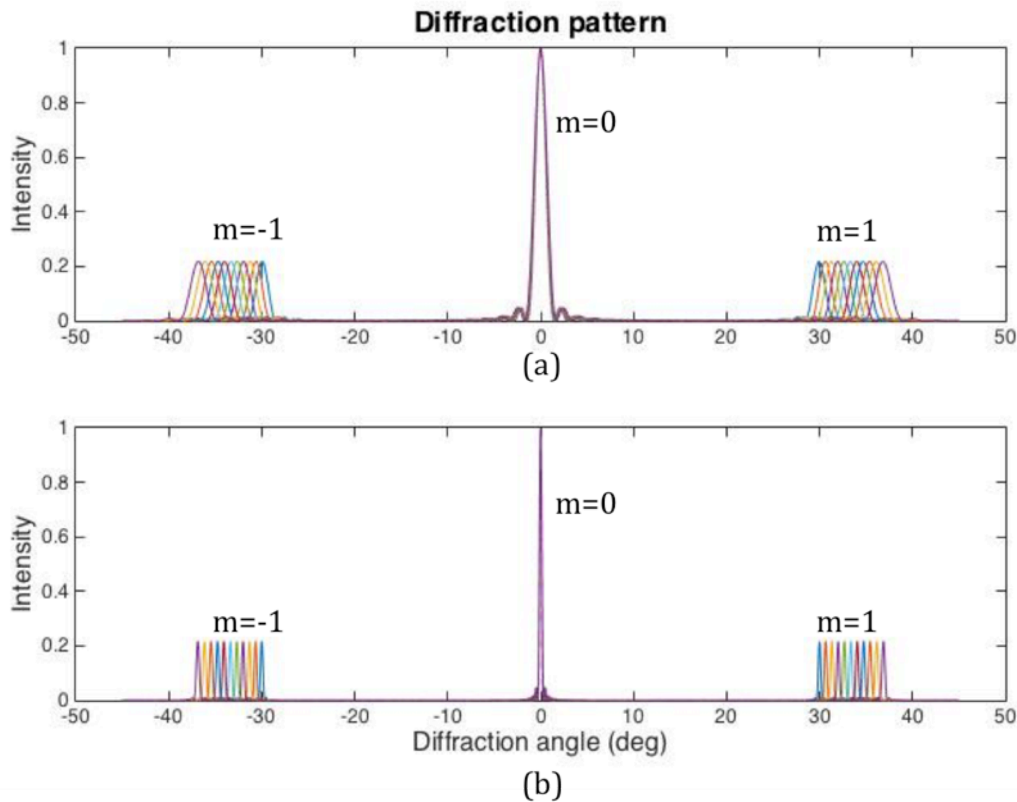

Figure 3.4: Zero and first order diffraction pattern with (a) 20 slits, and (b) 100 slits a = 2 µm, d = 10 µm, wavelength from 5 µm to 6 µm.

3.1.2 Blazed grating

The biggest drawback of a classic grating is low grating efficiency. As illustrated in Figure 3.3 and Figure 3.4, zero order, which has highest light intensity, cannot be applied as a monochromator. In order to optimize grating efficiency, a blazed grating is adopted to concentrate light intensity onto non-zero orders of diffraction light.

Figure 3.5 illustrates a commercial blazed grating. It consists of periodic triangle grooves forming a sawtooth-shaped cross-section. A commercial blazed grating is usually mechanically ruled with a ruling engine [11]. The grating equation (Equation 3.1) is valid for a blazed grating as well. It will not be affected by the blaze angle θ_B.

For blazed gratings, Littrow configuration is usually applied, in order to achieve maximum efficiency. The Littrow configuration is illustrated in Figure 3.5, which shows that the m-order diffraction is reflected towards incident light, $\theta_i = \theta_m = \theta_B$. Hence, the incident light is perpendicular to the slopes on the blazed gating surface, which helps focusing the maximum optical energy at m-order diffraction. Under such this condition, the grating equation can be written as:

$$m\lambda = 2d\sin\theta_B \tag{3.3}$$

$$d = \frac{m\lambda}{2\sin\theta_B} \tag{3.4}$$

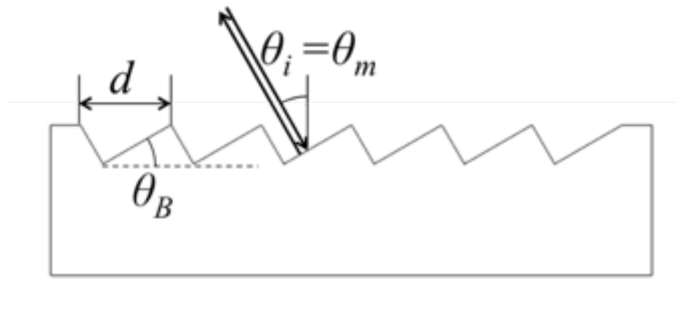

Figure 3.5: Cross-section of a commercial blazed grating and Littrow configuration.

The choice of grating periodicity and the blaze angle θ_B mainly depends on the working wavelength λ. From Equation 3.4, it can be concluded that slit spacing d should be on the same order as wavelength λ. For the blaze angle design, the substrate material and fabrication techniques should also be taken into consideration.

In MEMS applications silicon is chosen as the substrate to fabricate blazed gratings. When etching a blazed grating from a silicon wafer, anisotropic wet etching can help achieve a smooth saw-toothed sidewall. During a silicon anisotropic etching of a (100) wafer, the etch rate on (111) surface is 400 times slower, thus the etching will eventually result in V-groove profile with the sidewall at 54.7°. Figure 3.6 illustrates the cross-section of the grating after a (100) wafer silicon anisotropic etching.

Figure 3.6: Cross-section of the V-groove grating.

Many research groups have fabricated this type of grating. Hintschich et al. [12] presented a V-groove grating, which was fabricated by anisotropic TMAH etching. The grating had a periodicity of 3.019 µm, and top platform width of 0.67 µm. This grating was designed for operation between 1000 nm and 1900 nm, with a spectral resolution of 10 nm.

The biggest drawback of a V-groove grating is the optical energy loss caused by the flat platform in between grating grooves. In order to minimize this effect, an oxidation sharpening is adopted, and was also used in the design of this thesis. For the oxidation sharpening, the grating is placed in an oxidation oven to grow a silicon dioxide layer of certain thickness. The amount of silicon consumed in the oxidation process is 44% of the oxide thickness [13]. In order to make an ideal sharpened blazed grating, the oxide layer

should be thick enough so that it consumes enough of silicon equal to half the width of the flat platform between the grating grooves. Then, when the oxide layer is removed, remaining are sharp tips on the silicon gratings.

The oxidation sharpening process only perfects the tip of the grating. The bottoms of grating groove will be rounded in this process (Figure 3.7). In practice, the blazed grating is usually working under the Littrow configuration. For grating with big blaze angle, the bottoms of grating grooves will be under the shadow, and thus will not affect grating's efficiency.

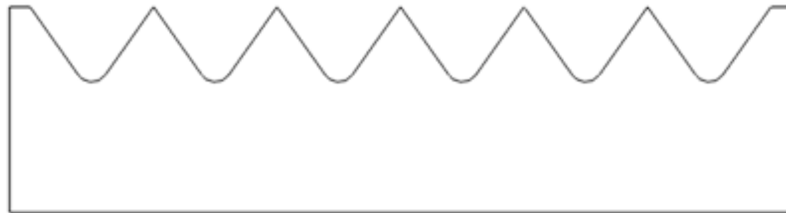

Figure 3.7: Cross-section of the sharpened blazed grating.

3.2 MEMS grating fabrication design

For this thesis, MEMS gratings are fabricated on 375 μm thick, <100> silicon wafers. In order to cover a bigger range of wavelengths, three different gratings were designed with three different spacings *d*: 3.06 μm, 7.35 μm, and 9.80 μm. The fabrication steps are illustrated in Figure 3.8.

- Wet oxidation is done to grow a 400 nm thick layer of silicon oxide on both sides of the wafer, to be used as a mask for the subsequent silicon etch. The wafers were placed in the oxidation furnace at 1100°C for 30 minutes, and N_2 flow rate at 1033 sccm (Figure 3.8a).

- 150 nm thick chrome film is sputtered on the frontside of the wafer. For Cr sputtering, Ar was set at 41 sccm, and DC power at 200 W for 120 seconds (Figure 3.8b). This metal film helps the photoresist to adhere to the silicon oxide.
- Photoresist is spun and patterned on the frontside using the grating mask (Figure 3.8c).
- Following this step is chrome wet etch, and BOE (buffered oxide etch) etching of the silicon dioxide (Figures 3.8d and 3.8e). After this, the photoresist is removed and the remaining chrome is etched, leaving only the patterned oxide layer as mask for KOH etch (Figure 3.8f). Removal of photoresist and chrome prevents contamination of the KOH solution.
- In order to achieve V-grooves for blazed grating, 30 wt.% KOH solution at 80°C is used for an anisotropic etch (Figure 3.8g). This solution etches the (100) surface 400 times faster than (111) surface. The resulting sidewall angle is 54.7°. When reaching a V-groove, the entire exposed silicon surface is (111) surface.
- An oxidation sharpening is done to sharpen the tip of blazed gratings. The grating is piranha (H_2SO_4 : H_2O_2 4:1) cleaned before oxidation sharpening. This removes trace organic contaminants from contaminating the furnace. After 5.5 hours of wet oxidation at 1100°C and 2520 sccm N_2 flow, a layer of 1 μm oxide is grown, (Figure 3.8h).
- The oxide layer is removed in BOE etching (Figure 3.8i).

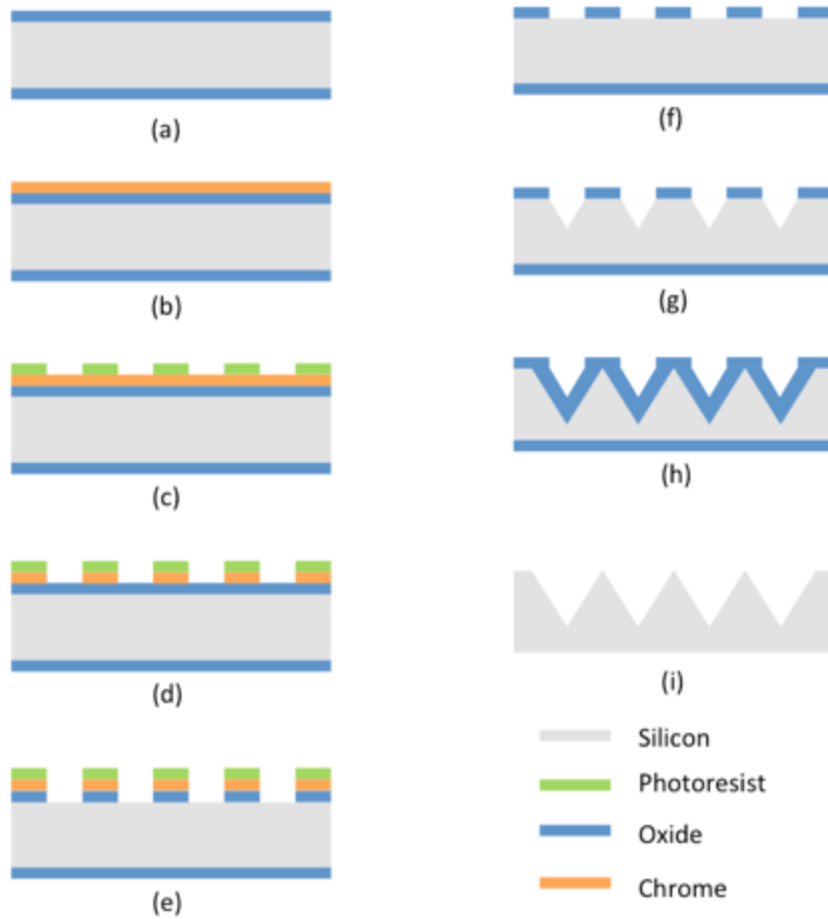

Figure 3.8: MEMS grating fabrication steps.

Figure 3.9 illustrates the mask used for grating fabrication. The gratings come in different periodicities: 3.06 µm, 7.35 µm, and 9.80 µm. For all the gratings, the chrome covered stripes between the grating grooves on the mask are the same width of 2 µm.

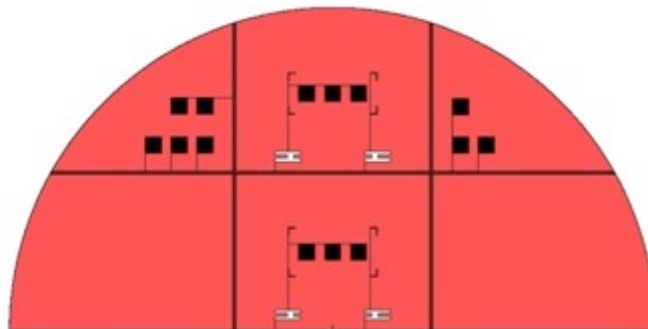

Figure 3.9: Grating mask.

3.3 MEMS grating fabrication trials

3.3.1 Lithography

Figure 3.10 shows a picture of the patterned photoresist for grating fabrication. It took several attempts before the proper recipe was found. These attempts were made to pattern the frontside oxide with the 3 μm to 10 μm features. Various techniques were used. In trial #5, the lithography was done on a thin reflective chrome layer. After this, different widths of photoresist were observed.

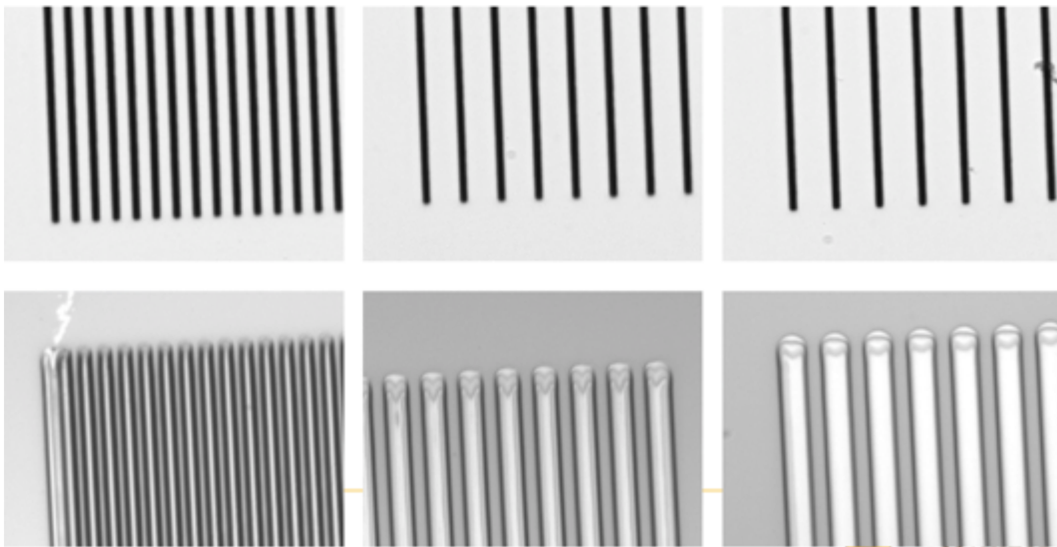

Figure 3.10: Mask and patterned resist for grating fabrication.

Trial #1

- Two wafers were coated with HPR 504 photoresist that was spun at 4000 rpm for 40 seconds. The thickness was 1.7 μm.
- The wafers were put on a hotplate at 115°C for 90 seconds (softbake) to remove solvents in resist.
- The wafers were aligned to the mask and exposed to UV for 2 seconds.

- The resist was developed in HPR 504 developer by hand for 30 and 40 seconds respectively for the two wafers.
- The wafers were rinsed with de-ionized (DI) water and blown dry.
- Results: Some of the 3 μm features were washed off, because the resist didn't adhere very well to the wafer. Other features showed signs of underdevelopment or underexposure. However, low humidity in the lab can also lead to this result. It was hypothesized that a thinner resist layer can also help achieving better resolution.

Trial #2 - using thinner resist

- Four wafers were put on the hotplate 115°C for 90 seconds (dehydration bake) to remove water on the wafer surface. This helps the resist to adhere to the wafer.
- HPR 504 photoresist was spun at 6000 rpm for 40 seconds. The thickness was 1.3 μm.
- Softbake at 115°C for 90 seconds.
- After soft bake, the wafers were rinsed with DI water and blown dry. This brings water back into the photoresist, and helps improve lithography quality.
- Exposure for 2 seconds.
- The resist were developed with the Solitec developer system for 10, 15, 17, and 20 seconds respectively. The Solitec system uses the same HPR 504 developer solution.
- Results: The 10 seconds and 15 seconds sample showed better results.

Trial #3 - plasma etching used

- Three wafers were dehydration baked at 115°C for 90 seconds.
- Photoresist was spun at 6000 rpm for 40 seconds. The thickness was 1.3 μm.
- Softbake at 115°C for 90 seconds.
- Rinse with DI water and blow dry.
- Exposure for 2 seconds.

- Developing with Solitec the developer system for 10, 11, and 12 seconds respectively.
- All of the features were underdeveloped or underexposed. However, at 11 seconds, the lines are sharp and clear for all different size features. About 100 nm resist was left undeveloped. This can be removed with oxygen plasma. Increasing the exposure time can also help improve the results.
- The 11s sample was etched in oxygen plasma (ashing) for 30 seconds. On the Trion RIE plasma etcher, the pressure was 200 mT, O_2 40 sccm, RIE 25 W, and ICP 100 W.
- After ashing, all resist was etched by 200 nm, and so all the undesired resist was gone.

Trial #4 - longer exposure and no plasma etch

- Two wafers were dehydration baked at 115°C for 90 seconds.
- Photoresist was spun at 6000 rpm for 40 seconds. The thickness was 1.3 µm.
- Softbake at 115°C for 90 seconds.
- Rinse with DI water and blow dry.
- Exposure for 2.5 and 3 seconds respectively.
- Developing with Solitec developer for 11 seconds.
- Results: The features were sharp and clear. Since the photoresist was exposed for longer time, all the features were well developed, and plasma etching was not necessary. However, as shown in Figure 3.10, all the stripes were wider than the stencils, because of underexposure. This only affects the width of each line in the grating, and won't affect the periodicity.

Trial #5 - litho on Cr layer

- A layer of 150 nm chrome film was sputtered on the oxide wafer. Ar flow 41 sccm, and power 200 W for 120 seconds.

- Dehydration bake at 115°C for 90 seconds.
- Photoresist was spun at 6000 rpm for 40 seconds. The thickness was 1.3 µm.
- Softbake at 115°C for 90 seconds.
- Rinse with DI water and blow dry.
- Exposure for 2.5 and 3 seconds respectively.
- Developing with Solitec developer for 11 seconds.
- Results: Adhesion for resist is very good, compare to oxide substrates. The resist stripes were narrower than resist on SiO_2 substrate. In addition, the reflective Cr layer effectively increases the light intensity in the exposure process, and thus resulting in narrower stripes.

3.3.2 Oxide Preparation and Silicon Etch

In order to etch the V-grooves for the blazed grating, an oxide mask is prepared for KOH etching. However, photoresist doesn't adhere well to oxide. It took us several attempts to solve this problem. Various techniques and materials were used. Figure 3.11 shows the sample after silicon etch.

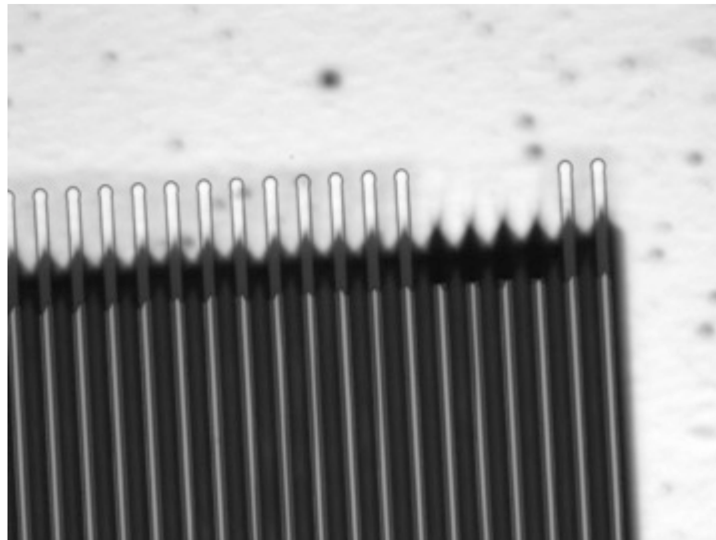

Figure 3.11: Grating sample after KOH etching.

Trial #1

- Wafer was put into 1100°C furnace for 30 minutes, with 1033 sccm N_2. The wet oxide was about 400 nm thick.
- The oxidized wafer was put into The HMDS oven for HMDS coating in a 3 minutes process. This can help the resist to adhere better to the wafer.
- Lithography was done with recipe in trial #4.
- No hardbake was done after lithography.
- Wafer was etched in 10:1 BOE for 20 minutes.
- Results: Resist failed because BOE is too aggressive. Hardbake after lithography could help resist to last longer.

Trial #2 - hardbake after litho

- Wet oxidation at 1100°C for 30 minutes.
- HMDS coating for 3 minutes.
- Lithography was done with previous recipe.
- Hardbake at 120°C for 20 minutes.
- Wet etching: 10:1 BOE for 20 minutes.
- Results: Resist failed because BOE is too aggressive. Increase the thickness of resist could help, but it would compromise the lithography quality. The solution is to add a metal layer between resist and oxide.

Trial #3 - adding Cr layer

- Wet oxidation at 1100°C for 30 minutes.
- Wafer with 400 nm oxide was sputtered with 150 nm Cr. Ar was set at 41 sccm. DC power was set to 200 W for 120 seconds. Cr was shiny like a mirror.
- Lithography was done with previous recipe.
- No hardbake was done.

- Wet etching: Cr etchant for 90 seconds. Undercut is 0.58 μm.
- Wet etching: 10:1 BOE for 20 minutes. Resist was left on the sample to protect Cr.
- Resist was pealing off and flying everywhere on the sample, as shown on Figure 3.12.
- Resist and Cr were stripped from the sample. Leaving patterned oxide on the wafer.
- Wafer was put in 70°C KOH solution (30 wt.%) to etch the V-groves. The temperature should be 80°C for desired etch rate.
- Oxide on the sample was etched in BOE.
- Piranha cleaning was done to prepare the sample for oxidation furnace.
- Results: Piranha cleaning removed all the photoresist on the surface. The results are sufficiently well.

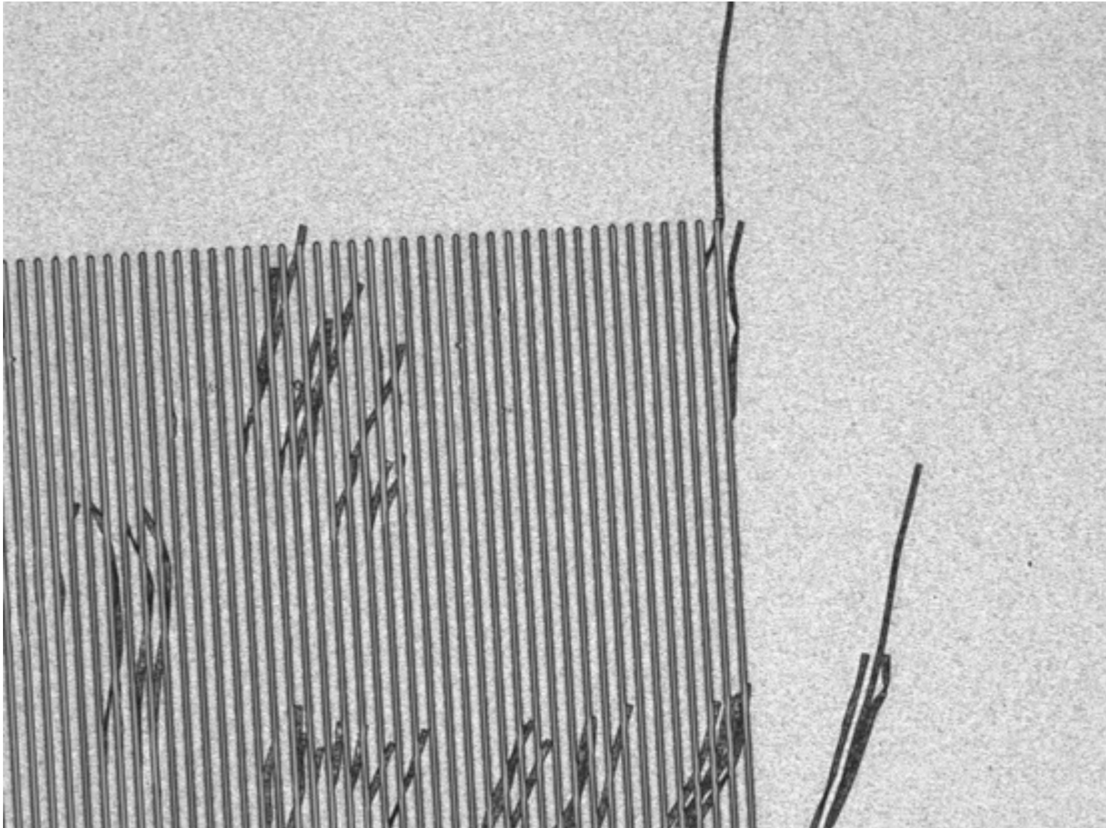

Figure 3.12: Sample after Cr etch and BOE. Photoresist was flying around.

3.3.3 Oxidation sharpening

Wet oxidation is a very standard process. The process developed for this is shown below.

Trial #1

- Wet oxidation at 1100°C. DI water: 85°C. N_2 flow rate: 1033 sccm.
- Results: The oxide growth rate was only 40% of the expected rate shown on the standard charts in textbooks due to a too small N_2 flow rate.

Trial #2 - increase N_2 flow rate

- Wet oxidation at 1100°C. DI water: 85°C. N_2 flow rate: 2520 sccm (100 on the scale).
- The oxide growth rate is the same, only 40% of the expected rate shown on the charts.
- Results: After studying the furnace model and the growth rate chart, we find that the chart is only valid for 3-inch wafer, while we were using smaller ¼ wafer pieces. Since we cut the wafer into quarters, the airflow in the furnace is different from the standard condition. It was hypothesized that adding 3-inch wafers between samples can help.

Trial #3 - add 3-inch wafers between each sample

- Wet oxidation at 1100°C. DI water: 85°C. N_2 flow rate: 2520 sccm.
- Two 3-inch wafers were placed on both ends as protective wafer. Several 3-inch wafers were placed between each quarter wafer sample, as shown in Figure 3.13. This ensures that airflow inside the furnace resembles the standard condition.
- The growth rate matched well with the chart. After 5 hours and 36 minutes, the oxide thickness is roughly 1μm, as expected from the charts.
- Oxide was etched in BOE.

- Results: The results were good. Figure 3.14 shows the results of oxidation sharpening.

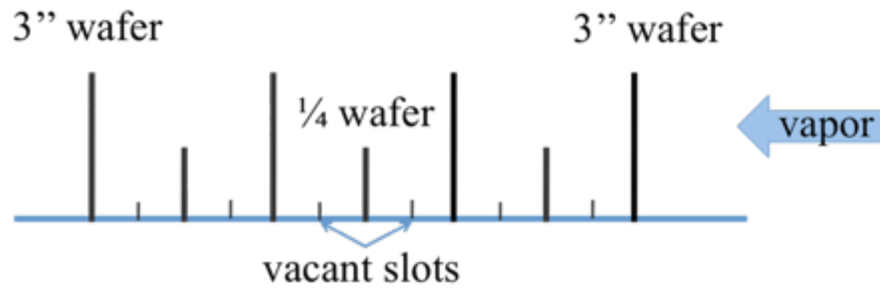

Figure 3.13: Wafer positions in the oxidation furnace.

Figure 3.14: Grating sample after oxidation sharpening.

3.4 Experimental Testing

The quality of the blazed grating was tested with an ellipsometer (M-2000D). Figure 3.15 shows the schematic setup of an ellipsometer. Polarized light is emitted to the surface of the grating samples with an incident angle θ_i, in the wavelength range 190 nm to 1000 nm. A photodetector measures the reflected light intensity at the reflective angle ($\theta_m = \theta_i$).

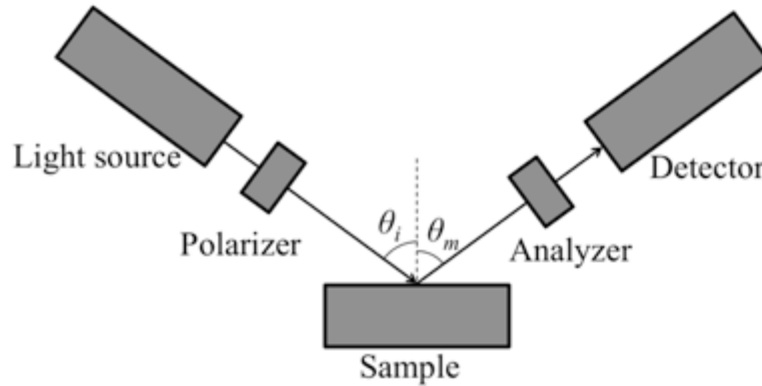

Figure 3.15: Schematic setup of an ellipsometer.

Six fabricated gratings were tested with the ellipsometer. All the gratings were tested at three incident angles: 45°, 46°, and 47°. The measured reflectivity vs. wavelength was plotted for each blazed grating (Figure 3.16, Figure 3.18, and Figure 3.20). Every peak on the plots corresponds to a constructive mode in the diffraction pattern, whose wavelength follows the grating equation given by:

$$d\left(\sin\theta_i + \sin\theta_m\right) = m\lambda \tag{3.1}$$

A MATLAB simulation using Equation 3.1 indicates the theoretical wavelengths of each possible peak at the tested angles. Results with different angles and grating periodicities are listed in Figure 3.17 3.19 3.21, and Table 3.1-3.3. By comparing simulated results with the peaks measured by ellipsometer, we can find a good match between the peak wavelengths, which indicates that the fabricated gratings are in a good quality.

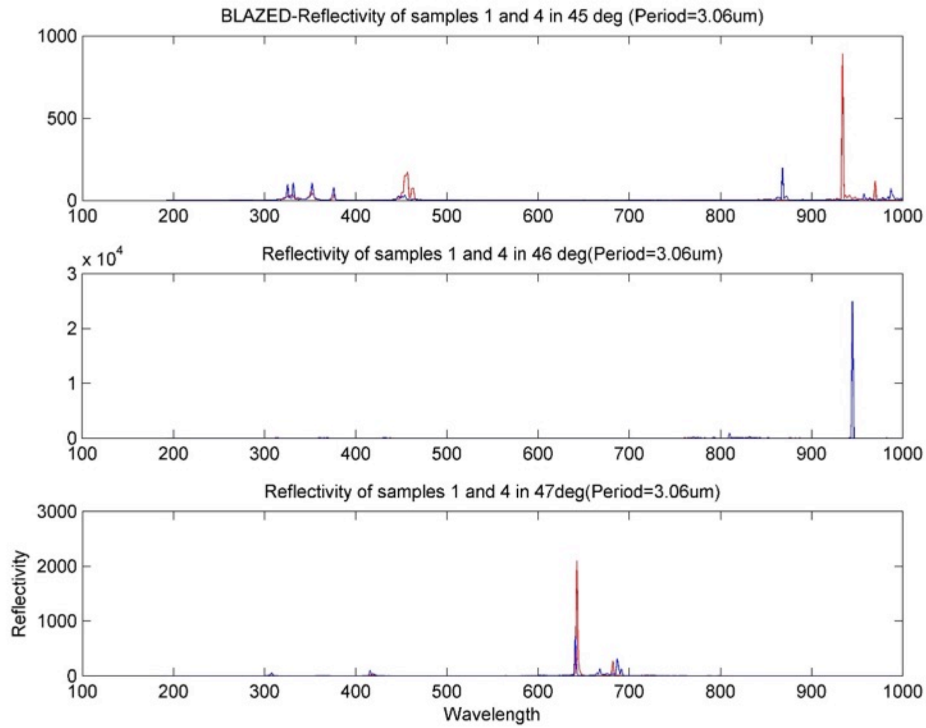

Figure 3.16: Measured reflectivity of blazed grating, d = 3.06 μm, at 45°, 46° and 47°.

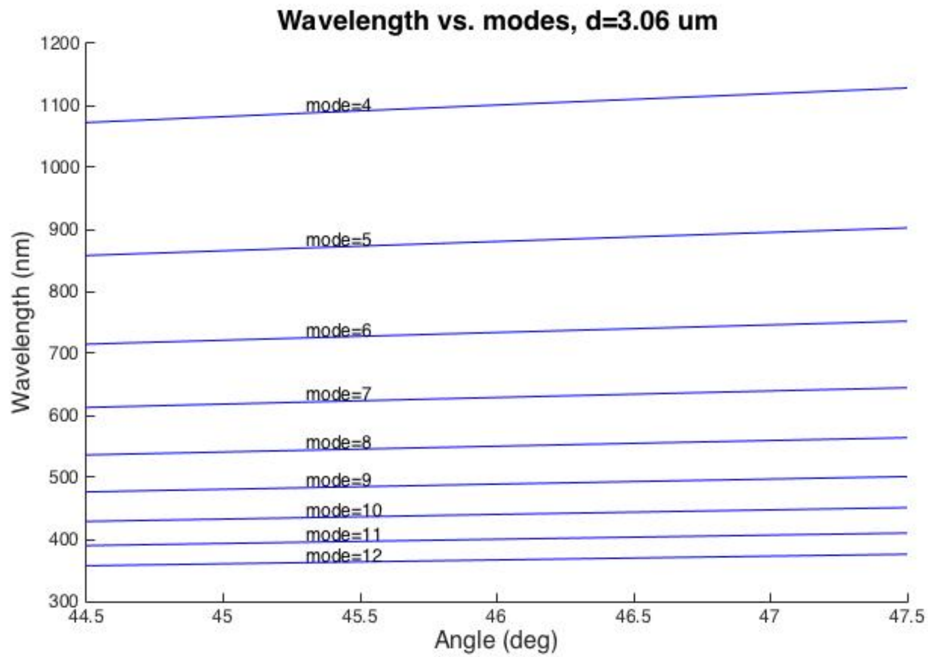

Figure 3.17: Constructive mode wavelength vs. angle, d = 3.06 μm.

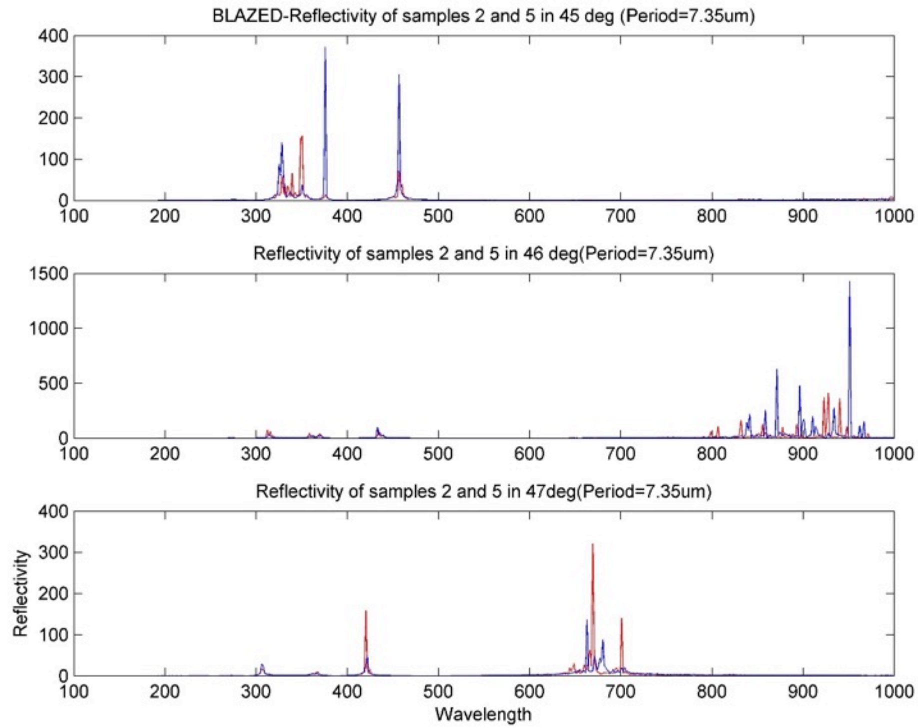

Figure 3.18: Measured reflectivity of blazed grating, d = 7.35 μm, at 45°, 46° and 47°.

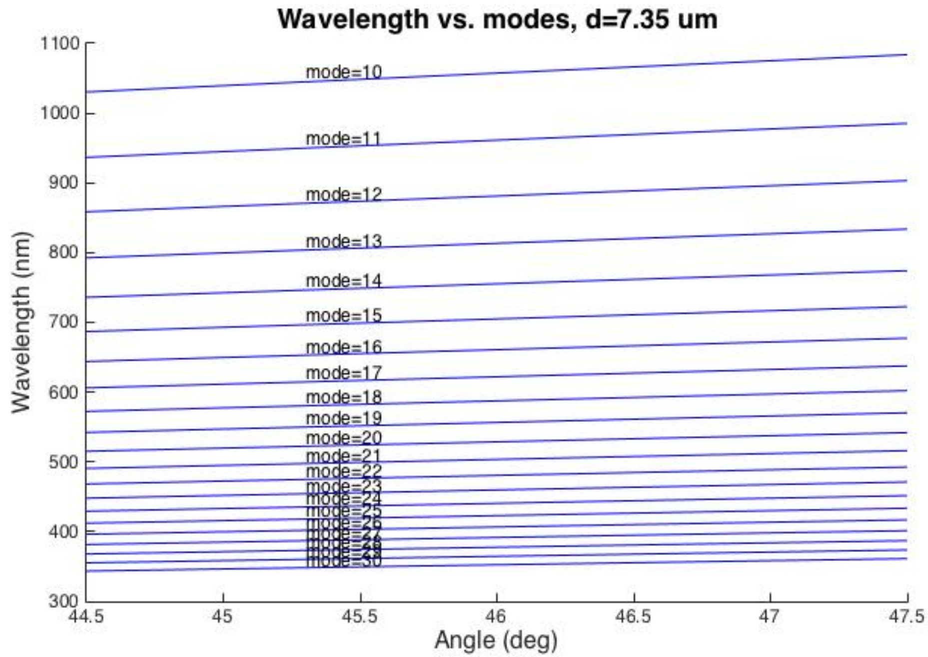

Figure 3.19: Constructive mode wavelength vs. angle, d = 7.35 μm.

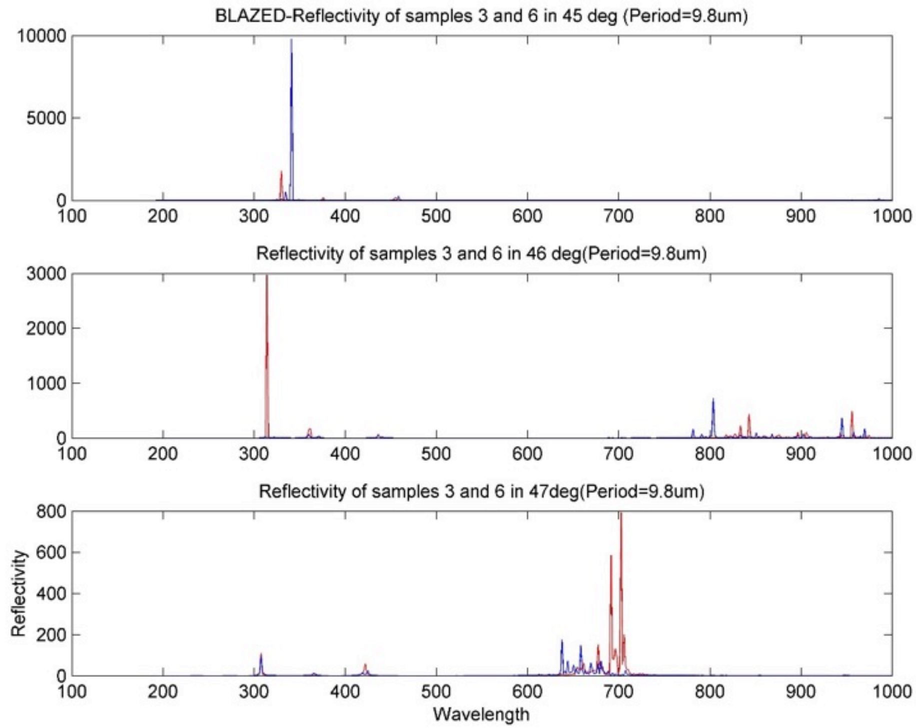

Figure 3.20: Measured reflectivity of blazed grating, d = 9.80 μm, at 45°, 46° and 47°.

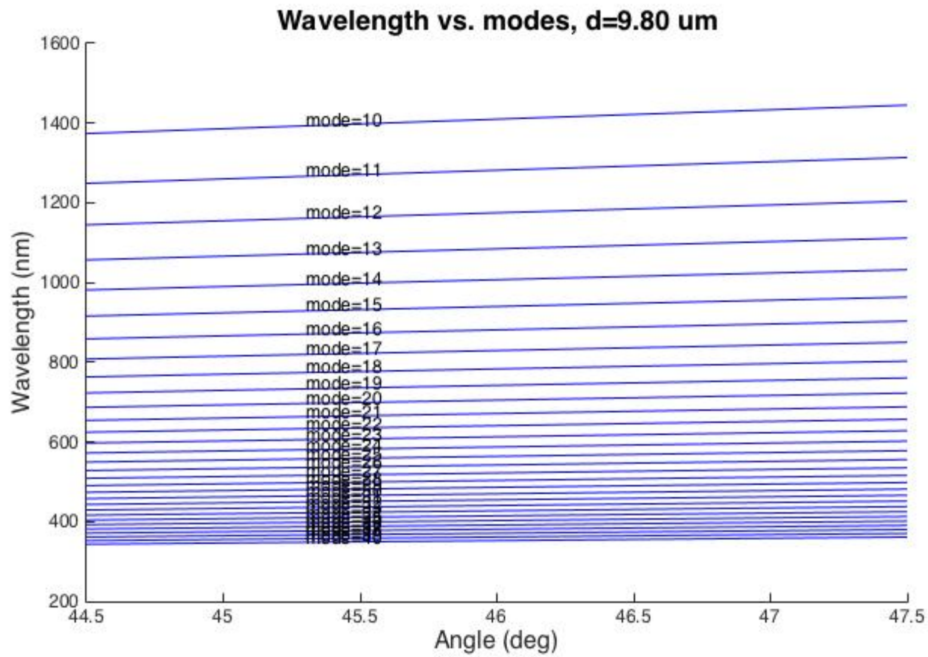

Figure 3.21: Constructive mode wavelength vs. angle, d = 9.80 μm.

Table 3.1: Wavelengths (nm) of constructive modes, $d = 3.06$ μm.

Angle		45°	46°	47°
Mode	1	4327	4402	4476
	2	2164	2201	2238
	3	1442	1467	1492
	4	1082	1101	1119
	5	865	880	895
	6	721	734	746
	7	618	629	639
	8	541	550	559
	9	481	489	497
	10	433	440	448
	11	393	400	407
	12	361	367	373

Table 3.2: Wavelengths (nm) of constructive modes, $d = 7.35$ μm.

Angle		45°	46°	47°
Mode	10	1039	1057	1075
	11	945	961	977
	12	866	881	896
	13	800	813	827
	14	742	755	768
	15	693	705	717
	16	650	661	672
	17	611	622	632
	18	577	587	597
	19	547	557	566
	20	520	529	538
	21	495	504	512
	22	472	481	489
	23	452	460	467
	24	433	441	448
	25	416	423	430
	26	400	407	413
	27	385	392	398
	28	371	378	384
	29	358	365	371
	30	346	352	358

Table 3.3: Wavelengths (nm) of constructive modes, $d = 9.80$ µm.

Angle		45°	46°	47°
Mode	13	1066	1085	1103
	14	990	1007	1024
	15	924	940	956
	16	866	881	896
	17	815	829	843
	18	770	783	796
	19	729	742	754
	20	693	705	717
	21	660	671	683
	22	630	641	652
	23	603	613	623
	24	577	587	597
	25	554	564	573
	26	533	542	551
	27	513	522	531
	28	495	504	512
	29	478	486	494
	30	462	470	478
	31	447	455	462
	32	433	441	448
	33	420	427	434
	34	408	415	422
	35	396	403	410
	36	385	392	398
	37	375	381	387
	38	365	371	377
	39	355	362	368
	40	346	352	358

3.5 Summary

In this chapter a successful fabricating process for blazed grating was developed. Fabricated blazed grating were experimentally tested in the 190-1000 nm wavelength range, and found to be good in quality.

Chapter 4: Micromirror design and fabrication

This chapter presents the Lorentz force actuated micromirrors developed for this project. This chapter will first present the design requirements, followed by COMSOL simulation of the micromirrors. A fabrication process was also developed for the micromirrors.

4.1 Lorentz force actuated micromirror design

The Lorentz force actuated micromirrors (Figure 1.3, reproduced as Figure 4.1 below) consist of a reflective mirror plate held by two silicon springs. A Lorentz coil was fabricated on the micromirror, and soldering pads were patterned on the silicon frame. The micromirror is actuated by Lorentz force, which occurs due to force coupling between the current $\boldsymbol{I}$ flowing in the Lorentz coil with an incident magnetic field. The Lorentz force $\vec{F}$ generated on the coil is given by Equation 2.4, where $\vec{\ell}$ is the vector for length of the wire, and $\vec{B}$ is the vector of magnetic field strength.

$$\vec{F} = I\vec{\ell} \times \vec{B} \tag{2.4}$$

As shown in Figure 4.1, for both the rotating and pop-up micromirrors, Lorentz force was generated on the section of Lorentz coil that is perpendicular to the magnetic field. The Lorentz force results in the rotational torque that actuates the micromirrors.

In experimental measurements the magnetic field was provided by a permanent magnet, taken from a hard drive. The magnetic field at 1 mm from the magnet was measured

to be 0.4 T (AlphaLab GM1-ST gaussmeter). This magnetic field strength was also used in the following COMSOL simulations of the Lorentz force actuated micromirrors.

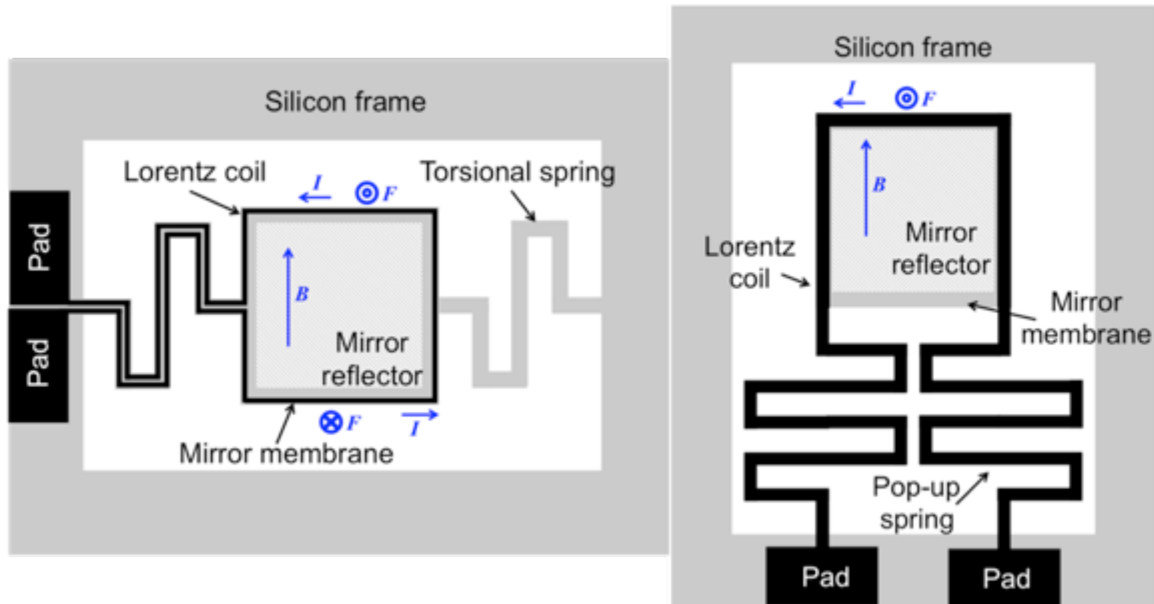

Figure 4.1: Schematic of micromirror and Lorentz force coupling.

4.1.1 Design requirements

There are several considerations for the design of the rotating and pop-up micromirrors. The relationships between each design consideration are discussed below:

1. Large mirror reflector area.

A larger reflector area gives a bigger cross-section area of the light path. This helps the photodiode of the optical detector receive a bigger signal, and thus increase the signal-to-noise ratio (SNR). A larger cross-section area of light path also means that with the same grating periodicity, more grating grooves are illuminated, and thus the resolution of the grating is increased (as discussed in Section 3.1.1). However, the mass of the micromirror (m) affects the resonance frequency of micromirror. With these considerations, the

micromirror was designed to be 3 mm × 3 mm, and the mirror reflector on the micromirror was made slightly smaller (2.5 mm × 2.5 mm) to leave enough space on for the Lorentz coils.

2. Large deflection angle.

As discussed in Section 3.1.1, with a larger deflection angle, the micromirror can work on a larger range of wavelengths. With a DC coil current, the maximum deflection angle is designed to be ± 10° for rotating micromirrors, and ± 20° for pop-up micromirrors.

A larger deflection angle can be achieved by increasing driving current, increasing the magnetic field strength, or decreasing the spring constant k of the silicon springs.

3. High resonance frequency.

It was desired that the micromirrors operate below their resonance frequency in the spectrometer. Considering the typical response time of a commercial thermopile photodetector (on the order of 50 Hz), the resonance frequency of the micromirrors was designed to be larger than 100 Hz, to avoid aging of device caused by resonance fatigue.

The resonance frequency of the micromirror is proportional to $\sqrt{\frac{k}{m}}$, where k is the spring constant of the silicon springs, and m is the mass of the micromirror. Since the mirror reflective area is fixed, a higher resonance frequency can be achieved by decreasing the thickness of the micromirror, or using stiffer springs (higher k).

4. Small energy consumption.

One of the biggest benefits of MEMS devices is low energy consumption. It was desired that the required operating power of the Lorentz force actuated micromirror should be in the order of 100 mW. The energy consumption includes the energy to drive the micromirror, and Joule heating in all the connection wiring. Softer springs (smaller k) would save energy and Joule heating can be reduced with smaller resistance of the Lorentz coil.

5. Electromigration.

Electromigration is the diffusion of metal ions under the impact of conducting electrons, and could cause failure of wires over time. Electromigration can be reduced with a lower current density, a lower Joule heating, and a better heat dissipation (increase device and wiring thickness).

6. Low cost fabrication of thin micromirror.

In order to bring down the fabrication cost, a thin membrane is back etched from a silicon wafer, instead of using an SOI wafer. This process limited the mirror to be no thinner than 10 µm, so that it is strong enough to survive all the fabrication processes.

7. High reliability and long lifetime of moving mirror.

Long term and reliable motion is required. In order to enable this, single crystal silicon was selected for the micro-springs. This was enabled by etching the micro-springs directly from the silicon wafer as part of the fabrication process.

Table 4.1 summaries the above design requirements in relation to each other. The key in the micromirror design is to find a proper spring constant k for both the rotating and pop-up micromirrors.

Table 4.1: Relationships between design considerations and parameters.

Design considerations	Parameters				
	Mass	Current	Spring constant	Resistance	Thickness
Mirror reflective area	↑				
Deflection angle		↑	↓		
Resonance frequency	↓		↑		↓
Energy consumption	↓	↓	↓	↓	
Electromigration		↓		↓	↑

4.1.2 Rotating micromirror spring design and COMSOL simulation

The design of the springs defines the spring constant *k*, which has the biggest influence on the performance of the Lorentz force actuated micromirror. Both torsion bar and S-shaped springs are considered. Theoretical study, simulation set-up and simulation results are discussed for each section below.

4.1.2.1 Torsion bar

In the first design, torsion bars were considered as springs for the rotating micromirrors. Figure 4.2 illustrates the torsion bar and its basic parameters. The deflection angle for a rectangle torsion bar is given by the equation:

$$\phi = \frac{T \cdot bar_{length}}{c_2 \cdot bar_{width} \cdot Membrane_{thickness}^3 G} \tag{4.1}$$

where bar_{width} and $Membrane_{thickness}$ are the width and thickness of the torsion bar respectively, *T* is the magnitude of the torques applied to the torsion bar, and *G* is the shear modulus, which is related to the torsion bar material. The coefficient c_2 depends upon the aspect ratio of the torsion bar, $bar_{width}/Membrane_{thickness}$. These two parameters are subject to fabrication limitations.

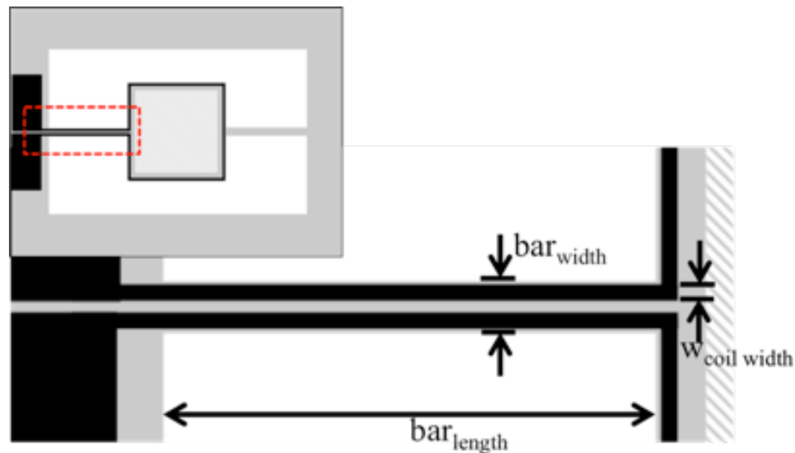

Figure 4.2: Parameters in torsion bar spring, rotating micromirror.

Considering the aspect ratio of the torsion bar, the coefficient c_2 follows the equation given by:

$$c_2 = \frac{1}{3}\left(1 - 0.630\frac{Membrane_{thickness}}{bar_{width}}\right), \left(bar_{width} / Membrane_{thickness} \geq 5\right) \tag{4.2}$$

The spring constant κ of a torsion bar is the ratio of torque over deflection angle within elastic limit, and is given by Equation 4.3.

$$\kappa = \frac{T}{\phi} = \frac{c_2 \cdot bar_{width} \cdot Membrane_{thickness}^3 G}{bar_{length}} \tag{4.3}$$

Thus, the spring constant κ is proportional to $\frac{bar_{width} \cdot Membrane_{thickness}^3}{bar_{length}}$.

A COMSOL model was built to simulate the rotating micromirror with torsion bars. The first design parameter values selected are listed in Table 4.2.

Table 4.2: Parameters of torsion bar supported rotating micromirror.

Parameter	**Value**	**Description**
$Area_{mirror}$	3 mm × 3 mm	Micromirror width and height
$Membrane_{thickness}$	20 µm	Silicon membrane thickness
bar_{width}	100 µm	Torsion bar width
bar_{length}	2 mm	Torsion bar length
$w_{coil\ width}$	30 µm	Lorentz coil wire width
$w_{coil\ thickness}$	1 µm	Lorentz coil wire thickness
B	0.4 T	Magnetic field
I_{coil}	50 mA	Current in the Lorentz coil

COMSOL simulation: Resonance frequency study

Resonance frequency and deflection angle is simulated using COMSOL's solid mechanics module. A fixed constraint is applied to the ends of torsion bars. To simulate Lorentz force on the edges of micromirror, the opposing sides of the micromirror are loaded

with specified opposing forces per unit length (edge load) of values $\pm B \times I_{coil}$ along the z-axis.

Resonance frequency is computed with COMSOL's Eigen frequency study. The first Eigen frequency (as shown in Figure 4.3) is 1163 Hz in the rotational mode. The resonance frequency of this rotating micromirror meets the design requirements.

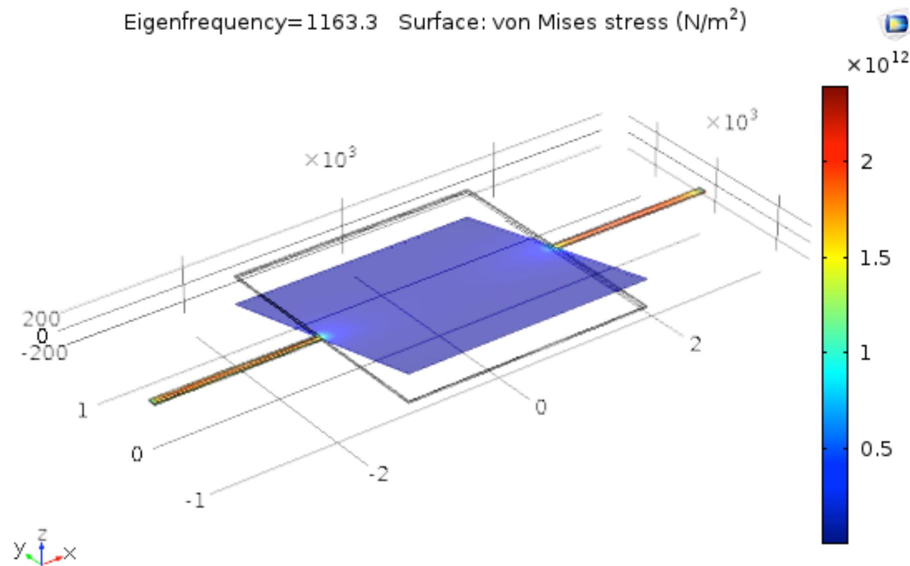

Figure 4.3: First Eigen frequency for torsion bar supported rotating micromirror.

COMSOL simulation: Temperature study

Operation temperature was simulated using COMSOL. An airbox was built surrounding the micromirror and springs. Three physics are used in temperature simulation: electric currents, heat transfer in solids, and heat transfer in fluids. In the stationary study, the results showed that the micromirror will be heated to 147°C, with a 50 mA DC current. In the time dependent study, the current increases from 0 mA to 50 mA from time $t = 0$ s. The time dependent study results (Figure 4.4) showed that it takes over 5 seconds for temperature to stabilize.

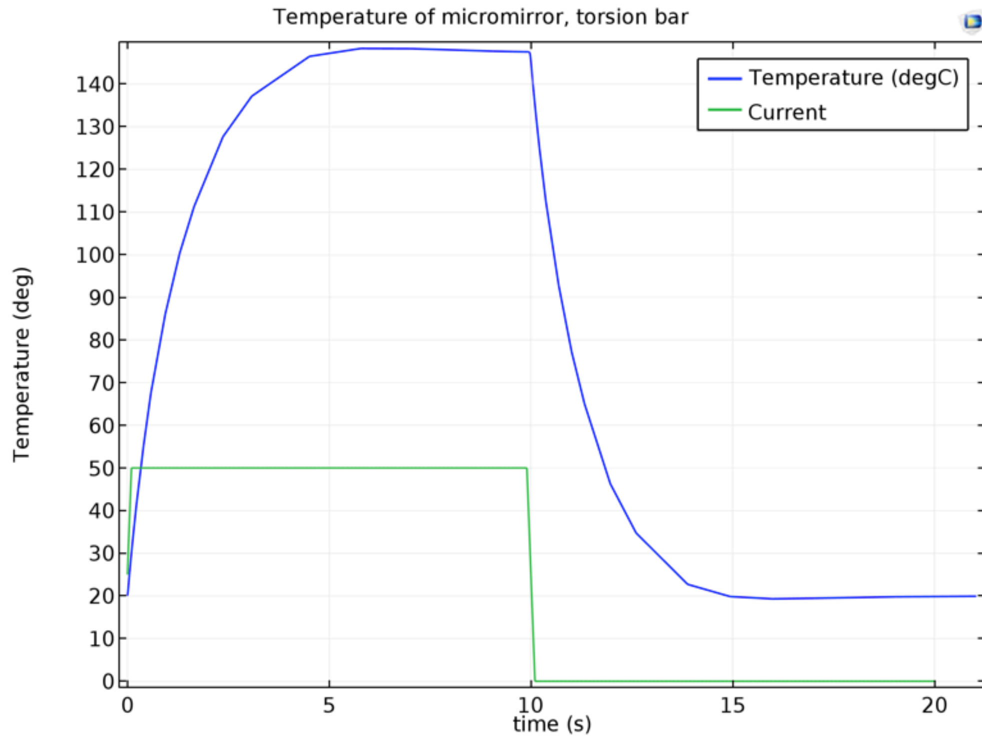

Figure 4.4: Temperature for torsion bar supported rotating micromirror.

COMSOL simulation: Deflection angle study

The deflection angle is computed with COMSOL's stationary study. The parameter I_{coil} was swept from 0 mA to 65 mA with a step of 5 mA. A point probe is placed at the corner of the micromirror, and at this point COMSOL logs the displacement *disp* of the probe point. The deflection angle of the micromirror is calculated from the equation given by:

$$\theta = 2 * \sin^{-1} \frac{disp}{Area_{mirror}} \tag{4.4}$$

Figure 4.5 illustrates the deflection angle versus current. From this figure, we can see that the deflection angle is proportional to the current, which means that the torsion bar is still in the linear range.

As we can see in Figure 4.5, the maximum deflection angle is very small (below 1°). It was decided that a simple torsion bar could not satisfy the design needs, and so an S-shaped torsion spring was then considered.

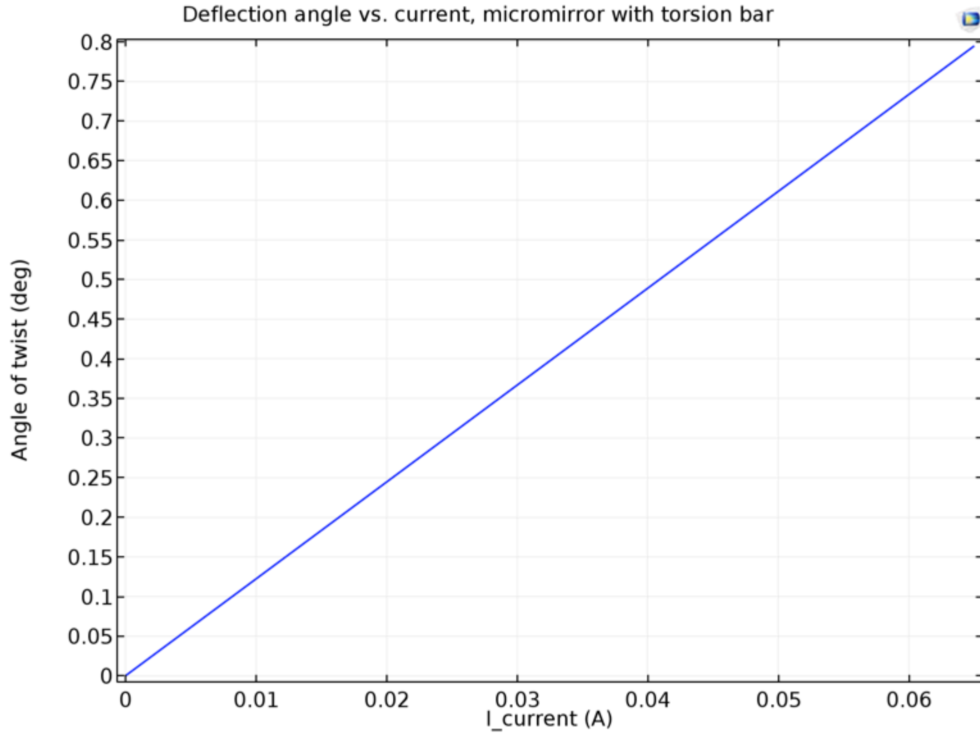

Figure 4.5: Deflection angle vs. current for torsion bar supported rotating mirror.

4.1.2.2 S-shape torsion spring

An S-shape spring was considered, due to its potential for greater bending angle. Compared with torsion bars, S-shape springs have a smaller spring constant, and are more compact. Figure 4.6 illustrates the S-shape torsion spring shape and its basic parameters.

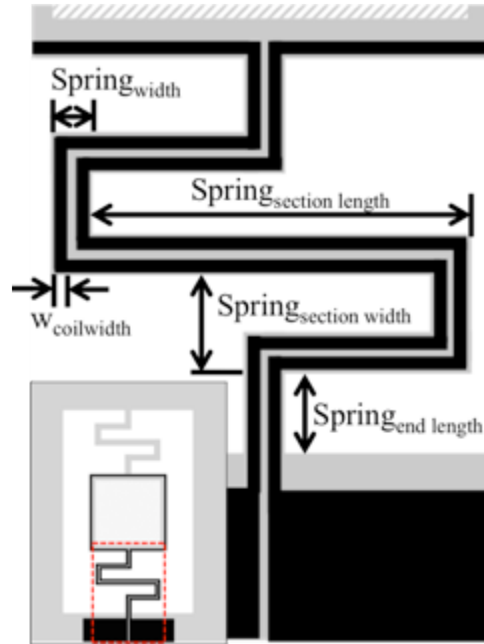

Figure 4.6: Parameters in S-shape spring, rotating micromirrors.

Due to the structure of S-shape springs, during torsional movement the spring has multiple torsional rotating segments perpendicular to each other. Therefore, a complete analytical model of S-shape spring is complex. Therefore, COMSOL was used to simulation the structure. These simulations revealed the S-shape spring characteristics. Parameter values for this simulation are listed in Table 4.3.

Table 4.3: Parameters of S-shape spring supported rotating micromirror.

Parameter	**Value**	**Description**
$Area_{mirror}$	3 mm × 3 mm	Micromirror width and height
$Membrane_{thickness}$	12 µm	Silicon membrane thickness
$Spring_{width}$	100 µm	S-shape spring width
$Spring_{section\ length}$	1.5 mm / 2 mm / 2.5 mm	Length of each spring section
$Spring_{section\ width}$	300 µm	Width of each spring section
$Spring_{end\ length}$	300 µm	Length of end section
$w_{coil\ width}$	30 µm	Lorentz coil width
$w_{coil\ thickness}$	1 µm	Lorentz coil thickness
B	0.4 T	Magnetic field
I_{coil}	50 mA	Current in the Lorentz coil

COMSOL simulation: Resonance frequency study

COMSOL's solid mechanics physics and Eigen frequency study showed the micromirror with S-shape spring has a resonance frequency of 443 Hz for $Spring_{section\ length}$ = 1.5 mm, 387Hz for $Spring_{section\ length}$ = 2 mm, and 346 Hz for $Spring_{section\ length}$ = 2.5 mm.

COMSOL simulation: Temperature study

Temperature is simulated with electric currents, heat transfer in solids, and heat transfer in fluids. With 50 mA DC current, the center of micromirror will be heated to 293°C. Time dependent study results (Figure 4.7) show that the heating and cooling time for S-shape spring is over 35 seconds.

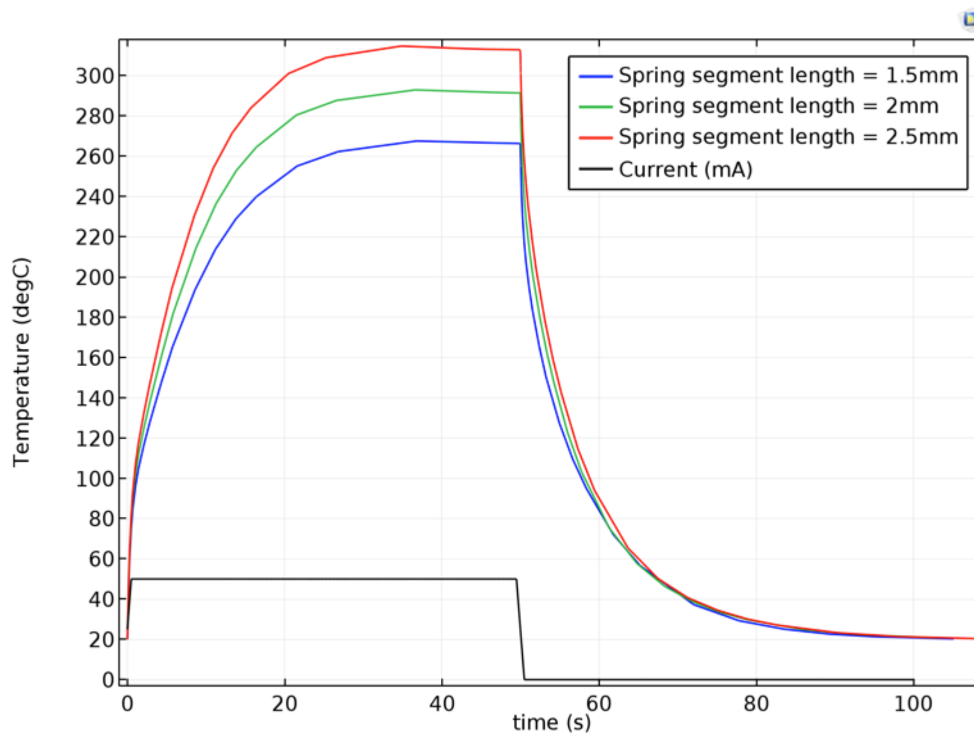

Figure 4.7: Temperature for S-shape spring supported rotating micromirror.

COMSOL simulation: Deflection angle study

The deflection angle is also calculated by COMSOL by placing a virtual probe on the corner the micromirror. Figure 4.8 illustrates the deflection angle with 0 mA to 65 mA current. The deflection angle reaches 10° when the current is above 55 mA.

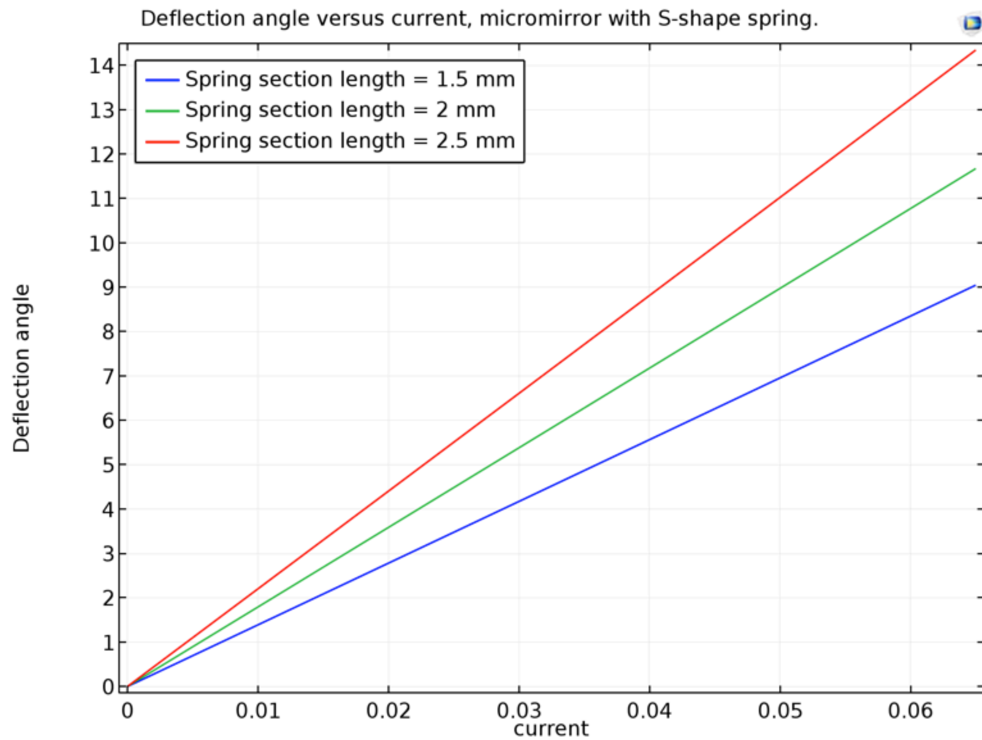

Figure 4.8: Deflection angle vs. current for S-shape spring supported rotating micromirror.

From the simulation results above, we can see that the performance of S-shape spring supported rotating mirrors fully satisfy the design requirements given in Section 4.1.1. The parameters of the S-shape springs (listed in Table 4.3) were used in the mask design of rotating micromirrors.

4.1.3 Pop-up micromirror spring design and COMSOL simulation

Similar to rotating micromirrors, both cantilevers and S-shape springs are considered in the design of pop-up micromirrors. Theoretical study, simulation set-up and simulation results are discussed for each module.

4.1.3.1 Cantilever

In the first design, cantilevers are used as the spring elements for the pop-up micromirrors. Figure 4.9 illustrates the basic parameters of the pop-up micromirror cantilever:

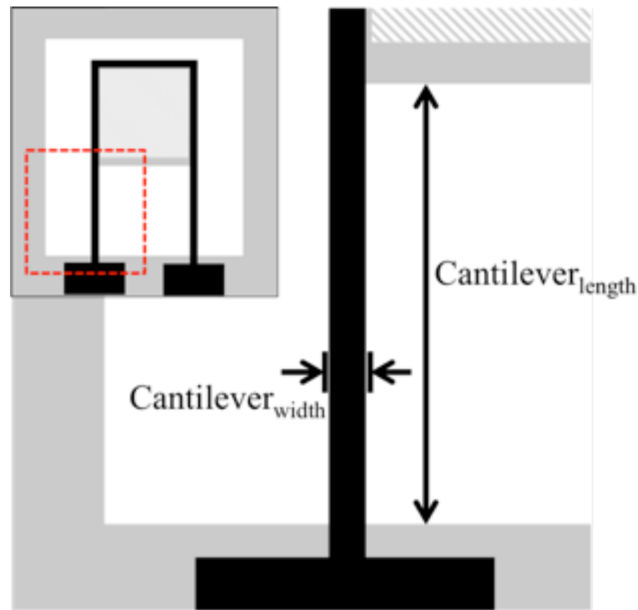

Figure 4.9: Parameters of cantilever, pop-up micromirror.

In mechanics of materials, the deflection for a rectangle cantilever with end load is described with Equation 4.5.

$$y(x) = \frac{F}{6EI}\left(3x^2 Cantilever_{length} - x^3\right) \tag{4.5}$$

In this equation, F is the force applied to the end of cantilever, and E is the Young's modulus, and I is the moment of inertia. The spring constant k of a cantilever is the ratio of force over deflection within elastic limit, and is given by:

$$k = \frac{3EI}{Cantilever_{length}^3} \tag{4.6}$$

As shown in the equations above, the deflection of an end-loaded cantilever is a linear function of force F. The angle of the micromirror plate is calculated from the derivate of Equation 4.5 at the end of the cantilever, given by:

$$\theta = \arctan\left(\frac{2F \cdot Cantilever_{length}^2}{3EI}\right) \tag{4.7}$$

A COMSOL model is built to simulate the rotating micromirror with torsion bars. The parameter values are listed in Table 4.4.

Table 4.4: Parameters of cantilever supported pop-up micromirror.

Parameter	**Value**	**Description**
$Area_{mirror}$	3 mm × 3 mm	Micromirror width and height
$Membrane_{thickness}$	20 µm	Silicon membrane thickness
$Cantilever_{width}$	100 µm	Cantilever width / Lorentz coil width
$Cantilever_{lendth}$	2 mm	Cantilever length
$w_{coil\ thickness}$	1 µm	Lorentz coil thickness
B	0.4 T	Magnetic field
I_{coil}	50 mA	Current in the Lorentz coil

COMSOL simulation: Resonance frequency study

Resonance frequency and deflection angle is simulated with solid mechanics module. A fixed constraint is applied to the ends of torsion bars. To simulate Lorentz force on the edge of micromirror, an edge load, *B × I_current [N/m]* along z-axis, is applied to the further

edge of micromirror. Resonance frequency is computed with Eigen frequency study. The first Eigen frequency is at 314 Hz, on the pop-up mode (Figure 4.10).

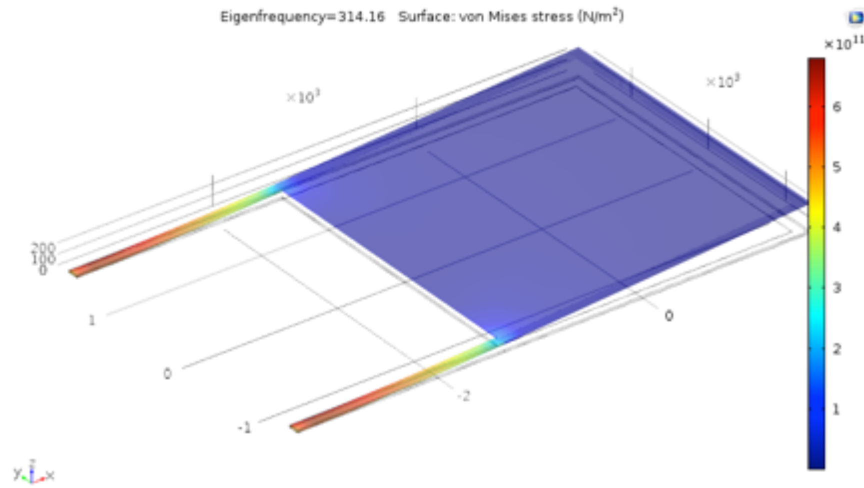

Figure 4.10: First Eigen frequency of cantilever supported pop-up micromirror.

COMSOL simulation: Temperature study

Temperature was calculated with COMSOL by building an airbox surrounding the micromirror and cantilevers. In the stationary study, results show that the micromirror will be heated to 50°C for a 50 mA DC current. As shown in Figure 4.11, time dependent study show that it takes over 5 seconds for temperature to stabilize.

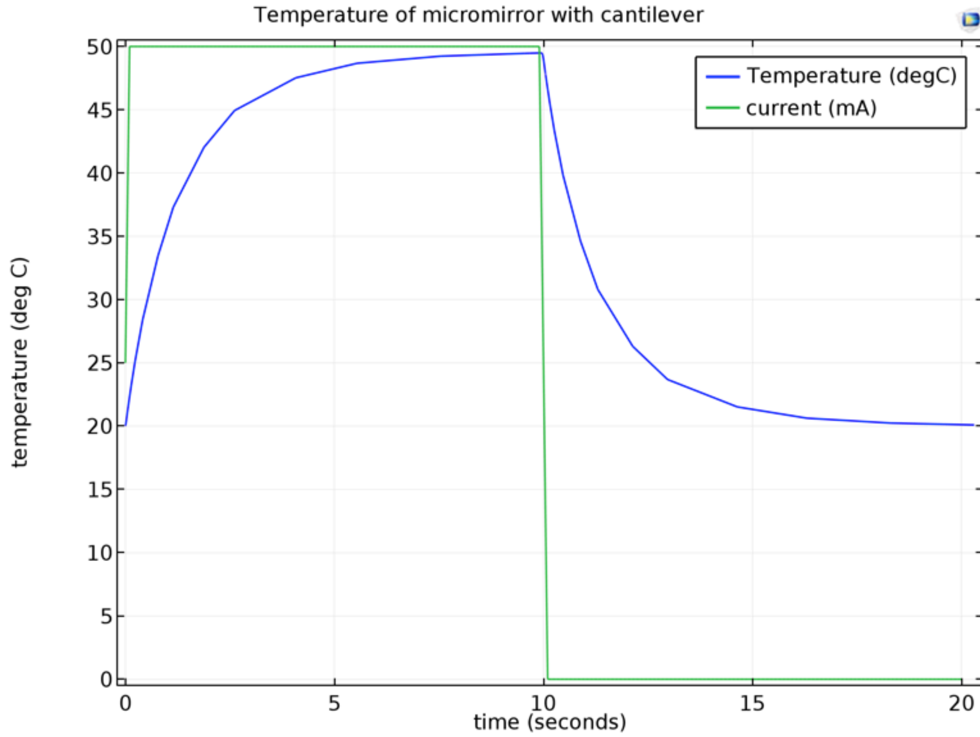

Figure 4.11: Temperature of cantilever supported pop-up micromirror.

COMSOL simulation: Deflection angle study

Deflection of the micromirror is computed with stationary study in COMSOL. The parameter *I_current* is swept from 0 mA to 65 mA with a step of 5 mA. A point probe *p1* is placed at the further end of micromirror, and another probe *p2* is placed at the end of cantilever. The angle of micromirror is calculated from displacement of probes, $disp_{p1}$ and $disp_{p2}$:

$$\theta = \sin^{-1} \frac{disp_{p1} - disp_{p2}}{Area_{mirror}} \tag{4.8}$$

Figure 4.12 illustrates the deflection angle versus current. From this figure, we can see that the deflection angle is proportional to current.

Unfortunately, the maximum deflection angle using the simple cantilever spring is too small for the pop-up micromirror to operate as an optical switch. Accordingly, S-shaped springs were considered.

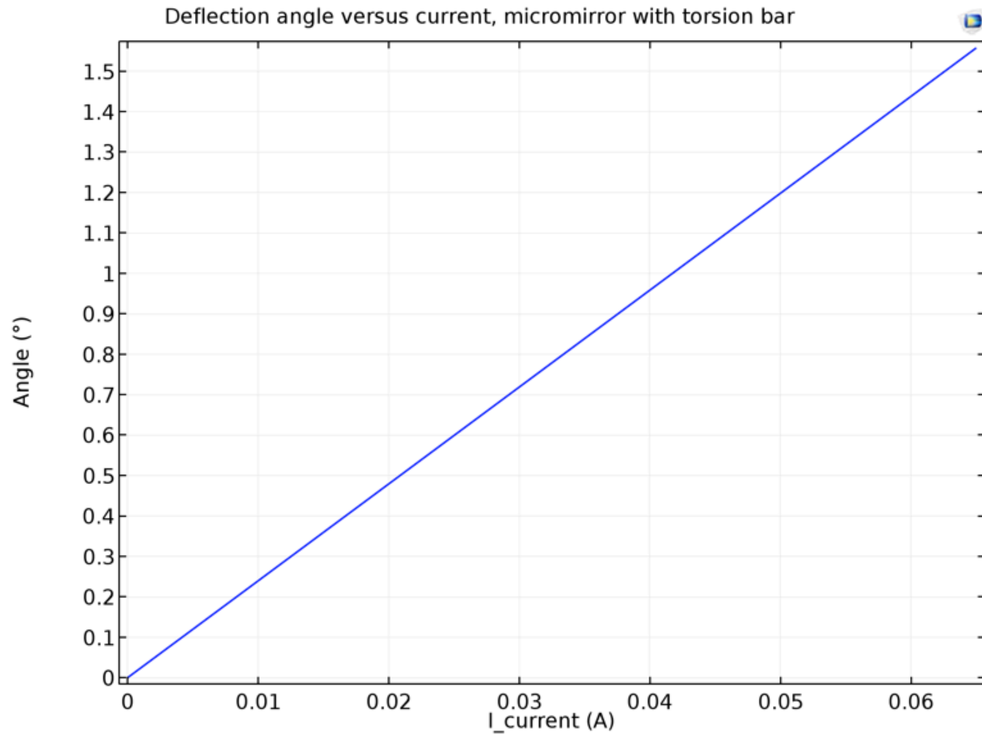

Figure 4.12: Deflection angle vs. current for cantilever supported pop-up micromirror.

4.1.3.2 S-shape spring

S-shape spring is also considered for pop-up micromirrors. Figure 4.13 illustrates the basic parameters of the spring:

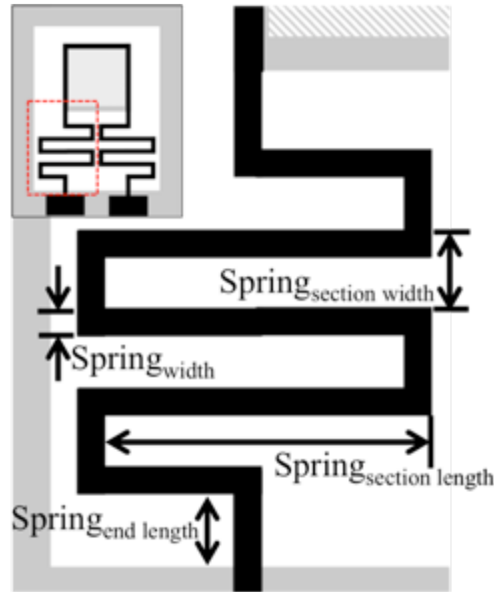

Figure 4.13: Parameters of the S-shape spring, pop-up micromirror.

Due to the structure of S-shape springs, during S-shape spring torsional movement, the spring has multiple torsional rotating segments, perpendicular to each other. Therefore, a complete analytical model of S-shape spring is complex. COMSOL simulation results are done to reveal the S-shape spring characteristics. Parameter values are listed in Table 4.5.

Table 4.5: Parameters of S-shape spring supported pop-up micromirror.

Parameter	**Value**	**Description**
$Area_{mirror}$	3 mm × 3 mm	Micromirror width and height
$Membrane_{thickness}$	12 µm	Silicon membrane thickness
$Spring_{width}$	100 µm	S-shape spring width / Lorentz coil width
$Spring_{section\ length}$	1.5 mm / 2 mm	Length of each spring section
$Spring_{section\ width}$	300 µm	Width of each spring section
$Spring_{end\ length}$	300 µm	Length of end section
$w_{coil\ thickness}$	1 µm	Lorentz coil thickness
B	0.4 T	Magnetic field
I_{coil}	50 mA	Current in the Lorentz coil

COMSOL simulation: Resonance frequency study

From solid mechanics physics and Eigen frequency study, micromirror with S-shape spring has a resonance frequency of 107 Hz for $Spring_{section\ length}$ = 2 mm, and 121 Hz for $Spring_{section\ length}$ = 1.5 mm.

COMSOL simulation: Temperature study

Temperature is simulated with electric currents, heat transfer in solids, and heat transfer in fluids. With 50 mA DC current, the center of micromirror will be heated to 135°C. The heating and cooling time (Figure 4.14) for S-shape spring is over 40 seconds.

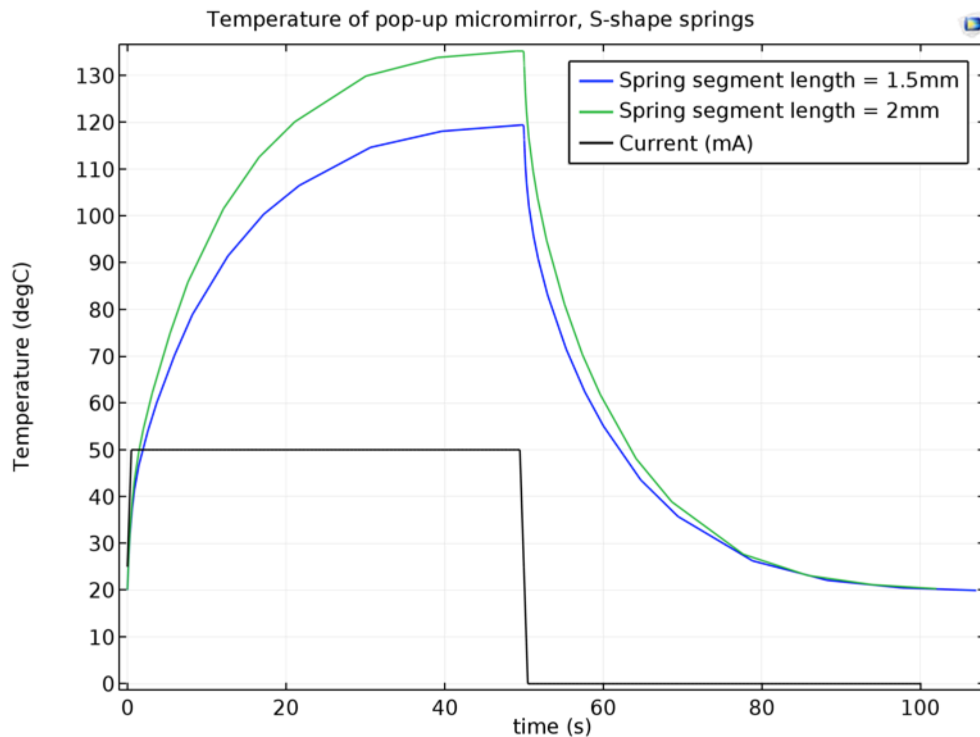

Figure 4.14: Temperature for S-shape spring supported pop-up micromirror.

COMSOL simulation: Deflection angle study

Figure 4.15 illustrates the angle of micromirror with 0 mA to 65 mA current. From this figure, we can see that the deflection angle is proportional to current. The maximum deflection angle reaches 20° at a driving current of 60 mA.

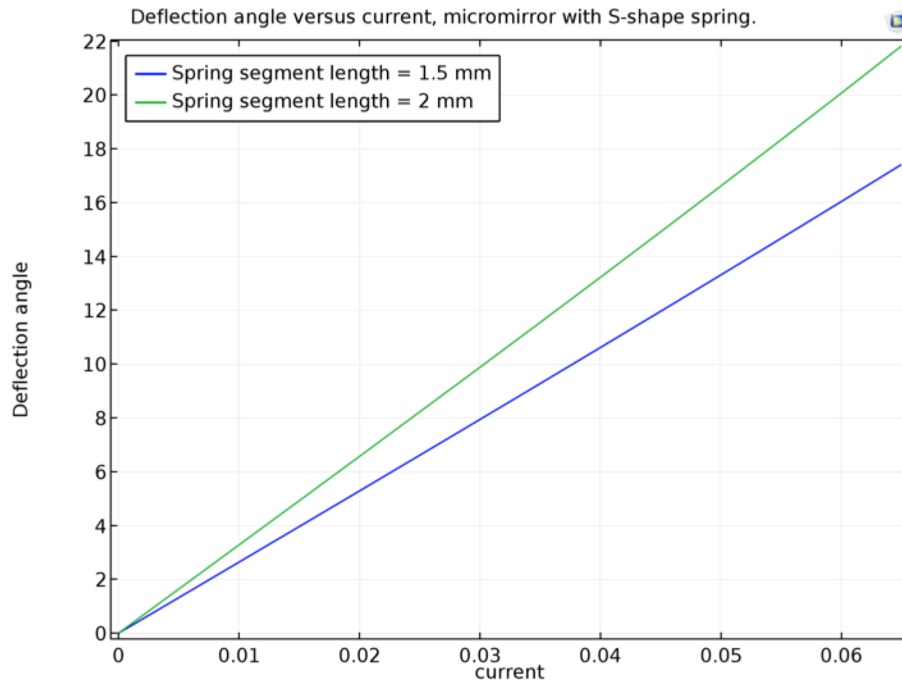

Figure 4.15: Deflection angle vs. current for S-shape spring supported pop-up micromirror.

From the simulation results above, we can see that the performance of S-shape spring supported pop-up mirrors fully satisfy the design requirements. The parameters of the S-shape springs (listed in Table 4.5) were used in the mask design of pop-up micromirrors.

4.2 MEMS micromirror fabrication design

MEMS mirrors were fabricated on 525 µm thick, <100> silicon nitride wafers that are coated with 200 nm LPCVD silicon nitride. The nitride layer acts as mask for silicon etch. It

also acts as the electrical insulation layer. Figure 4.16 illustrates the lithography masks used for fabricating the MEMS micromirrors. The fabrication steps are illustrated in Figure 4.16.

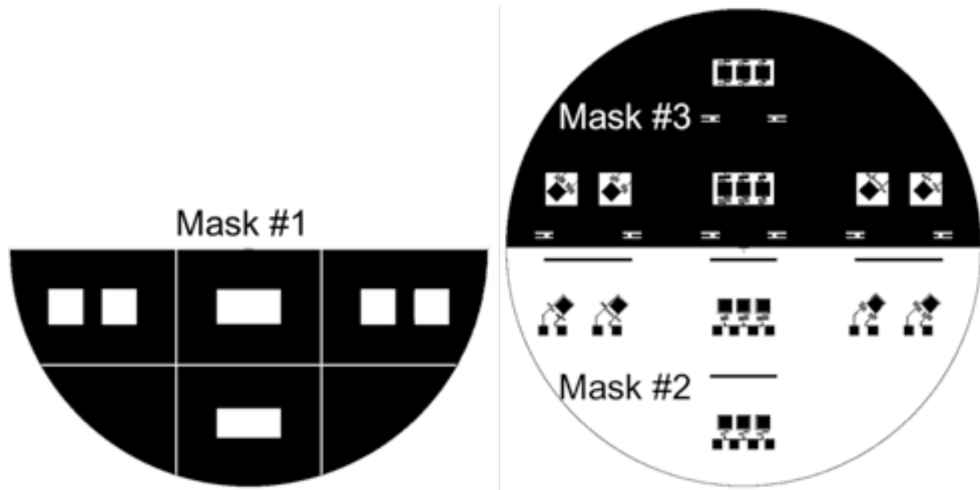

Figure 4.16: MEMS micromirror mask. Mask #1 is the back etch mask. Mask #2 is the wire and mirror reflector mask. Mask #3 is the front etch mask to define the mirror and spring shapes.

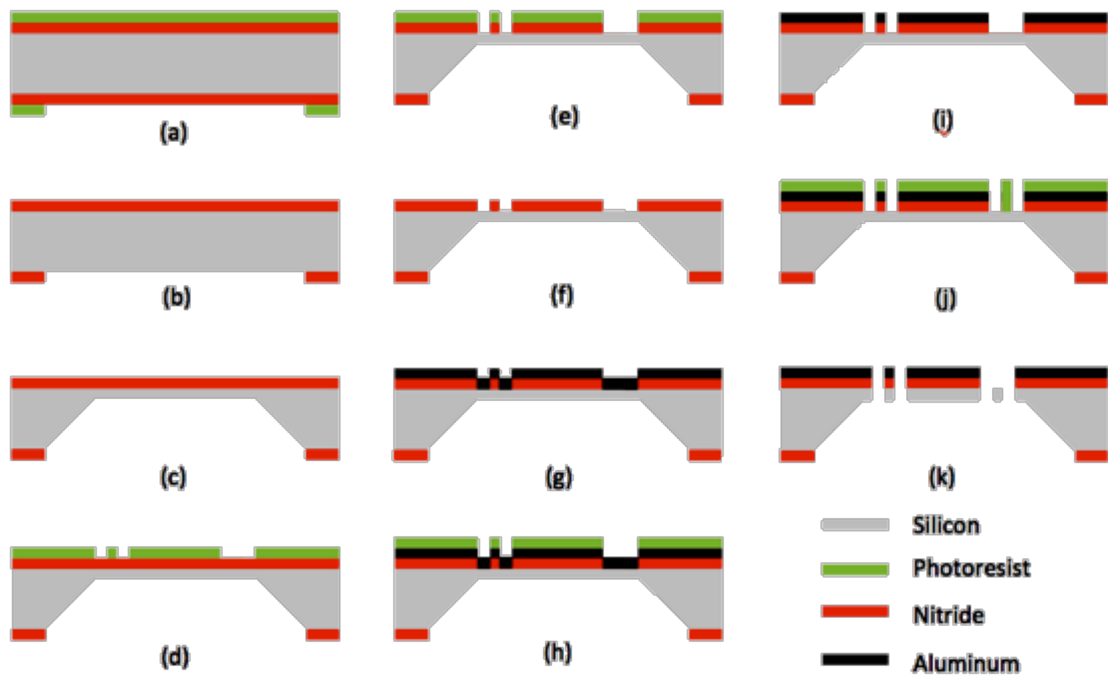

Figure 4.17: MEMS mirror fabrication steps.

- Figure 4.17a (Mask #1): Photoresist is spun on the backside of the wafer. This photoresist is patterned with Mask #1 (back etch mask). A thick layer of resist is also coated on the frontside of the wafer for protection.
- Figure 4.17b: Nitride on the backside of the wafer is etched with plasma etch in the Trion plasma etcher for 120 seconds. Pressure was 35 mT, CF_4 45 sccm, O_2 5 sccm. ICP power was 300 W, and RIE 80 W. The patterned nitride layer is used as mask in the KOH etch. After nitride plasma etch, photoresist is removed to avoid contaminating KOH solution.
- Figure 4.17c: KOH wet etch is done to etch the backside silicon, leaving about a 20 μm silicon membrane remaining. The desired mirror thickness is 12 μm. However, this thickness could be too fragile for the following process.
- Figure 4.16d (Mask #3): A two-side lithography is done using Mask #3 (front etch mask). An infrared light helps to align the back-etched cavity with the patterns on the frontside.
- Figure 4.17e: Nitride plasma etch to give step edges that helps alignment of Mask #2.
- Figure 4.17f: Photoresist is removed to prepare for the next step.
- Figure 4.17g: Thermal evaporation is done to deposit aluminum on the frontside of the wafer. This gives a shiny and low-stress aluminum layer, which is ideal for mirror reflector.
- Figure 4.17h (Mask #2): Photoresist is spun and patterned using Mask#2 (wire and mirror reflector mask). The patterns cannot directly align to back-etched cavity, due to the opaque aluminum layer. The step edges on the nitride layer provide guidelines for alignment.
- Figure 4.17i: Aluminum wet etching to pattern the aluminum layer into the shape of mirror reflector, Lorentz coil, and soldering pads. Photoresist is then removed to prepare for the next step.

- Figure 4.17j (Mask #3): A thick layer of resist is spun and patterned with Mask #3 (front etch mask).
- Figure 4.17k: Before mirror releasing, the silicon membrane is further etched from the backside to reach the desired mirror thickness. This is done in plasma etch in the Trion plasma etcher. Native oxide etch for 15 seconds with pressure 50mT, CF4 at 45 sccm, ICP 300 W, RIE 25 W. Silicon etch for 200 seconds, with pressure 50mT, SF6 at 30 sccm, ICP 300 W, RIE 25 W. Then, the wafer is flipped over, and another silicon plasma etch is done to punch through the membrane and release the mirror and springs.

4.3 MEMS micromirror fabrication trials

4.3.1 Backside nitride etch

The development of the process for the etching of the backside nitride is discussed below.

Trial #1

- A 4-inch double-sided wafer with 100nm Si_3N_4 was cleaned in piranha etch.
- Lithography was done with the back etch mask, using the previous recipe. Photoresist was spun at 6000 rpm. Hardbake at 120°C for 20 minutes.
- In order to protect the nitride on the frontside, a layer of photoresist was coated. During the spinning and developing process, blue tape was used on the other side of the wafer to prevent scratches from the vacuum chunk.
- Cutting the wafer into pieces will result in uneven photoresist thickness. So in order to pattern both halves of the wafer using back etch mask without cutting, multiple

exposure technique was used in the litho: The grating mask is covered during multiple exposures. Half of the wafer was exposed and developed as usual. Development won't affect the photoresist that was unexposed. Expose the other half of the wafer with same recipe, and develop. Finish off the litho with hard bake.

- Nitride was etched for 120 seconds in the Trion plasma etcher. Pressure was set at 35 mT, CF_4 at 45 sccm, O_2 at 5 sccm. ICP power was 300 W, and RIE 80 W.
- Results: Resist was too thin. Some of the plasma ions punched through the resist, and attacked nitride underneath.

Trial #2

- A 4-inch double-sided wafer with 100 nm Si_3N_4 was cleaned in piranha etch.
- Lithography was done with back etch mask, using previous recipe. Photoresist was spun at 3000 rpm. Hardbake at 120°C for 20 minutes.
- Photoresist was coated on the frontside of wafer. Blue tape was used to prevent scratches.
- The multiple exposure technique was used as described above.
- Nitride was etched using same recipe as previous trial.
- Photoresist was removed.
- Results: 200 nm of nitride was etched successfully. The resist was etched a little bit as well. The silicon substrate was attacked a bit as well, but this didn't affect the KOH etch in the next step.

4.3.2 Backside silicon etch

KOH etch is a standard process. In order to get a more precise membrane thickness, the etching was done in several steps instead of one long etch. Etch rate was calculated after each time. The 425 μm wafer was etched halfway through in the first etch. In the following

etches, the wafer was again etched in several steps, until the membrane was about 50 μm thick, then 30 μm, and finally 20 μm. Figure 4.18 shows the sample after the first KOH etch.

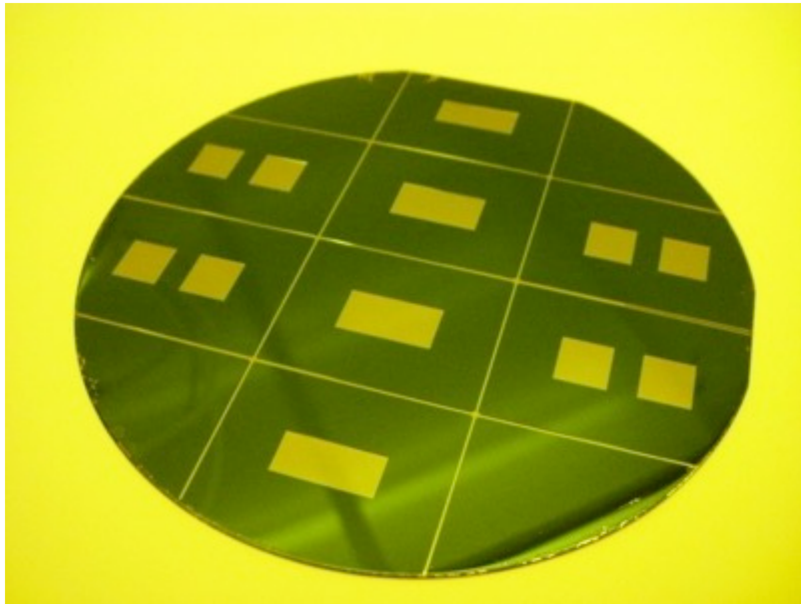

Figure 4.18: Sample after first KOH etch.

Trial #1

- The wafer was etched in 70°C KOH solution (30 wt.%) for 3 hours. The magnetic stirrer was rotating at 300 rpm in the solution.
- Etch rate was 0.64 μm/min.
- Results: The etch rate is much smaller than the desired etch rate 1 μm/min. This is caused by mistakenly using low KOH solution temperature. The desired etch rate should be 80°C instead of 70°C.

Trial #2

- The temperature of KOH solution was increased to 80°C. The wafer was etched in KOH solution for another 3 hours and 50 minutes. The magnetic stirrer rotated at 300 rpm in the solution.
- The etch rate was about 1 μm/min.

- The thickness of silicon membrane was etched to 20 μm. Note, the etched surface was not as smooth as expected, due to the uneven surface from the prior KOH etching at 70°C.
- Results: During the etching, the wafer broke into eight chips, along the alignment lines between each chip. However, five chips survived the KOH etch, and were used for device testing.

4.3.3 Nitride etch and Al deposition

Before the aluminum deposition, the nitride layer was etched with Mask#3 (the mirror and spring mask). This creates some step edges for alignment of Mask#2 (the aluminum metal mask). Figure 4.19 shows the results after aluminum deposition.

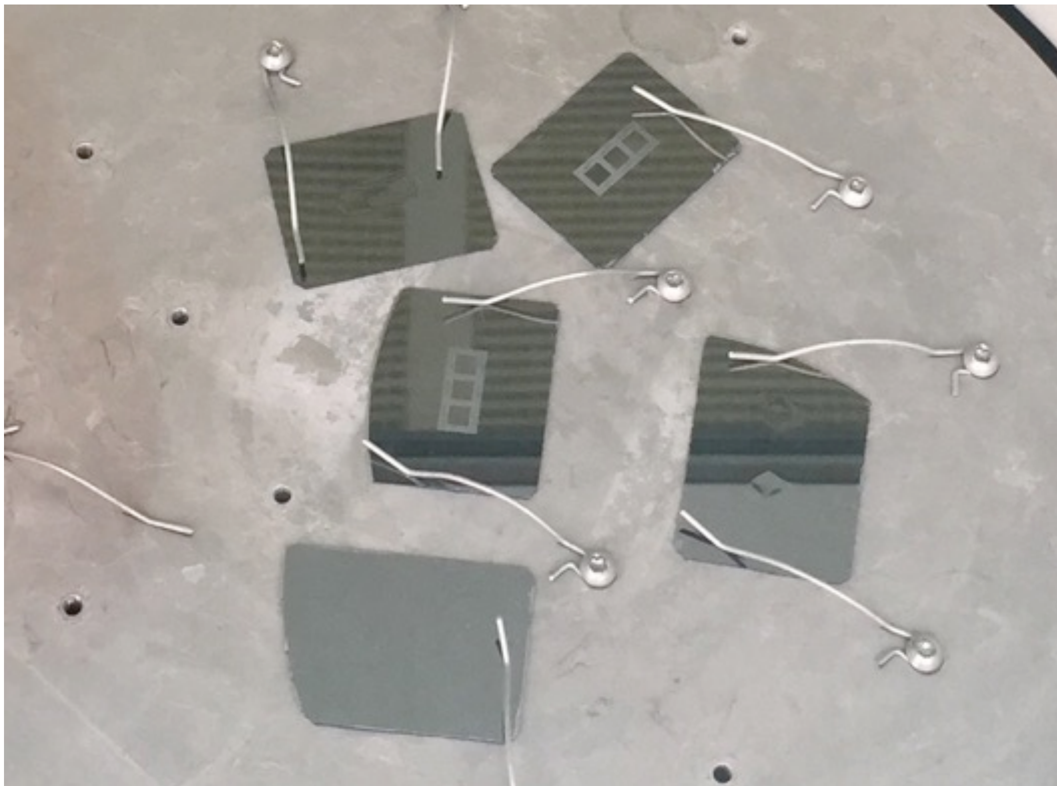

Figure 4.19: Samples with Al deposited on the frontside.

Process:

- Two-sided lithography was done with the back etch mask. Photoresist was spun at 3000 rpm. Hardbake at 120°C for 20 minutes.
- IR source and backside alignment wafer holder were used in the two-sided ABM mask aligner.
- Nitride was etched in the plasma etcher. This nitride etch created topographical steps to faciliate the alignment of the aluminum wires and mirror reflector mask in the next lithography.
- After nitride etch, the etched surface showed different smoothness. Under the same condition, some samples had smooth silicon surface, while others were rough. The roughness wouldn't affect the quality of micromirrors, because these areas would be punched through later.
- An 802 nm aluminum film was deposited with the dual source thermal evaporator. Both sources were used. About 130 cm of Al wires were used. The cooling water for the bell jar was turned on. Pressure was 2.1×10^{-7} Torr. Melting current was 15 A, and deposition current was 20-22 A. Deposition rate was 17 Å/s.

4.3.4 Lithography and Al etch

Aluminum wet etch was done to pattern the wires, soldering pads, and the mirror reflecting surface. Bubbles generated during Al etch caused some problems.

Process

- Lithography was done with Al etch mask. Photoresist was spun at 3000 rpm. No hardbake was done.
- Wet etching: Al etchant was heated to 50°C, and the aluminum etch step required was 100 seconds. The magnetic stirrer was turned on. Etch rate was 530 nm/min.

- After 100s etching, there were some round aluminum spots left on the sample. This is mainly caused by the bubbles during the etching. In order to make bubbles leave the sample surface faster, the sample should be stirred by hand occasionally.
- Another 30 second aluminum etch was done. The solution was stirred by hand, while the magnetic stirrer was spinning. This helped bubbles leaving the sample faster. All the aluminum spots were etched.
- Results: The smallest wire width was successfully patterned. The undercut during the aluminum etch was less than 2 μm, and could be ignored.

4.3.5 Micromirror release

The Trion plasma etcher was used to release the micromirrors. Wafer was etched about 15 μm from the frontside with patterned photoresist as a mask. Then, it was etched from the backside to release the mirrors without mask. Figure 4.20 shows the results of the released pop-up mirrors.

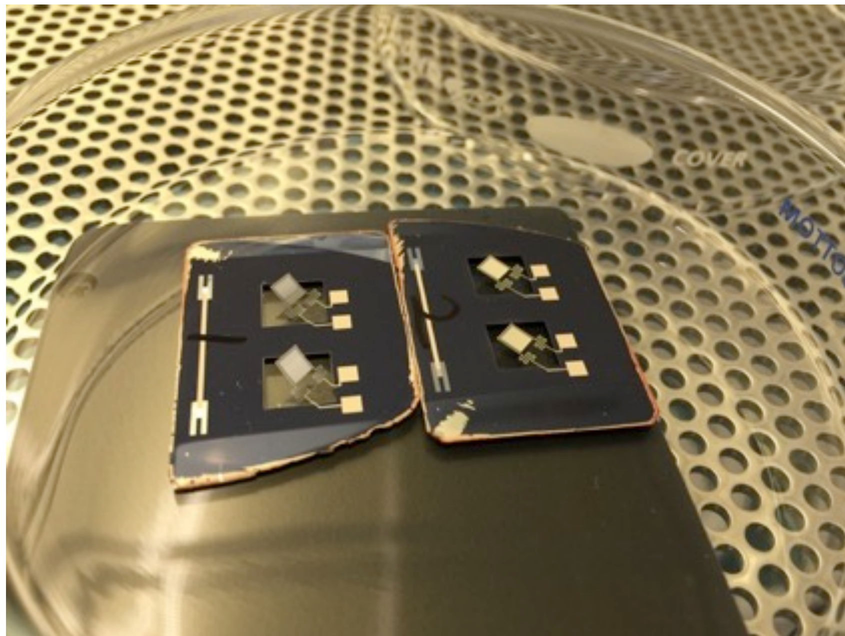

Figure 4.20: Released pop-up micromirrors.

Process

- Lithography was done with front etch mask. Photoresist was spun at 3000 rpm. Hardbake at 120°C for 20 minutes.
- Plasma etching was done on both sides of the sample. The sample was first etched about 15 µm from the frontside, with a photoresist mask. Then, it was etched from the backside to thin the membrane, and release the mirror. Each etching has two steps: native oxide etching, and silicon etching.
- Native oxide etch recipe: Pressure 50 mT, CF_4 at 45 sccm, O_2 0 sccm. ICP power at 300 W, RIE 25 W. Etch time 15 seconds.
- Silicon etch recipe: Pressure 50 mT, SF_6 at 30 sccm. ICP power 300 W, RIE 50 W. Etch rate 1.6-1.8 µm/min. A plasma color change was seen during this process.
- Results: After releasing from backside, the pop-up mirrors on chip #1 lifted up at 29.3°, and chip #2 at 6.0°. The lifted micromirror is caused the high stress silicon nitride layer. The difference in the angles is probably caused by different spring constants for each device. This is due to the different etch rates of the silicon when the sample is placed at different positions in the chamber, giving different amount of undercut, and so slightly different spring dimensions.
- The resistance of each micromirror was measured after releasing. The resistance R_{coil} is 15-20 Ω for the pop-up micromirrors, and 35-40 Ω for the rotating micromirrors. The variation in resistance comes from the difference in the parameter l of each micromirror spring.

4.4 Conclusions

A successful fabrication process was developed for both rotating and pop-up silicon membranes and micro-mirrors. This was the first process in our laboratory that utilized a

thinned silicon membrane as the starting platform for the MEMS device, enabling lower cost fabrication than if SOI wafers were used.

The fabricated mirrors showed some visible bending due to the high stress silicon nitride masking layer. This can be seen in the initial lifting angle of the pop-up mirrors, and in the slight curvature of membrane itself. This can be reduced by thinning this layer prior to metal deposition on the membrane.

Chapter 5: Chip Testing of Micromirrors

This chapter discusses measurements of the performance of the rotating and pop-up micromirrors. Two testing methods were used. Microscope measurements were used when DC current (and so displacement) was applied to the micromirror. This method was used in the deflection angle measurement (DC mode) and for evaluating the curvature of micromirrors. Dynamic motion measurement using a laser-based system was used when an AC current was applied. This method was used in the measurement of resonance frequency, Q-factor, deflection angle (AC actuation), and air damping.

This chapter starts with an introduction to the testing environment and circuit setup (Section 5.1). Then, both microscope and laser measurements were used for rotating micromirrors (Section 5.2). However, due to the limitation of laser measurement system, the pop-up micromirrors were only tested in DC mode (Section 5.3).

5.1 Testing environment and circuit setup

The actuation circuit for the micromirrors is illustrated in Figure 5.1. In this circuit, the rotating micromirror was connected to the source, a protection resistor, and an ammeter.

The source provides reliable DC or AC voltage to drive the circuit. In DC mode, a dual source DC power supply (Agilent E3647A) is used to generate up to 60 V. In AC mode, a function generator (Agilent 33120A) provides a triangular wave. A protection resister of $R_{protection}$ 1 kΩ is connected in series to prevent the mirror from over heating. An ammeter

(Agilent 34461A) measures the current flowing through the Lorentz coil on the micromirror, as the deflection angle is measured.

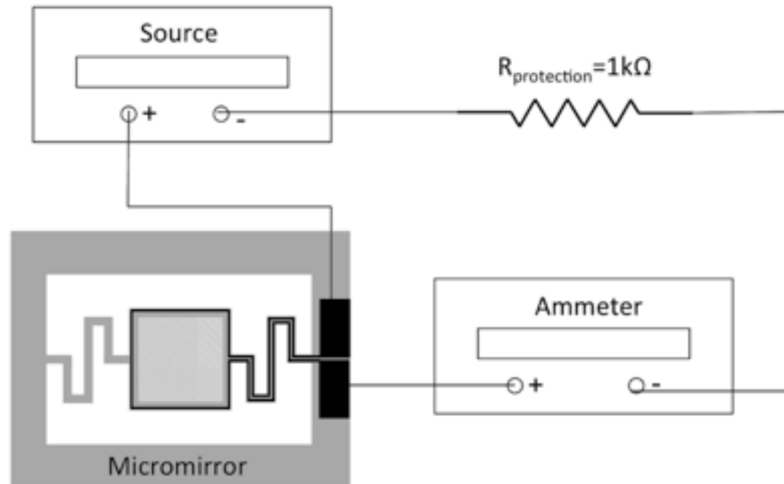

Figure 5.1: Actuation circuit of micromirror.

The rotating micromirror chip is connected to the actuation circuit with silver conductive epoxy (H20E Epo-Tek). Figure 5.2 illustrates the mounting techniques for the micromirror chip. A permanent magnet is used to provide magnetic field around the micromirror chip. Two microscope slides are fixed between the magnet and the micromirror chip as a 1 mm spacer. This provides more space between the micromirror and magnet, and helps prevent micromirror from damages during the actuation. Adhesive strips were used to firmly attach the micromirror chip with glass spacer and the magnet.

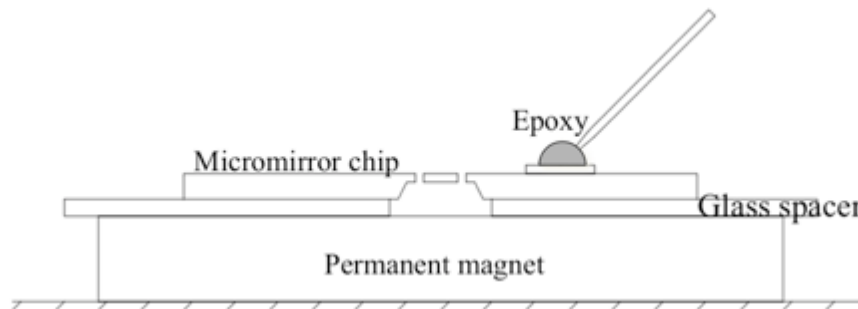

Figure 5.2: Micromirror mounting.

The magnet field of the magnet is 0.4 T measured at the micromirror with a gaussmeter (AlphaLab GM1-ST). According to the NCEI database, the earth's magnetic field is 57 μT in Winnipeg [14]. Compared with the magnetic field around the magnet, the effect of earth magnetic field is negligible.

5.2 Testing of rotating micromirrors

5.2.1 Microscope measurement for rotating micromirrors

In this method, an Olympus SZX12 microscope is used to measure the displacement of micromirror. This method is accurate, reliable, and easy to align. However, it is not suitable for angles smaller than ~0.2° for rotation, due to the limit of depth of focus of the microscope objective used (100x). The resolution of measured height difference in Δh (Figure 5.3) with this objective was 5 μm.

Motion is measured by adjusting the position of the sample stage of the microscope, to re-focus the sample image as the mirror displaces. The microscope is first focused on one position of the object, writing down the reading on the fine focus knob n_0. Then, the microscope focuses on to another spot, moving only the fine focus knob to n. When adjusting the focus of microscope, the height of the sample stage was moving by the same distance Δh, bringing the second spot into focus. The distance of stage movement Δh is calculated according to Equation 5.1, since each graduation line on the fine focus knob represents 15 μm for Olympus SZX12.

$$\Delta h = 15\left(n_0 - n\right)\mu m \tag{5.1}$$

This method can be used to measure the difference in height on different spots of the micromirror, such as due to surface curvature. It can also be used to measure the height difference of the same spot before and after actuation.

Before each measurement, the heights of chip corners were measured to determine the tilting angle of the sample stage.

As shown in Figure 5.3, the deflection angle of the rotating micromirror is calculated as:

$$\sin\theta = \frac{\Delta h}{1.5mm} \tag{5.2}$$

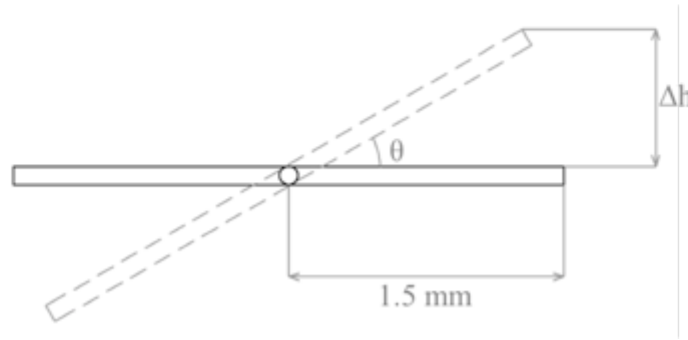

Figure 5.3: Deflection angle measurement for rotating micromirror.

The accuracy of the microscope approach is calculated, based on ±5 μm error in the focus adjustment and reading of graduation lines. For the rotating micromirrors (1.5 mm length), the accuracy is calculated from Equation 5.2:

$$d\theta = \frac{1}{1.5mm}\frac{1}{\sqrt{1-\left(\frac{\Delta h}{1.5mm}\right)^2}}d\Delta h \approx \frac{1}{1.5mm}d\Delta h = 0.19° \tag{5.3}$$

where $d\Delta h$ is 5 μm, and given that Δh / 1.5 mm is much less than 1.

Measurement of deflection angle of rotating mirrors with DC current

The performance of the rotating mirrors was measured by applying a DC current to the Lorentz coil to actuate the micromirrors. Two rotating micromirrors were measured: micromirror with $Spring_{section\ length}$ = 2 mm (mirror #1), and $Spring_{section\ length}$ = 1.5 mm (mirror

#2). The micromirror with $Spring_{section\ length}$ = 2.5 mm was damaged, and thus not tested. Mirror displacements were measured on the four corners of each micromirror. The average displacement is applied as *Δh* in Equation 5.2 to calculate the deflection angle. Measurements were taken for currents ranging from 0 to 60 mA, with a step of 5 mA.

For mirror #1, Figure 5.4 compares the measured deflection angle with those of the COMSOL simulation. From this figure, we can see that mirror #1 has a linear rotation vs. current as expected. This shows that the S-shape torsion springs attached to the micromirrors are moving in a linear elastic regime.

Plotted in Figure 5.4 are COMSOL simulations for S-shape torsion springs of 12 μm and 11 μm thickness. Since the plasma etched sidewall of micromirrors is visible due to its slope (~60°), the thickness of the micromirror can be measured with the microscope. The thickness was measured to be ~11±1 μm for both mirrors #1 and #2. Accordingly, measured performance is in agreement with the simulated performance, within the margin of the micromirror thickness. This agreement proves that the COMSOL simulation is correct.

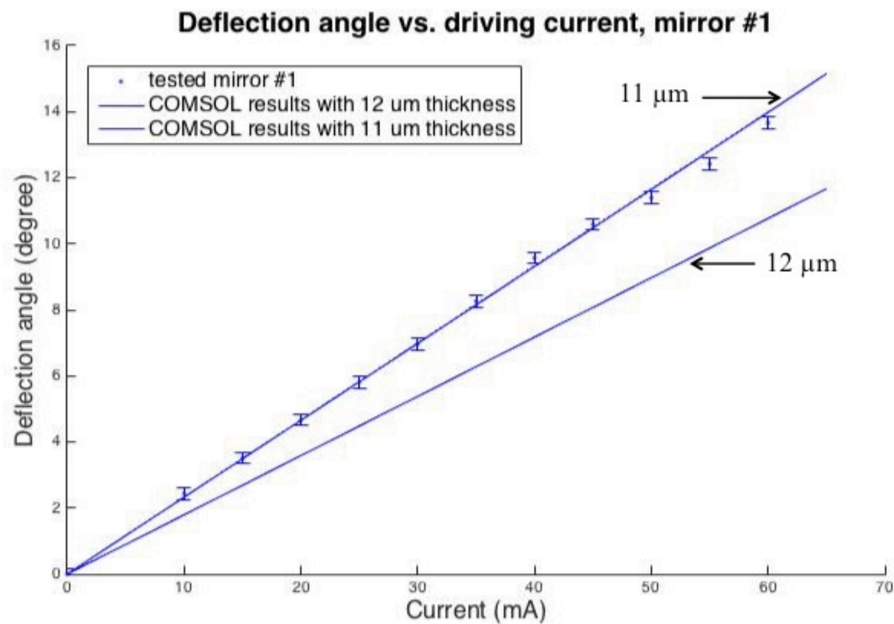

Figure 5.4: Deflection angle vs. driving current for mirror #1.

According to Hook's law, the parameter spring constant κ characterizes the stiffness of a spring in its linear range. A torsion spring follows the angular form of Hook's law, which is given by:

$$\sin\theta = \frac{\Delta h}{1.5mm} \tag{5.4}$$

where τ is the torque applied on the spring, and θ is the deflection angle. For the micromirror tested in this measurement, torque is the cross product of level arm r with Lorentz force F:

$$\vec{\tau} = \vec{r} \times \vec{F} \tag{5.5}$$

The Lorentz force is generated on one edge of the micromirror is calculated to be:

$$\vec{F} = I\vec{l} \times \vec{B} \tag{5.6}$$

Lorentz force is generated on opposing sides of the micromirror, and two S-shape springs are connected to the micromirror. Thus, from the equations above, the spring constant κ of the S-shape springs is given by:

$$\kappa = \frac{\tau}{\theta} = r\frac{F}{\theta} = rlB\frac{I}{\theta} \tag{5.7}$$

where $\frac{\theta}{I}$ is the slope of the testing curve in Figure 5.4. For rotating micromirrors, level arm is half of micromirror length, $r = \frac{l}{2} = 1.5mm$. From Equation 5.7, the spring constant of mirror #1 is calculated to be 0.88 μNm/rad.

The deflection angles for mirror #2 are illustrated in Figure 5.5, which compares well with the COMSOL simulation results. As shown in the figure, the S-shape torsion springs in mirror #2 are also in their linear range. The spring constant of mirror #2 is calculated from Equation 5.7 to be 1.4 μNm/rad.

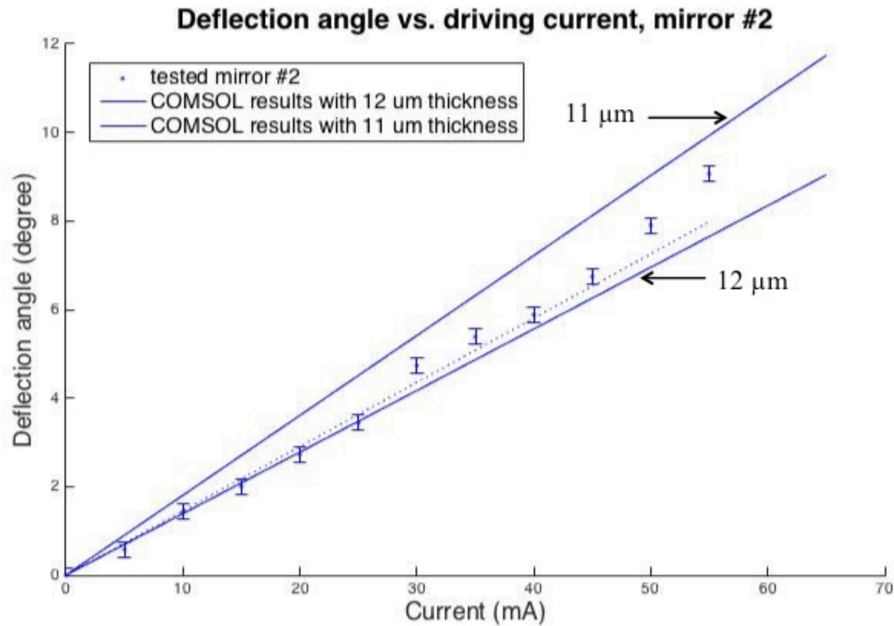

Figure 5.5: Deflection angle vs. driving current for mirror #2.

Measurement of rotating micromirror curvature

As discussed in Section 4.4, the curvature of the silicon membrane was observed after aluminum deposition and also observed after micromirror release. The curvature is an important parameter of a micromirror. The curvature can affect the divergence of the light beam. It also affects the distance that light can travel without decollimation.

The curvature of the rotating micomirrors was measured with an Olympus BX51 microscope, using a 50x objective, which has below 1 μm depth of focus. This microscope has a finer focus adjustment for the sample stage, with each graduation line on the fine focus knob representing 1 μm. As shown in Figure 5.6, relative heights were measured at seven positions on the rotating micromirror #1. The curvature was calculated from the relative height of the seven points. In the x-axis, the radius of curvature is -3.1 cm in the center. In the y-axis, the radius of curvature is 5.8 cm on the left and 8.6 cm on the right.

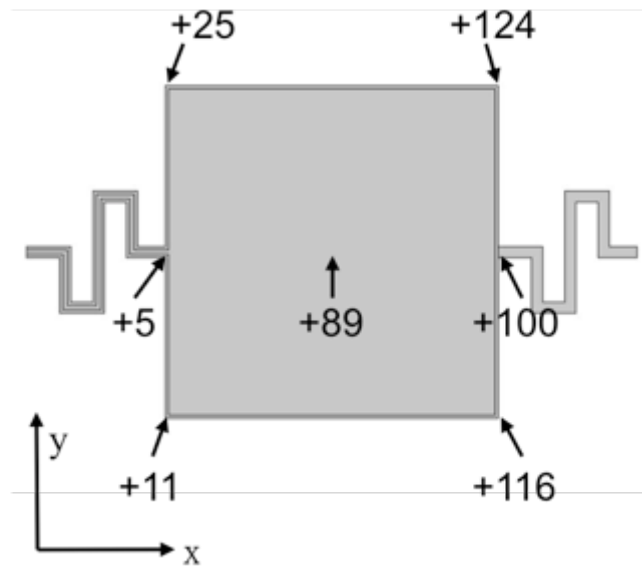

Figure 5.6: Curvature measurements for mirror #1 (units are in micrometers).

The same measurements and calculation were done on mirror #2 (as shown in Figure 5.7). The radius of curvature is calculated to be 8.0 cm along the x-axis, and 6.6 cm (left) and 6.8 cm (right) along the y-axis.

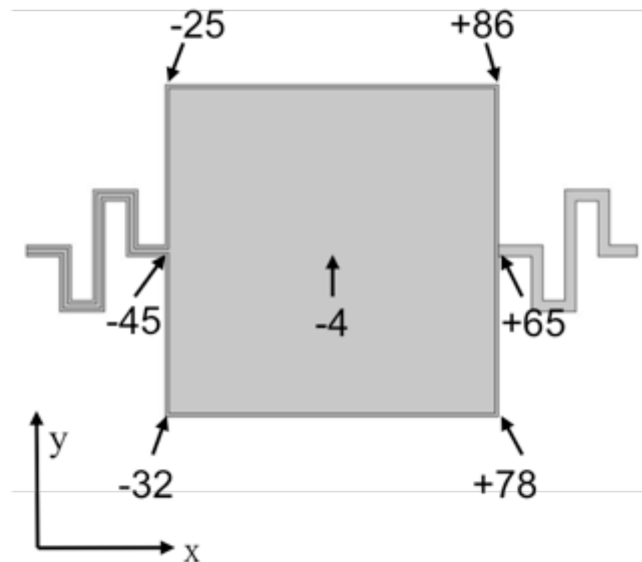

Figure 5.7: Curvature measurements for mirror #2 (units are in micrometers).

5.2.2 Dynamic motion measurements for rotating micromirrors

The dynamic motion measurement is adopted to measure the deflection angle of the rotating micromirrors in AC mode.

The rotating micromirror is connected to the same magnet and actuation circuit, as shown in Figure 5.1 and Figure 5.2. In order to measure the deflection angle, a laser beam shines onto the center of micromirror at a 30° angle, as illustrated in Figure 5.8. The laser beam is reflected to a vertically placed graph paper with 1 mm graduations. The laser spot on the graph paper moves up and down while the mirror's deflection angle changes during AC actuation. The biggest deflection angle is calculated with the maximum height of the laser spot, *h*.

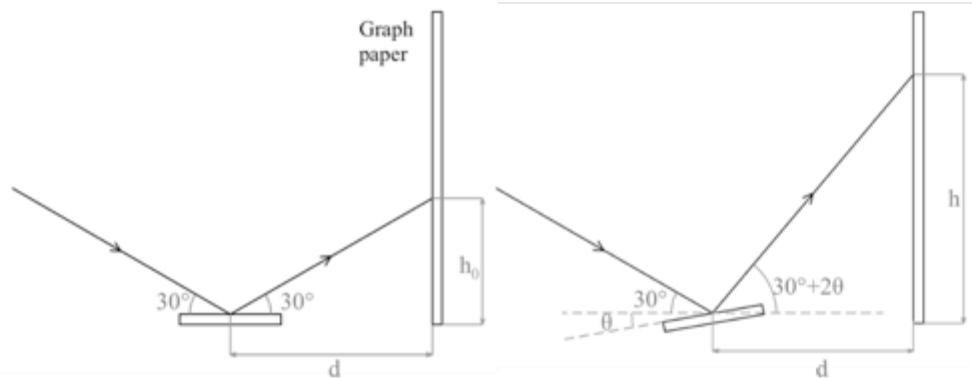

Figure 5.8: Rotating micromirror measurement before (left) and after (right) actuation.

Before each measurement, the spacing *d* needs to be calibrated. The spacing *d* is calculated with the initial position of the laser spot h_0, when the driving current is 0 mV.

$$d = \frac{h_0}{\tan 30°} \tag{5.8}$$

Since the angle of reflected light is 30° + 2θ, the deflection angle θ can be calculated with the maximum height of laser spot, and is given by:

$$\tan(30° + 2\theta) = \frac{h}{d} \tag{5.9}$$

The accuracy of the dynamic motion measurement can be calculated based on ±0.2 mm error in the reading of 1 mm graph paper. For rotating micromirrors, the accuracy is calculated from Equation 5.10:

$$d\theta = \frac{1}{2d}\frac{1}{1+\left(\frac{h}{d}\right)^2}dh = \frac{1}{2d}\frac{1}{1+\tan^2\left(30^\circ+2\theta\right)}dh$$
$$= \frac{1}{2d}\cos^2\left(30^\circ+2\theta\right)dh < 0.1^\circ \tag{5.10}$$

Resonance frequency and Q-factor of rotating micromirror

To better characterize the rotating micromirrors, resonance frequency and Q-factor were measured and discussed.

Resonance frequencies are the frequencies at which the response magnitudes are relatively maximum. The resonance frequency was measured with the dynamic motion measurement. To measure the resonance frequency, an AC current was applied to the Lorentz coil on the micromirror. The peak amplitude of the AC current was constant at 7 mA_{peak}, while the frequency of swept from 40 Hz to 500Hz. Resonance frequency is the frequency at which the micromirror has biggest angle of rotation. The resonance frequency was found to be 364 Hz for mirror #1 (see Figure 5.9), and 406 Hz for mirror #2.

Q-factor is a parameter that describes the damping effect of a resonator. It is the ratio of resonance frequency to half-power bandwidth, which is given by Equation 5.11:

$$Q = \frac{f_r}{\Delta f} \tag{5.11}$$

Figure 5.9 illustrates the angle of rotation at different frequencies for mirror #1. From Equation 2.11, the Q-factor is calculated to be 20.

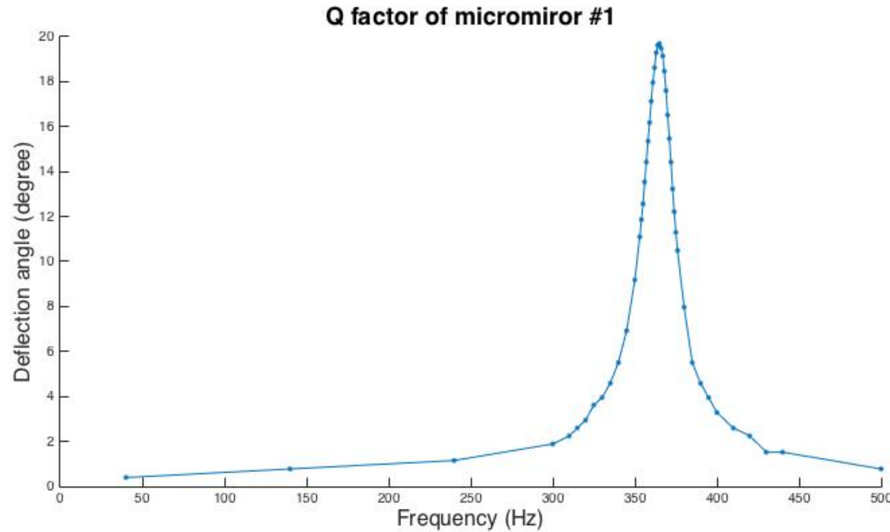

Figure 5.9: Deflection angle vs. frequency for mirror #1.

Measurement of deflection angle with AC current and air damping

When in motion, the micromirror is pushing air. This causes air damping, which dissipates energy and affects the linearity of the micromirror. The air damping effect increases with the size of the micromirror, and its velocity of movement.

Air damping of the micromirror was not measured directly. Instead, the angle of rotation in AC mode was measured to observe the non-linearity of micromirror, which gives an indication of the air damping effect. Linearity of micromirror is measured by an dynamic approach. An AC current was applied to the Lorentz coil on the mirror #1. The frequency of the AC current was the resonance frequency of the micromirror, while the peak amplitude swept from 50 mV to 750 mV with a step of 10 mV. The total resistance of the circuit is 88 Ω. The angle of rotation is calculated at each AC current.

Figure 5.10 plots the deflection angle vs. amplitude of AC current applied to the Lorentz coil. From this figure, it can be observed that the micromirror motion becomes non-linear after ~ 4° of motion. It can be concluded that the non-linearity results from the air

damping effect, since the springs were earlier tested to be linear up to 14° (as discussed in the DC mode measurements Section 5.2.1.1).

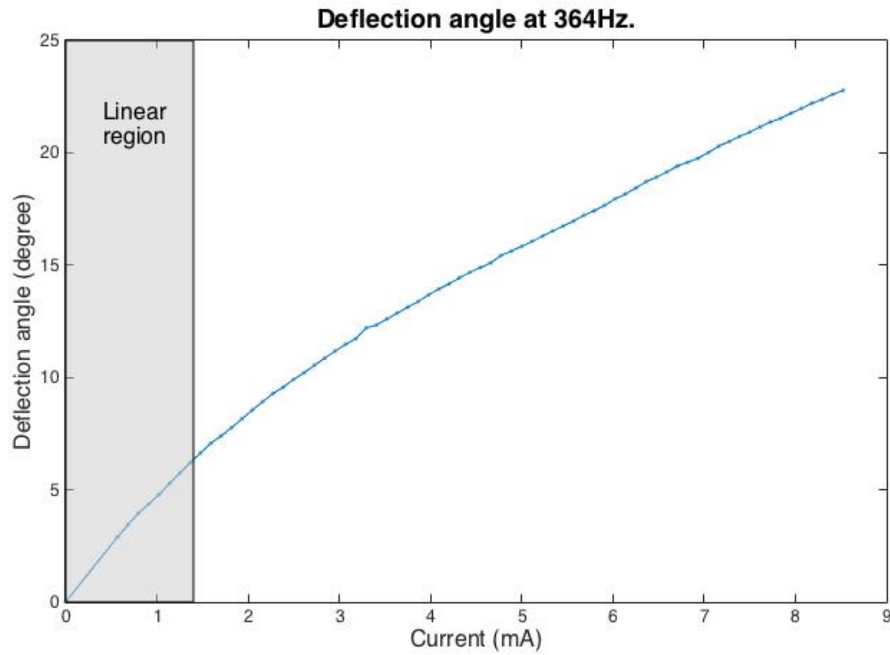

Figure 5.10: Deflection angle vs. driving current (at resonance) for mirror #1.

5.3 Testing of pop-up micromirrors

5.3.1 Microscope measurement

For the pop-up micromirrors, the measurement method follows the same steps as for the rotating micromirrors. Figure 5.11 illustrates the relationship between height difference Δh and angle of rotation θ for pop-up micromirrors. The deflection angle for pop-up micromirror is given by:

$$\sin\theta = \frac{\Delta h}{3mm} \tag{5.12}$$

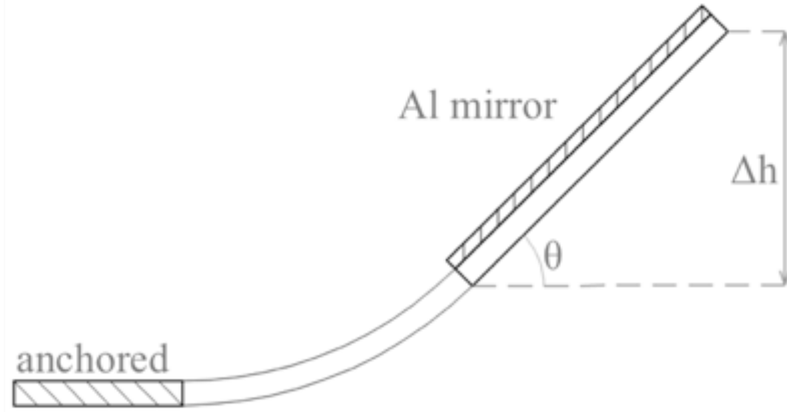

Figure 5.11: Deflection angle for pop-up micromirror.

For pop-up micromirrors (length 3 mm), the accuracy of the microscope measurement is also based on ±5 µm error in the focus adjustment and reading of graduation lines. The measurement accuracy can be calculated from Equation 5.3:

$$d\theta = \frac{1}{3mm}\frac{1}{\sqrt{1-\left(\frac{\Delta h}{3mm}\right)^2}}d\Delta h \approx \frac{1}{3mm}d\Delta h = 0.10° \tag{5.13}$$

where $d\Delta h$ is 5 µm, and given that Δh / 3 mm is much less than 1.

Measurement of angle of lift in DC mode

Two pop-up micromirrors were measured: mirror #3 possessing a 1.5 mm spring segment length, and mirror #4 with a 2 mm spring segment length. The pop-up micromirrors were made in different batches, and thus come in different thickness. Mirror #3 had a $Membrane_{thickness}$ = 9±1 µm, and Mirror #4 had a $Membrane_{thickness}$ = 15±1 µm. As mentioned in Section 4.3.5, both pop-up micromirrors had an initial tilting angle, which was introduced by the high stress silicon nitride layer. The initial tilt angle θ_0 was 29.2° for mirror #3, and 5.7° for mirror #4. This value should be noted when comparing measurements of mirror lift

angle during actuation, with the COMSOL simulation results, as the initial angle should be subtracted from the measured angle during deflection measurements.

Figure 5.12(a) compares the angles of lift from COMSOL simulation (9 µm thick mirror), with results from the measurement for mirror#3. We can see that the mirror motion appears non-linear with increasing driving current. However, this is due to the changing magnetic field during mirror lift, which occurs because the Lorentz force coupling increases with mirror lift angle. To better illustrate for this, Figure 5.12(b) plots the motion of the mirror as a function of Lorentz force. We can still, however, see a disagreement between simulation and measurement at large angles of lift. It is concluded that this difference is due to the spring becoming non-linear at large angles of lift.

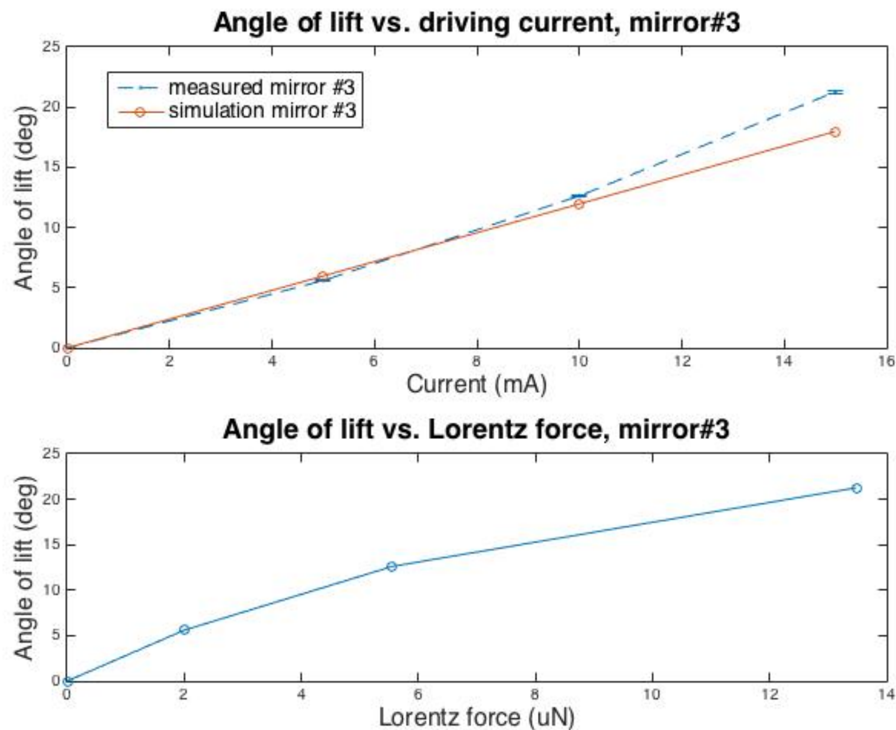

Figure 5.12: (a) Angle of lift vs. driving current for mirror #3 (upper). (b) Angle of lift vs. Lorentz force (lower).

Similar to the rotating micromirrors, the S-shape springs in the pop-up micromirror also follows the same equations. As discussed in Section 5.2.1.1, the spring constant κ of the torsion springs is given by:

$$\kappa = \frac{\tau}{\theta} = r\frac{F}{\theta} = rlB\frac{I}{\theta} \tag{5.7}$$

where r = 6 mm, and $\frac{\theta}{F}$ is the slope of the testing curve in Figure 5.12(b). For pop-up micromirrors, level arm r is the distance from the anchored point to the further edge of the micromirror, 6.25 mm. From Equation 5.7, the spring constant of mirror #3 is calculated to be 0.15 µNm/rad (calculated from 10 mA driving current data point).

Figure 5.13 compares the angle of lift from COMSOL simulation (15 µm thick mirror), with the measurement for mirror#4. The spring constant of mirror #4 was calculated to be 0.94 µNm/rad (calculated from 10 mA driving current data point).

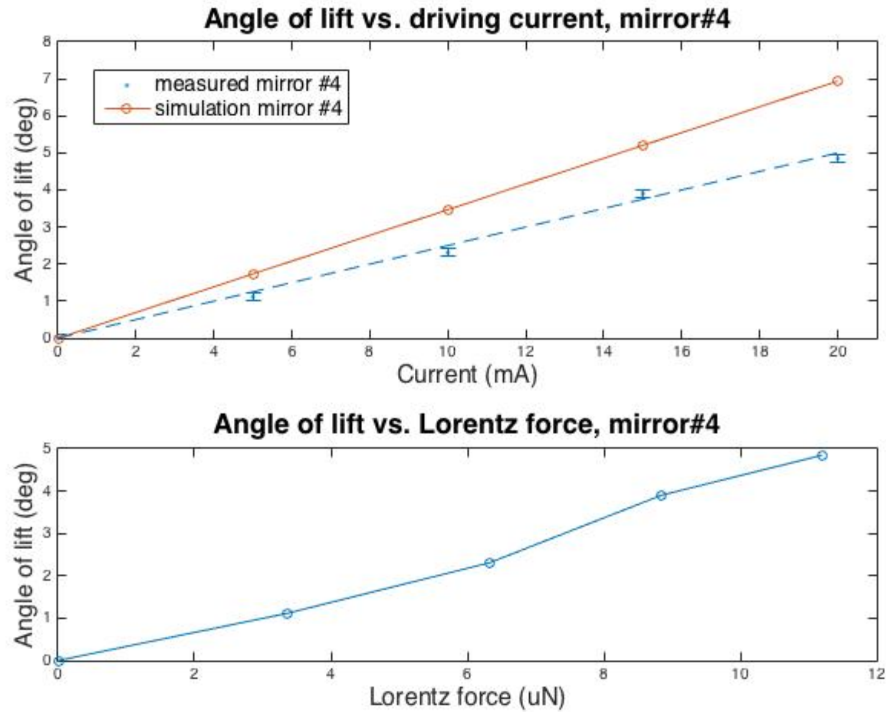

Figure 5.13: (a) Angle of lift vs. driving current for mirror #4 (upper). (b) Angle of lift vs. Lorentz force (lower).

Curvature of the pop-up micromirrors

Curvature of micromirror was also observed in pop-up micromirrors. The curvature of the pop-up micromirrors was measured with the Olympus BX51 microscope. During the measurement, the micromirror was not actuated. As shown in Figure 5.14, relative heights were measured at nine positions on the pop-up mirror #4. All the measured heights were in micrometer. In the x-axis, the radius of curvature is 4.5 cm at the top edge of the mirror, and 11.3 cm at its bottom. In the y-axis, the radius of curvature is 7.8 cm in the center, and -20 cm on both edges.

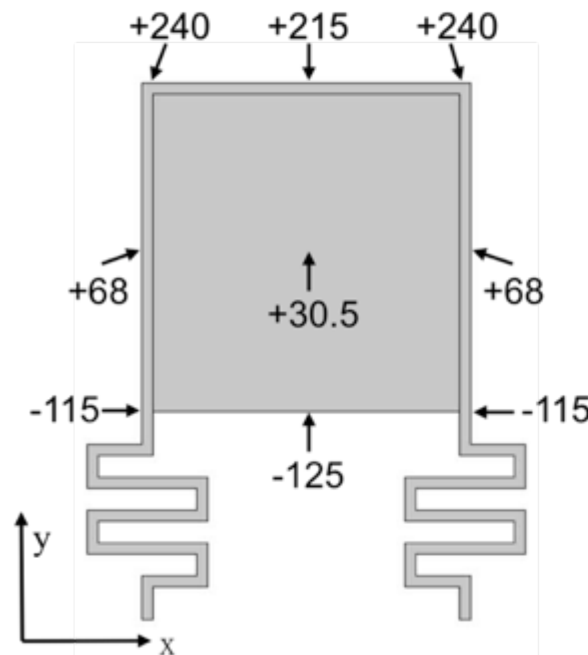

Figure 5.14: Curvature measurements for mirror #4 (units in micrometers).

5.3.2 Limitations of dynamic motion measurement

Measurement of dynamic motion for the pop-up mirror could not be done, because unlike the rotating mirrors, the center of the pop-up mirrors raise as they are actuated. This changes the height *hm* as shown in Figure 5.15. At the same time, the lifting of the

micromirror also shifts the reflection position on the micromirror, which makes it difficult to compare the position of the laser spot on the graph paper used to measure the laser position.

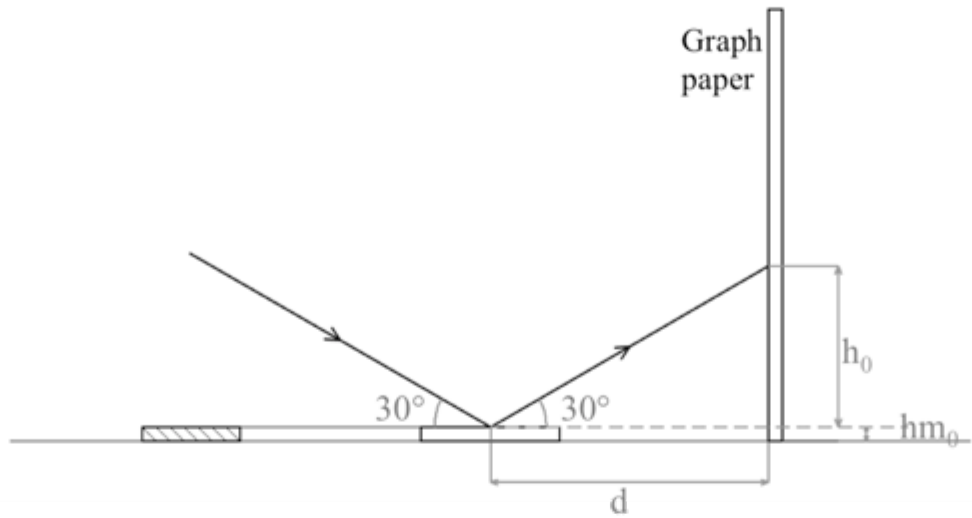

(a)

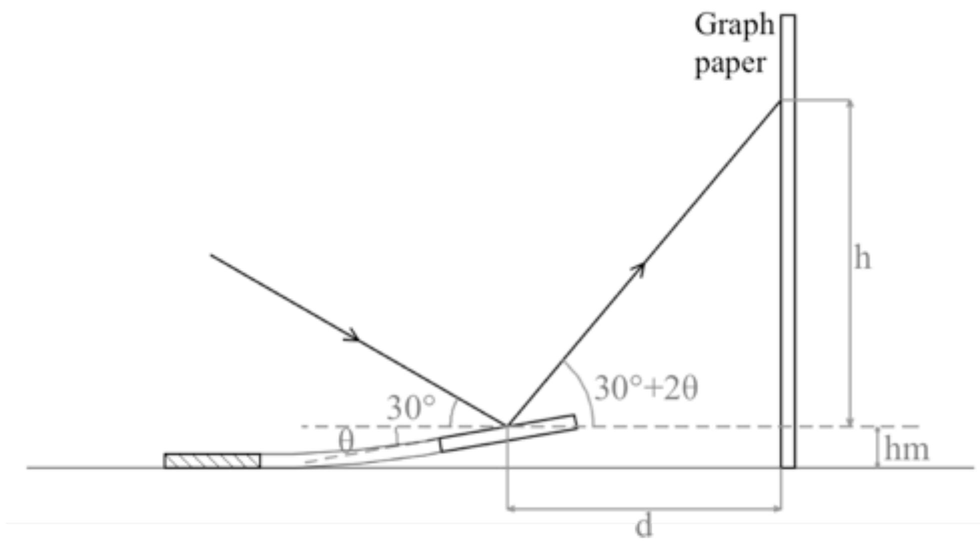

(b)

Figure 5.15: Pop-up micromirror measurements before (a) and after (b) actuation.

5.4 Summary

Rotating and pop-up micromirrors were successfully fabricated and tested. They showed good match between the predicted spring constant κ calculated from COMSOL simulations and the experimentally measured results, giving confidence to the COMSOL design study. Some of the key parameters of the tested micromirrors are listed in Table 5.1.

Table 5.1: Summary of micromirrors.

	Rotating		**Pop-up**	
	Mirror #1	**Mirror #2**	**Mirror #3**	**Mirror #4**
$Spring_{segment\ length}$	2 mm	1.5 mm	1.5 mm	2 mm
$Membrane_{thickness}$	11±1 μm	11±1 μm	9±1 μm	15±1 μm
κ COMSOL	0.81 μN/rad	1.1 μN/rad	0.35 μN/rad	1.2 μN/rad
κ tested	0.88 μN/rad	1.4 μN/rad	0.15 μN/rad	0.94 μN/rad

Chapter 6: Magnetic field sensor

This chapter discusses a magnetic field sensor built with the rotating micromirror. A brief literature review on MEMS magnetic field sensors first presented, followed by a discussion of the developed magnetic field sensor of this thesis. The working principles, measurement set-up and experimental results are presented. This work has been published in journal paper [1].

6.1 Introduction to Lorentz force based magnetic field sensors

Traditionally, the magnetic field is measured with an inductive pickup coil. Hall effect sensor is one of the most common solid-state magnetic field sensors, whose sensitivity is usually lower than 50 mV/mT [15]. Magneto-optical Kerr effect is also studied for magnetometers. Steven A. Oliver et al demonstrated a Kerr effect sensor with magnetic field sensitivity of 4×10^{-3} Oe [16]. Superconducting quantum interference device (SQUID) sensor is mainly used in laboratories, due to its low working temperature and noise sensitivity. It exhibits highest sensitivity (femto-Tesla) among all the sensing techniques [17].

Much research has been focused on resonance based MEMS magnetic field sensors in the recent years. Lorentz force is generally used in these types of sensors. Resonance based MEMS magnetic field sensors have many benefits compared with other types of sensors. They have higher sensitivity than Hall effect sensors, and lower environmental requirements as well as lower cost than SQUID sensors.

In a resonance based MEMS magnetic field sensor, an AC current flows across the resonator, generating periodic Lorentz force at the mechanical frequency of the resonator itself, which can greatly augment the mirror motion, as illustrated in Figure 6.1. The AC current also causes a periodic motion of the structure, which allows for filtering of signal noise outside of the resonance frequency, thus, enhancing resolution. In a magnetic field, Lorentz force $\vec{F}$ on a current-carrying wire follows equation 2.4, with the motion of the structure proportional to the magnetic field strength. With MEMS techniques, the magnetic field sensor can be made in a compact size. At different level of current, resonance MEMS Lorentz magnetic field sensors can work in a wide range of measurement.

$$\vec{F} = I\vec{\ell} \times \vec{B} \tag{2.4}$$

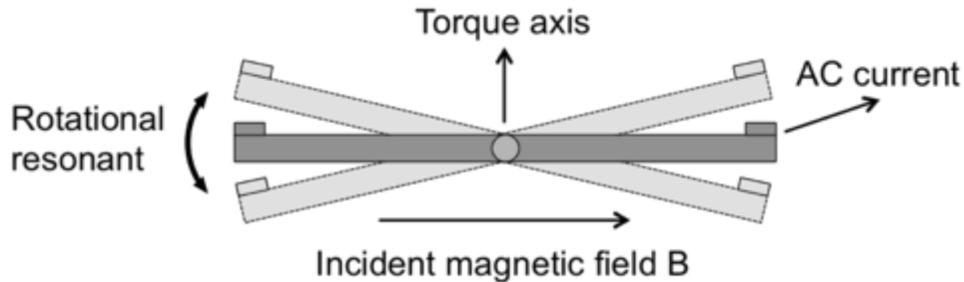

Figure 6.1: Lorentz force resonator in a magnetic field.

The magnetic field strength can be calculated from the motion measurement results. There are several different sensing methods for the mechanical deflection of a resonant structure. Capacitive sensing transforms the mechanical deflection into the change in capacitance. Piezoresistive sensing transforms deflection into change in resistance. Optical sensing adds a laser light path to the system. A common method is to have the deflection of the moving mirror change the location of the reflected laser spot on a photodetector. These methods are discussed below.

6.1.1 Capacitive sensing of sensor membrane position

A capacitor is an electronic component that stores energy by collecting charges on the conductor plates. When the distance changes between two parallel plates, the capacitance will change accordingly. The initial capacitance of a parallel capacitor, if neglecting fringing effects, is given by the equation:

$$C_0 = \frac{\varepsilon A}{d} \tag{6.1}$$

When the distance d between the parallel plate is changed to d', the capacitance will be given by:

$$C' = \frac{\varepsilon A}{d'} = C_0 \frac{d}{d'} \tag{6.2}$$

A 3D micromechanical compass was designed and fabricated by Kyynäräinen et al. [18]. Figure 6.2 illustrates the principles of torsional magnetometer. The sensitivity of this sensor reaches 60 nT at 0.1 mA. The sensor was built by bonding resonator wafer with bottom electrode wafer. The fabrication started by RIE to pattern the cavity for electrodes on both wafers. A layer of thermal oxide was grown on the bottom wafer for electrical insulation. The electrodes were made by deposition and patterning Mo/Al layer. Two wafers were bonded at 200 °C, with electrodes facing each other. The bottom silicon layer of the SOI wafer was removed in RIE, exposing the buried oxide layer, which works as the insulation layer between coil and top electrodes. The coil and electrical bridge formed by depositing and patterning of the Mo and Al layers. Finally, the resonator was released by DRIE.

Kádár et al. [19] presented a similar resonant magnetic field sensor, with high quality factor and detection limit of 1 nT. Li et al. [20] also reported a 3D micromechanical compass using capacitive sensing, with sub-30 nT/√Hz resolution.

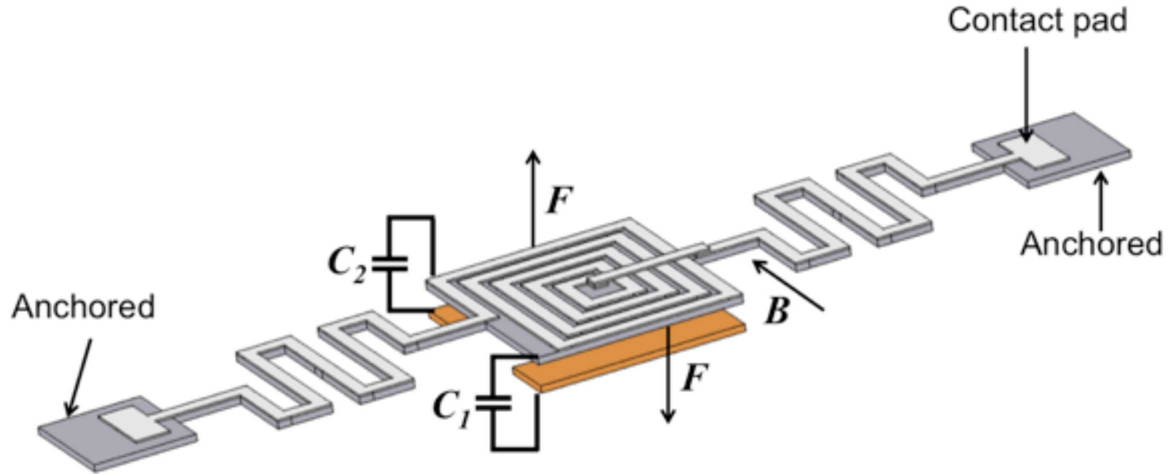

Figure 6.2: Schematic diagram of magnetic field sensor with capacitive sensing.

6.1.2 Piezoresistive sensing of sensor membrane position

Piezoresistive effect describes the change in resistance when the material is under mechanical strain. For piezoresistive materials, the change in resistance follows the equation, given by:

$$\frac{\Delta R}{R} = G\varepsilon \tag{6.3}$$

where G is the gauge factor, and ε is the mechanical strain. Doped silicon is an ideal piezoresistive material, for its high piezoresistive effect, and IC compatibility.

For piezoresistive sensors, a piece of piezoresistive material is deposited on the cantilever that suspends the micromirror. When the micromirror is mechanically vibrating at resonance frequency, the piezoresistive material will be under periodic mechanical strains. Thus, the resistivity of the piezoresistive material will be alternating at the same frequency.

Herrera-May et al. [21] proposed a resonance based magnetic field sensor that adopts piezoresistive sensing. Figure 6.3 illustrates the schematic diagram of the magnetic field sensor with piezoresistive sensing, and the associated Wheatstone bridge that measures the change in resistance. The sensitivity reaches 143 nT at 22 mA. The 1400 µm × 2800 µm× 12

μm (L×W×H) micromirror was fabricated on n-type SOI wafers. Fabrication started by growing an 18 nm thermal oxide layer and depositing a 118 nm silicon nitride layer. The nitride was removed on the front side, and patterned on the backside for backetch. To form the p-type piezoresistors, boron was implanted on the front side, using a second mask. The doping concentration reached 1×10^{17} cm^{-3}. Another 1 μm thermal oxide layer was grown and patterned exposing the Al contacts. Then, a layer of 1 μm Al was deposited and patterned to form the wires and soldering pads. The whole structure was released by backetch that removes backside silicon and buried oxide layer, and RIE on the front side to define the mirror plate and cantilever.

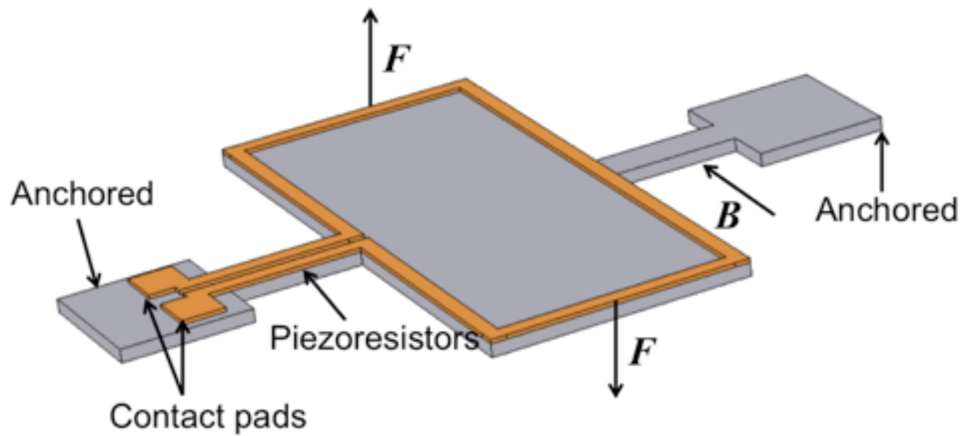

Figure 6.3: Schematic diagram of magnetic field sensor with piezoresistive sensing.

The motion of resonance cantilever is also measured with piezoresistive effects in the magnetic field sensor reported by Sunier et al. [22].

6.1.3 Optical sensing of sensor membrane position

As illustrated in Figure 6.4, with an AC current flowing across the resonator, an alternating Lorentz force is generated on the resonator, resulting in the mechanical vibration

of the resonator. With an optical positioning system, the amplitude of vibration can be measured accurately.

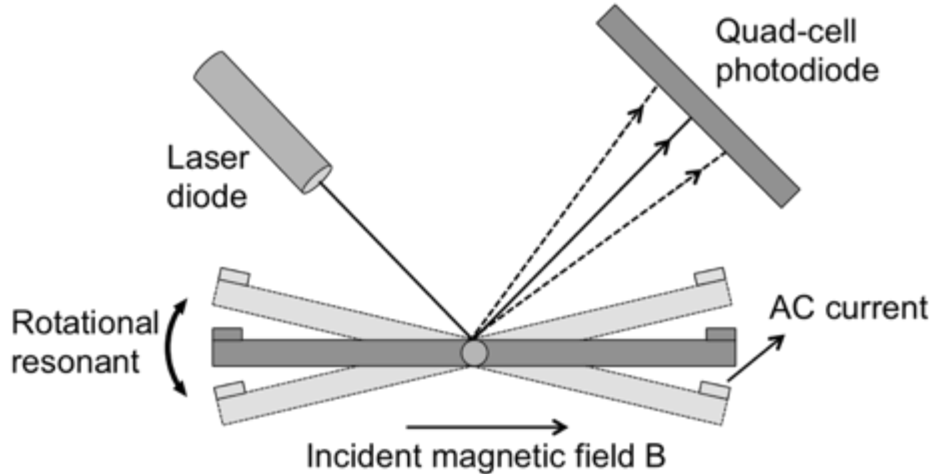

Figure 6.4: Resonance based magnetic field sensor with optical measurement.

A xylophone bar magnetometer was designed and fabricated by Oursler et al. [23]. The 5 mm × 0.5 mm × 0.25 mm xylophone bar was fabricated by chemically milling the nonmagnetic CuBe foil. The xylophone bar oscillated when an AC current flowed across, generating an alternating Lorentz force. The magnitude of the oscillation was measured optically, by a laser diode and position-sensitive photodiode (PSD).

A resonance based MEMS magnetic field sensor has been built in this thesis. A Lorentz force actuated MEMS micromirror resonates while an AC current flows across the Lorentz coil. The amplitude of the torsional resonance is measured with a quad-cell photodetector and external electronics. This magnetic field sensor shows a linear response between the resonant rotational angle and the magnetic field strength at atmospheric pressure. This magnetic field sensor presents a resolution of 0.4 nT, at 50mA$_{rms}$ bias current and 53 mHz bandwidth. At different level of bias current, resonance MEMS Lorentz magnetic field sensors can work in a wide range of measurement, from nT to T.

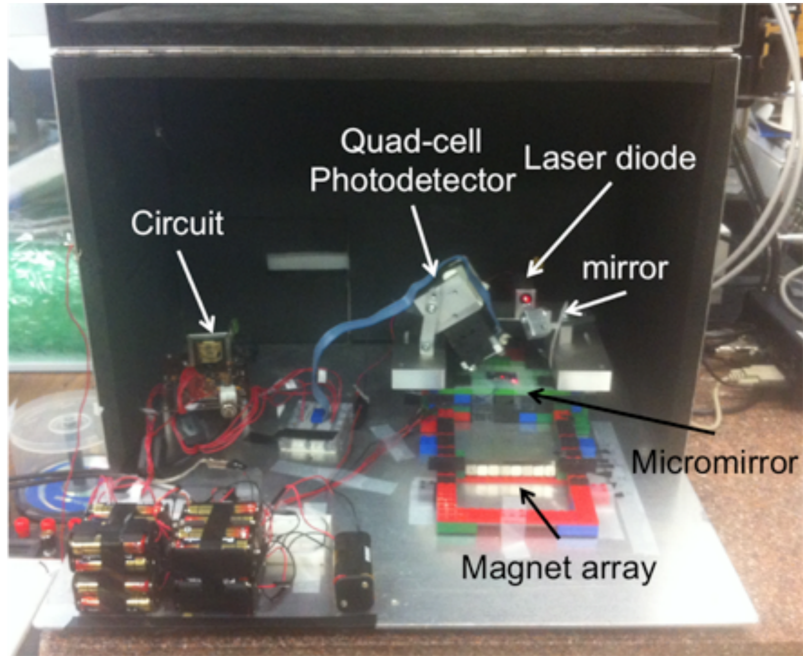

Figure 6.5: Resonance based magnetic field sensor set-up.

6.2 Working principle of developed sensor

Figure 6.6 illustrates the working principle of the magnetic field sensor developed in this thesis. The sensor operates by Lorentz force acting on the rotating micromirror. An AC current is applied to the coil on the mirror, generating periodic Lorentz force when in the presence of an incident magnetic field. It should be noted that a benefit of this Lorentz sensor, is that it's measurement sensitivity is a function of the AC coil current, and so it can be adjusted as required to measure a wide range of magnetic field, from nT to T values.

The AC current is set to the mechanical resonant frequency of the mirror, in order to greatly augment motion. Mirror #1 ($Membrane_{thickness}$ = 11 µm, $Spring_{segment\ \mathrm{length}}$ = 2 mm, resonance 364 Hz) was chosen, due to its smaller spring constant. This offers a bigger deflection angle with the same current and same magnetic field, and thus contributes to a higher sensitivity of the magnetic field sensor.

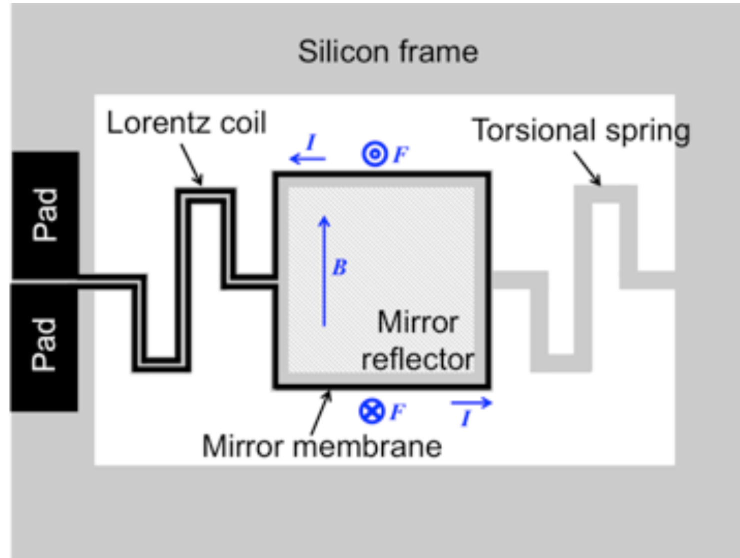

Figure 6.6: Schematic of micromirror and Lorentz force coupling.

As discussed in Section 5.2.2, the micromirror showed a non-linearity at larger angles of deflection. Figure 5.10 (reproduced as Figure 6.7 below) plots the deflection angle vs. driving current. When implementing the mirror as a magnetic field sensor, the mirror motion should be within its linear range to achieve a linear response to the incident magnetic field.

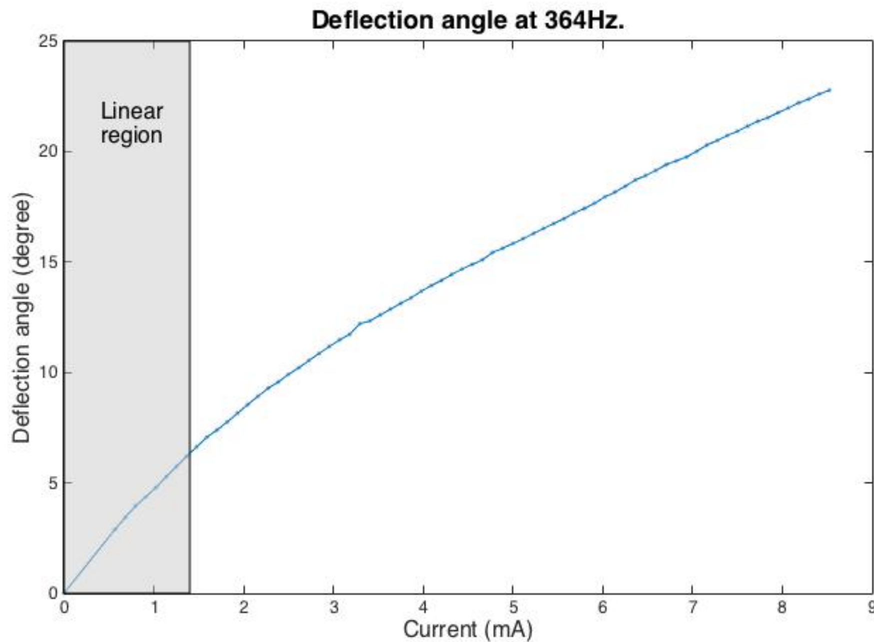

Figure 6.7: Deflection angle vs. driving current, mirror #1

An optical positioning system was used to provide high accuracy deflection angle measurement of the mirror. Figure 6.8 illustrates the block diagram of the magnetic field sensor system. Figure 6.9 shows the optical positioning system, which uses a quad-cell photodetector. The principles of the optical positioning system are discussed below.

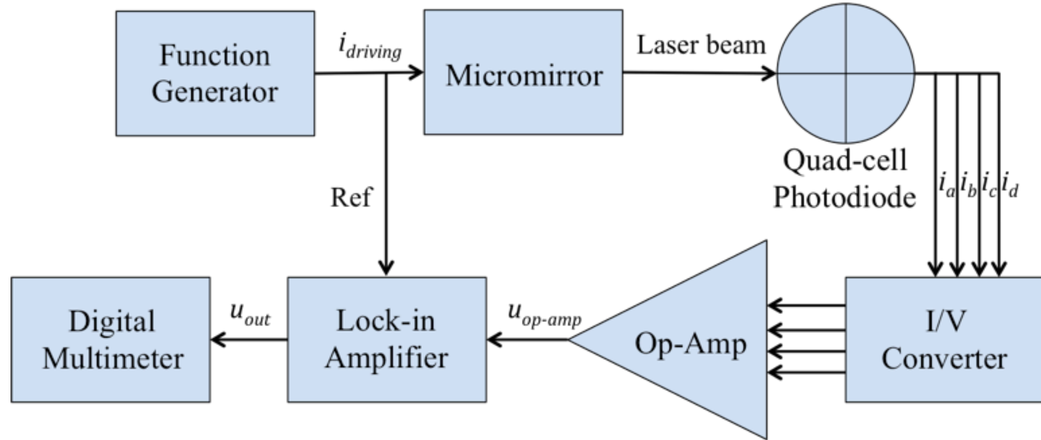

Figure 6.8: Block diagram of magnetic field sensor system.

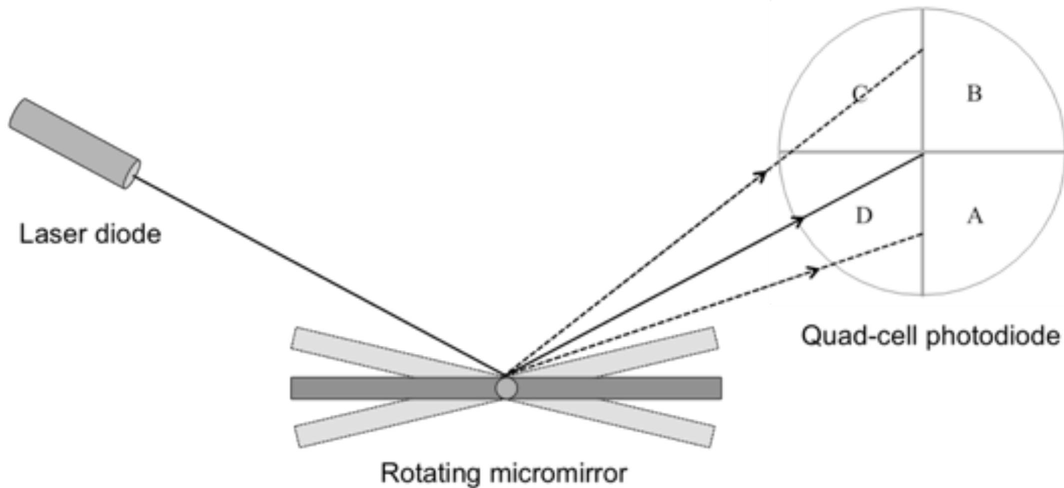

Figure 6.9: Angle measurement with the optical positioning system.

In the magnetic field sensor system, a function generator (Agilent 33120A) provides a small AC current $i_{driving}$ driving the micromirror at its resonance. The micromirror is resonating with a deflection angle θ, which is smaller than 1°, and so in the mirror's linear range. Thus, the deflection angle θ follows the following equation:

$$\theta = k_1 i_{driving} B \tag{6.4}$$

As illustrated in Figure 6.9, the small deflection angle is measured with the optical positing system, which contains a laser diode (PTI Technologies PM01(635-5B)G3) and a quad-cell photodiode (Advanced Photonics SD380-23-21-051). The laser beam was aligned to the center gap of the quad-cell photodetector before the actuation. On the quad-cell photodiode, the moving distance of the laser spot is proportional to the deflection angle of the micromirror. As the micromirror rotates, the laser spot on the quad-cell moves up and down across the narrow gap. The current output of each section is proportional to the receiving light intensity. The current output was converted to voltage signal, and fed to an operation amplifier, which calculates the relative position of the laser spot in y-axis with Equation 6.2:

$$u_{op-amp} = k_2 \frac{(i_B + i_C) + (i_A + i_D)}{i_A + i_B + i_C + i_D} \tag{6.5}$$

where i_A, i_B, i_C, i_D representing the current output of each section on the photodetector.

Then, the signal is passed to a lock-in amplifier (Stanford research system SR830 DSP), with the driving current as its reference. In the lock-in amplifier, the input signal $u_{opt-amp}$ is multiplied with the reference signal $i_{driving}$ (Equation 6.3), and then filtered with a low pass filter (Equation 6.4).

$$\begin{aligned} u &= k_3 u_{op-amp} i_{driving} \\ &= k_3 U_{op-amp} \sin(\omega t + \varphi) I_{driving} \sin(\omega t + \varphi) \\ &= \frac{1}{2} k_3 U_{op-amp} I_{driving} + \frac{1}{2} k_4 U_{op-amp} I_{driving} \cos(2\omega t + 2\varphi) \end{aligned} \tag{6.6}$$

$$u_{out} = \frac{1}{2} k_3 U_{op-amp} I_{drive} \tag{6.7}$$

The voltage output u_{out} of the lock-in amplifier is measured with a digital multimeter (Agilent Technologies 34461A). The voltage output measured at the digital multimeter is a DC signal, which makes it difficult to observe the background noise and signal-to-noise ratio.

In order to observe the real-time background noise, the driving current is turned on and off every 30 seconds.

6.3 Measurement set-up

The entire magnetic field sensor system was built on a vibration isolation table. In order to further reduce noise, the sensor was put in an electrically grounded closed box to reduce the background light picked up by the photodetector, and electrical noise.

Figure 6.5 (reproduced as Figure 6.10 below) illustrates the testing set-up. A thick piece of aluminum was machined to mount the laser, a reflection mirror, and the quad-cell photodiode. An assembly of LEGO blocks was built to firmly and accurately position all the parts in place. The sensor was firmly attached to the surface plate with adhesive.

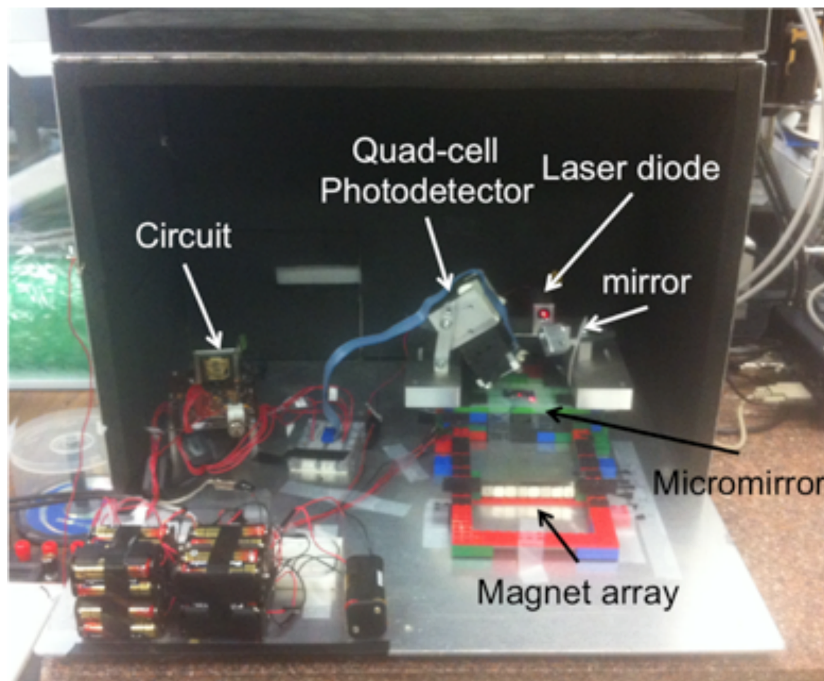

Figure 6.10: Resonance based magnetic field sensor set-up.

The magnetic field around the sensor is generated by permanent magnets. An array of ND-50 permanent magnets is placed at certain distance away from the sensor. The magnetic field at the micromirror was measured with a gaussmeter (AlphaLab GM1- ST). Figure 6.11 shows the strength of the magnetic field vs. distance from the magnets.

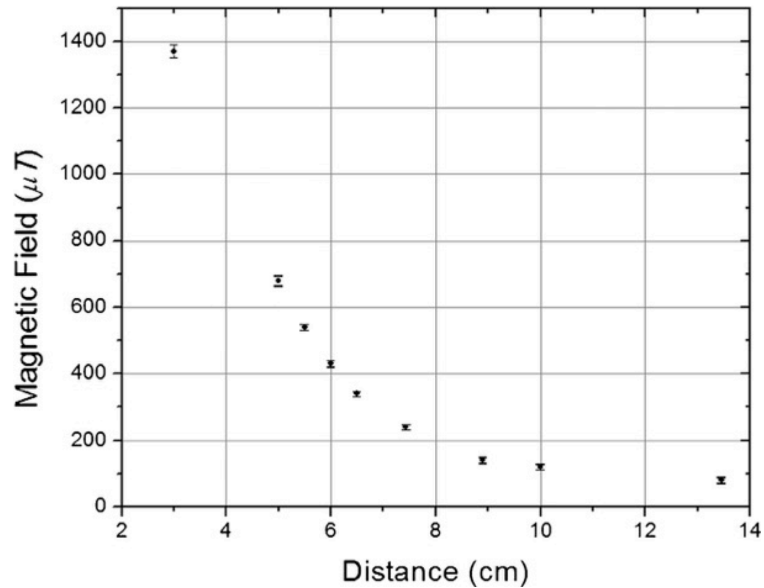

Figure 6.11: Measured magnetic field vs. distance from the sensor to magnets.

6.4 Resolution measurement

There are two main factors affecting the resolution of the magnetic field sensor: the noise level and deflection angle of the micromirror.

Noise level measurement

The first noise measurement study mainly analyzes the noise level at different current levels, and thus different Joule heating levels, without the incident magnetic field. The noise in the u_{out} was measured with a spectrum analyzer (Stanford Research System SR760).

Figure 6.12 is the noise spectrum of the signal before lock-in amplifier. From this measurement, we can calculate that the noise level is only increased by 0.4% when the driving current (rms) increases from 0.15 mA to 50 mA. It can also be observed that the working frequency 364 Hz is in the white noise region.

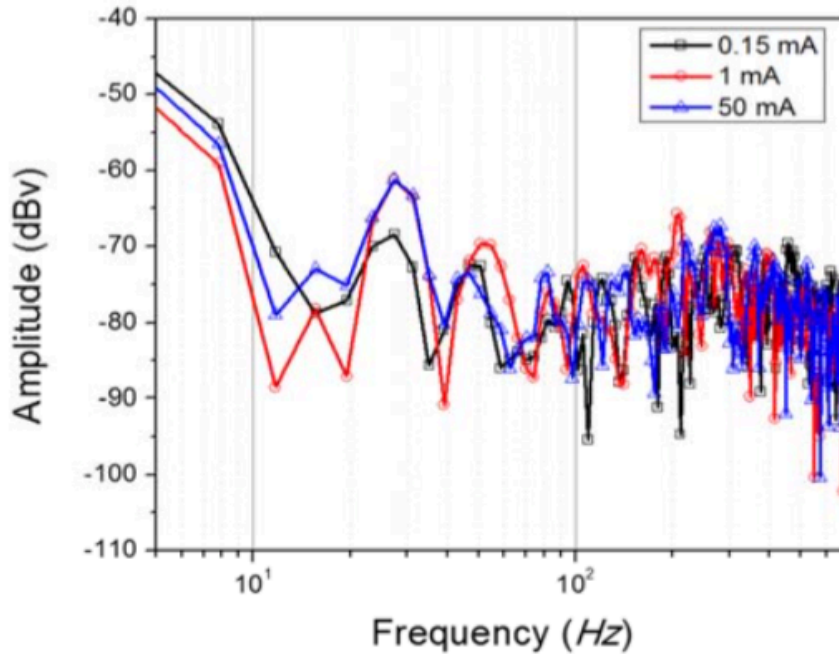

Figure 6.12: Noise spectrum of $u_{op\text{-}amp}$ with different driving current.

Noise was also measured with different integration times for the lock-in amplifier (Figure 6.13a), with incident magnetic field 80 μT, and driving current 0.15 mA. The lock-in amplifier works as a low-pass filter, whose bandwidth is inversely proportional to its integration time. Figure 6.13b plots the rms voltage of noise and SNR vs. integration time. It can be concluded from Figure 6.13 that a higher SNR is achieved at longer integration times. It was desired to use a 3 second integration time constant for measurements, for which the average noise level is 1.38 mV.

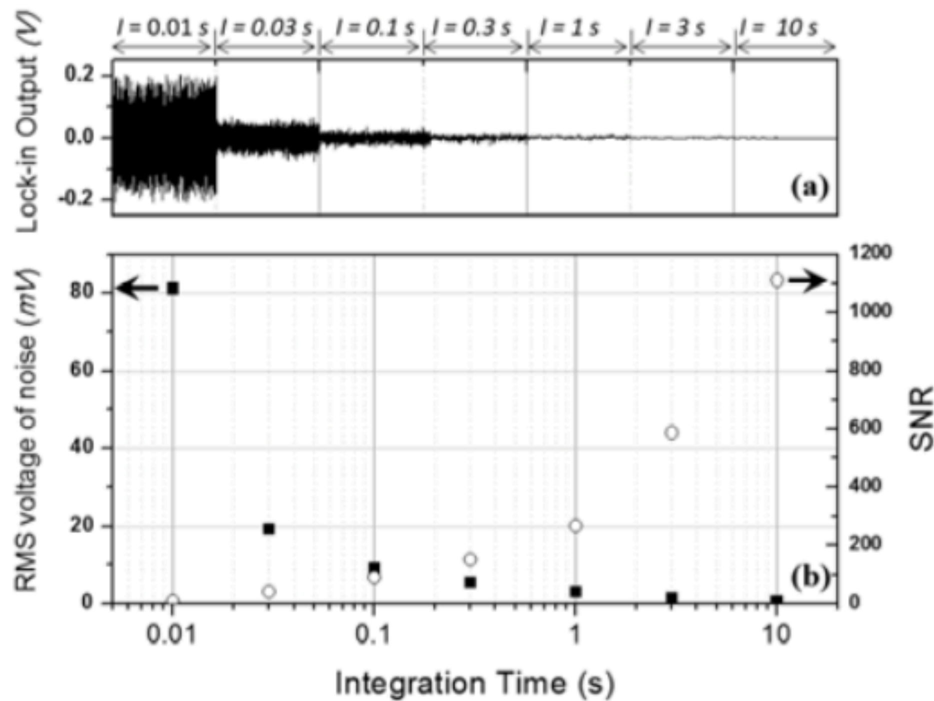

Figure 6.13: Noise signal (rms) at different integration times.

The deflection angle is determined by the driving current $i_{driving}$. When the driving current increases, the micromirror resonates at bigger angles, and thus a bigger signal is picked up by the photodetector.

As shown in Figure 6.12 and Figure 6.13, the noise level is not related to the driving current. It is only related to the integration time of lock-in amplifier.

Resolution calculation

To calculate the resolution, the magnetic field sensor was tested with different magnetic fields and with different driving currents. The integration time was chosen at 3 seconds (53 mHz bandwidth) for minimal noise. Figure 6.14 illustrates the output of the lock-in amplifier at the tested magnetic fields and driving currents.

For every driving current tested, a linear response is shown between lock-in amplifier output and magnetic field. This indicates that the magnetic field sensor can provide a wide range of magnetic field measurement with different driving current selection.

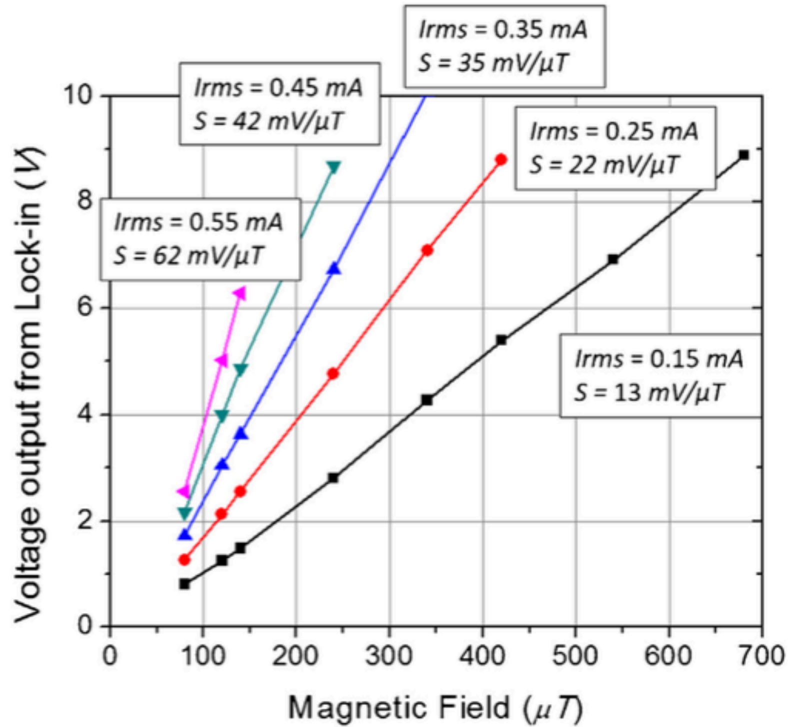

Figure 6.14: Measured sensitivities at different driving current, 3 seconds integration time.

The sensor sensitivity (*S*) shown in Figure 6.14 is found from the ratio of the lock-in amplifier voltage output and the incident magnetic field amplitude, using equation 6.5.

$$S = \frac{U_{out}}{B} \tag{6.8}$$

The minimum detectable magnetic field is the magnetic field with smallest voltage reading that can be differentiated from the noise:

$$B_{\min} = \frac{U_{noise}}{S} \tag{6.9}$$

where B is the magnetic field in the testing, U_{out} is the lock-in amplifier reading when B is applied, and U_{noise} is the rms voltage of noise at the lock-in amplifier output. With Equation 6.6, we can calculate that B_{min} is 136 nT with 0.15 mA driving current and 3 seconds integration time (U_{noise} = 1.38 mV).

Higher sensitivity can be achieved by increasing the driving current. When the driving current increases to 50 mA_{rms} (which is the current limit defined by electromigration current in aluminum of 10^5 A/cm^2), the minimal detectable magnetic field B_{min} is 0.4 nT. However, due to the limitation of the testing environment (interference of earth magnetic field, electrical cablings, and other sources), the sensor could not be tested at this low level.

6.5 Q-factor measurement

Figure 6.15 is the voltage output of lock-in amplifier vs. frequency sweep for the magnetic field sensor. The Q-factor of the magnetic field sensor is calculated with $Q=f_0/\Delta f$, where f_0 is the resonance frequency (364 Hz), and Δf is the half-power bandwidth (3.14 Hz). The Q-factor is calculated to be 116.

It should be noted that compared with the experiments in Section 5.2.2 for mirror#1, the Q-factor is much higher in this magnetic field sensor application. This is because a much lower driving current (0.15 mA) is used in this magnetic field sensor situation, which keeps the micromirror resonating in its linear region during the frequency sweep. By contrast in Section 5.2.2, the micromirror was tested with a 10 mA driving current (in non-linear range). Therefore, in the result of section 5.2.2 air damping limited the resonating amplitude, and thus decreased the Q-factor.

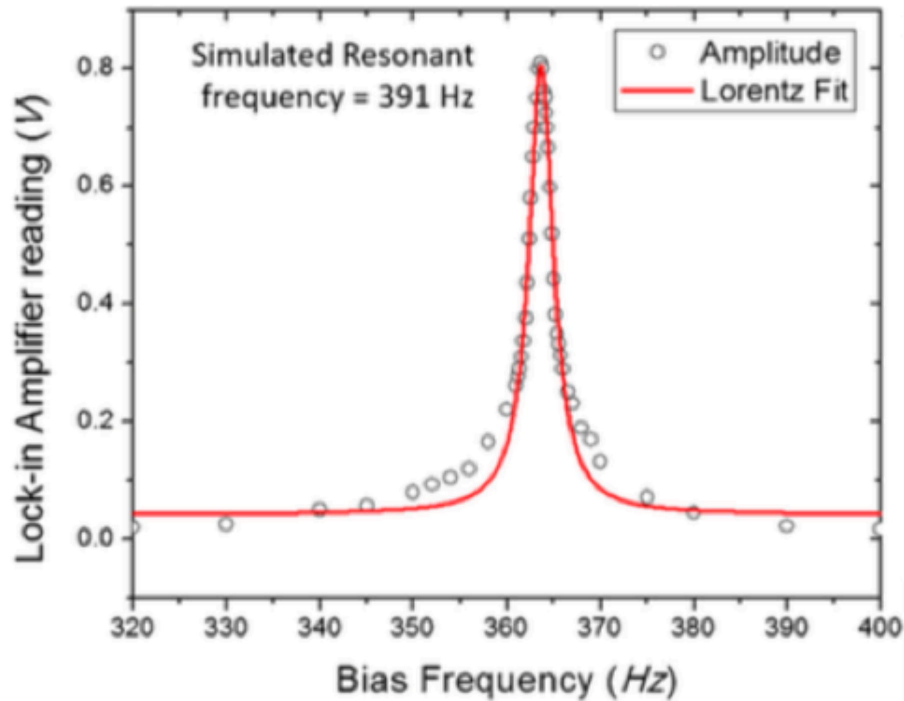

Figure 6.15: Q-factor of magnetic field sensor.

6.6 Conclusion

A magnetic field sensor was built based on the Lorentz force actuated micromirror. Sensing mechanisms and circuit design were discussed in this chapter. The sensitivity of the magnetic field was also measured and calculated. The magnetic sensor could achieve a sensitivity of 0.4 nT with 50 mA driving current and 3 seconds integration time.

Table 6.1 compares the results of this work with other resonance based magnetic field sensors. For this work, results of 0.1 second and 3 seconds integration time are presented. As can be seen, this sensor demonstrated the highest noise limited resolution compared to the other MEMS Lorentz force based magnetic field sensors.

Table 6.1: Summary of various resonance magnetic field sensors.

Publication	Sensing technique	Bandwidth (Hz)	Noise floor (nT/√Hz) at indicated bias current	Resolution (nT) at indicated bias current	Resolution frequency (kHz)	Quality factor	Dimension (mm)
This work at 3s int. time	Optical	0.053 at P_{atm}	1.78 at 50 mA_{rms}	0.4 at 50 mA_{rms}	0.364	116 at P_{atm}	3 × 3
This work at 0.1s int. time	Optical	1.6 at P_{atm}	11.6 at 50 mA_{rms}	2.7 at 50 mA_{rms}	0.364	116 at P_{atm}	3 × 3
Herrera-May et al. [21]	Piezoresistive	162.1 at P_{atm}	143 at 22 mA	143	136.52	842 at P_{atm}	0.4 × 0.15
Sunier et al. [22]	Piezoresistive	N/A	N/A	1000	175	600 at P_{atm}	0.4 × 0.185
Kádár et al. [19]	Capacitive	20-25	N/A	1	2.5	700 at 5 Pa	2.8 × 1.4
Kyynäräinen et al. [18]	Capacitive	2	10 at 0.1 mA	60	N/A	30,000 at 0.6 Pa	0.5 × 0.5
Li et al. [20]	Capacitive	1.9 at P_{atm}	17 at 5.8 mA_{rms}	17	49.1	12,700 at P_{atm}	2 × 2

Chapter 7: Conclusions and Future work

7.1 Conclusions

In this research successful fabrication processes for Lorentz force micromirrors and blazed gratings were developed.

Sharp blazed gratings were fabricated using anisotropic etching and oxidation sharpening. A reliable lithography process for 2 µm resolution was developed. The gratings have different periodicities: 3.06 µm, 7.35 µm and 9.80 µm. It was shown in the ellipsometer testing results that the grating periodicity matches well with the design.

The Lorentz force actuated micromirrors consist of 3 mm × 3 mm reflective mirror held by two silicon micro-springs. Both rotating and pop-up micromirrors were successfully fabricated. As expected, the deflection angle of the rotating micromirror showed linear response to driving current. However, the pop-up micromirror springs showed non-linearity at larger deflection angles. Compared with the COMSOL simulation results, the spring constant of all fabricated micromirrors agree with the simulated designs.

A magnetic field sensor was built based on a rotating micromirror. An AC current was flowed around the micromirror, to cause it to resonant in a magnetic field. The rotational amplitude of the resonanting mirror was measured with an optical positioning system and external circuits. The resonance amplitude of the magnetic field sensor was found to be linear vs. the incident magnetic field. The sensitivity of the magnetic field sensor was also found to be linear with respect to the driving current. The highest resolution of the magnetic field sensor is 0.4 nT at $50mA_{rms}$, and 53 mHz filter bandwidth. With appropriate selection of current level, this sensor can measure a wide range of magnetic field, from nT to T.

7.2 Future work

Future work on this project can focus on improving the quality of the micromirror. Further investigations could be done to study the thin film stress to achieve desired mirror curvature. A process may also be developed to etch blazed grating on the surface of the micromirror. Multiple turns of coil may be adopted to maximize the Lorentz force on the micromirror.

For the magnetic field sensor application, a smaller mirror could be fabricated to achieve higher resonance frequency and Q-factor. The resonante micromirror could also be placed in a vacuum for better performance.

References:

[1] Park, Byoungyoul, et al. "Lorentz force based resonant MEMS magnetic-field sensor with optical readout." *Sensors and Actuators A: Physical* (2016).

[2] Hornbeck, Larry J. "Digital Light Processing™: A new MEMs-based display technology." (1996).

[3] Krishnamoorthy, Uma, Daesung Lee, and Olav Solgaard. "Self-aligned vertical electrostatic combdrives for micromirror actuation." *Microelectromechanical Systems, Journal of* 12.4 (2003): 458-464.

[4] Schenk, Harald, et al. "Large deflection micromechanical scanning mirrors for linear scans and pattern generation." *Selected Topics in Quantum Electronics, IEEE Journal of* 6.5 (2000): 715-722.

[5] Nakai, Akihito, et al. "Double-sided scanning micromirror array for autostereoscopic display." *Sensors and Actuators A: Physical* 135.1 (2007): 80-85.

[6] Cho, Il-Joo, et al. "A low-voltage two-axis electromagnetically actuated micromirror with bulk silicon mirror plates and torsion bars." *Micro Electro Mechanical Systems, m2002. The Fifteenth IEEE International Conference on*. IEEE, 2002.

[7] Alpert, Nelson L., William E. Keiser, and Herman A. Szymanski. *IR: theory and practice of infrared spectroscopy*. Springer Science & Business Media, 2012.

[8] Ingle Jr, James D., and Stanley R. Crouch. "Spectrochemical analysis." (1988).

[9] Daly, James T., et al. "Monolithic infrared spectrometer apparatus and methods." U.S. Patent No. 6,303,934. 16 Oct. 2001.

[10] Peters, Jason E., et al. "Infrared absorption of Czochralski germanium and silicon." *International Symposium on Optical Science and Technology*. International Society for Optics and Photonics, 2001.

[11] Palmer, Christopher A., and Erwin G. Loewen. *Diffraction grating handbook*. Springfield, Ohio, USA: Newport Corporation, 2005.

[12] Hintschich, S. I., et al. "MEMS-based miniature near-infrared spectrometer for application in environmental and food monitoring." (2014).

[13] Campbell, Stephen A. *The science and engineering of microelectronic fabrication.* Oxford University Press, 2001.

[14] Maus, Stefan, et al. "The US/UK world magnetic model for 2010-2015." (2010).

[15] Tumanski, Slawomir. "Modern magnetic field sensors–a review." *Organ* 10 (2013): 13.

[16] Oliver, Steven A., et al. "Magnetic field measurements using magneto-optic Kerr effect sensors." *Optical Engineering* 33.11 (1994): 3718-3722.

[17] Josephs-Franks, P., et al. "Measurement of the spatial sensitivity of miniature SQUIDs using magnetic-tipped STM." *Superconductor Science and Technology* 16.12 (2003): 1570.

[18] Kyynäräinen, Jukka, et al. "A 3D micromechanical compass." *Sensors and Actuators A: Physical* 142.2 (2008): 561-568.

[19] Kádár, Zs, et al. "Magnetic-field measurements using an integrated resonant magnetic-field sensor." *Sensors and Actuators A: Physical* 70.3 (1998): 225-232.

[20] M. Li, et al. "Single-structure 3-axis Lorentz force magnetometer with sub-30 nT/√ HZ resolution." *2014 IEEE 27th International Conference on Micro Electro Mechanical Systems (MEMS)*. IEEE, 2014.

[21] Herrera-May, A. L., et al. "A resonant magnetic field microsensor with high quality factor at atmospheric pressure." *Journal of Micromechanics and Microengineering* 19.1 (2008): 015016.

[22] Sunier, Robert, et al. "Resonant magnetic field sensor with frequency output." *Journal of microelectromechanical systems* 15.5 (2006): 1098-1107.

[23] Oursler, Douglas A., et al. *Development of the Johns Hopkins xylophone bar magnetometer*. Johns hopkins univ laurel md applied physics lab, 1999.